Air Bearing Slider Dynamics and Stability in Hard Disk Drives

by

Vineet Gupta

B. Tech (Indian Institute of Technology, Madras) 2002
M.S. (University of California, Berkeley) 2006

A dissertation submitted in partial satisfaction of the

Requirements for the degree of

Doctor of Philosophy

in

Engineering – Mechanical Engineering

in the

Graduate Division

of the

University of California, Berkeley

Committee in charge:

Professor David B. Bogy, Chair
Professor Oliver O'Reilly
Professor Andrew R. Neureuther

Fall 2007

The dissertation of Vineet Gupta is approved:

Chair _____ Date _____

_____ Date _____

_____ Date _____

University of California, Berkeley

Fall 2007

Air Bearing Slider Dynamics and Stability in Hard Disk Drives

by

Vineet Gupta

ABSTRACT

Air Bearing Slider Dynamics and Stability in Hard Disk Drives

By

Vineet Gupta

Doctor of Philosophy in Engineering – Mechanical Engineering

University of California, Berkeley

Professor David B. Bogy, Chair

The disk drive industry is continuously trying to achieve higher data storage densities, faster data transfer rates, and higher reliability at lower cost. The new storage density goal of 3 Tbit/in^2 dictates smaller magnetic spacing and a reduction in the slider's vibrations. With tighter limits on slider vibrations and elevated excitation due to intermolecular forces, electrostatic forces, windage and shock, small variations of slider pose a potential threat of head-disk interface (HDI) failures. Thus, this dissertation aims to study the slider dynamics and stability in hard disk drives and to propose strategies not only for reducing the slider vibrations, but also for enhancing the stability of the HDI.

The research presented here addresses three objectives. Firstly, there is a need to reliably predict the system behavior at high disk rotation speeds and at low mechanical spacing. Researchers in the past have used a simple model consisting of a slider and an air bearing model, while completely ignoring the dynamics of the head-stack assembly (HSA) and the disk. It has been shown that the system dynamics predicted by these models is significantly different from the actual system response (measured experimentally) during slider-disk contact/impact, aerodynamic forcing, shocks, track seek, load-unload etc. In this dissertation a new simulation program is proposed which seeks to predict the system dynamics by including the HSA and the disk model for the first time.

The second objective is to investigate the slider dynamics and stability caused by intermolecular and electrostatic forces acting on the slider and the aerodynamic forces acting on the HSA and the disk. The effect of intermolecular and electrostatic forces on the slider's 6 degrees-of-freedom (DOF) and the interaction of the length scale of the slider-disk topographies with the slider vibrations and stability are investigated for the first time in this dissertation. The first ever numerical investigation of slider vibrations due to aerodynamic forcing of the HSA and the disk considering the effect of the HDI forces is also reported here. Further, the effects of several flow mitigation devices, smaller suspensions and reverse spinning disks on flow-induced slider vibrations are investigated.

But even if all targets for reduced mechanical spacing and tighter limits on slider vibrations are met, the superparamagnetic limit restricts the maximum achievable recording density on the conventional media to about 0.5-1 Tbit/in^2. Patterned media has been proposed as an alternative to overcome this limit and achieve recording densities greater than 3Tbit/in^2. But one of the main obstacles to patterned media is achieving stable mechanical slider-disk spacing. Thus the third objective of this dissertation is to study the slider's flying characteristics on a patterned media. The dynamics of the slider along all 6 DOF and its stability is investigated for the first time in this dissertation. Optimal patterned disk topography is also proposed for maximum stability of the slider over patterned disk surface.

Professor David B. Bogy

Dissertation Committee Chair

DEDICATION

To my parents and sister

TABLE OF CONTENTS

LIST OF FIGURES

LIST OF TABLES

ABBREVIATIONS

AR	Area Ratio
BPI	Bits per Inch
BPM	Bit Patterned Media
DTM	Discrete Track Media
FH	Flying Height
FHM	Flying Height Modulation
HDD	Hard Disk Drive
HDI	Head Disk Interface
HGA	Head Gimbal Assembly
HMS	Head Media Spacing
HSA	Head Stack Assembly
ID	Inner Diameter
IMF	Intermolecular Forces
IRS	Improved Reduced System
MD	Middle Diameter
MFH	Minimum Flying Height
OD	Outer Diameter
PH	Pattern Height
RMS	Revolutions per Minute
SD	Standard Deviation
TMR	Track Misregistration
TPI	Tracks per Inch

ACKNOWLEDGEMENTS

I am honored to have the privilege of working under the supervision of Professor David B Bogy during my graduate studies at Berkeley. I would like to thank him for the excellent technical advice to guide my research, while at the same time giving me the freedom to explore my academic interests. I am really fortunate to have him both as an advisor and a mentor.

I owe a great deal to Dr. C. Singh Bhatia for his guidance and for many illuminating discussions that we had throughout my graduate studies. His confidence in me has motivated me to make this dissertation a better piece of work. I would also like to thank Professor Oliver O. Reilly and Professor Andrew R. Neureuther for their valuable feedback while reviewing this dissertation.

One of the benefits of living at Berkeley is the opportunity to interact with truly outstanding individuals: Rohit Ambekar, Rohit Karnik, Sandipan Mishra and Sujit Kirpekar. I am thankful not only for the helpful discussions, but also for their support and friendship.

Finally, I would like to acknowledge the role of my parents and my sister in my success as graduate student. Their constant love, sacrifice, support and encouragement are the solid foundation for my well being and achievement.

The research presented in this dissertation was supported by the Computer Mechanics Laboratory at the University of California, Berkeley, and the Information Storage Industry Consortium's extremely high density recording program.

Vineet Gupta

Berkeley May 2007

CHAPTER 1

INTRODUCTION

1.1 The History of Hard Disk Drives

The year 2006 marked the 50th anniversary of the hard disk drive (HDD). The first hard disk drive IBM 350 (Figure 1.1), invented by Reynold B. Johnson, was shipped in September, 1956 with the IBM 305 computer [1]. This hard drive had fifty disks, each 24 inches in diameter rotating at 1200 RPM. The drive measured 60"X68"X29" and weighed more than a ton. There were 100 bits per inch on a track and 20 tracks per inch amounting to an areal recording density[1] of 2Kbit/in^2. The head-to-media spacing was 20 μm and the data transfer rate was 8,800 characters per second [2].

A lot has changed since. Recently Seagate Technologies introduced the Savvio 15K (Figure 1.2) [3]. It's a 2.5 inch form factor drive with two disks rotating at 15,000 RPM and an average head-to-media spacing of less than 10 nm across the disk. This drive measures 3.95"X2.76"X0.58", weighs 210 gm and has a data transfer rate of 400 Mbytes per second. There are 890,000 bits per inch on a track and 125,000 tracks per inch amounting to an areal recording density of 110 Gbit/in^2. That's a 50 million fold increase in storage density with quite a reduction in the size and the weight over the past 50 years.

[1] The areal recording density (usually expressed in bits per square inch, bits/in^2) is defined as the amount of data that can be stored on a unit area of the recording medium. In hard disk drives, areal density is equal to the product of the linear bit density (the number of bits per inch – BPI – along a circumferential track) and the track density (the number of tracks per inch – TPI).

This astonishing growth rate in the storage density has been made possible by scaling down the recorded bit size and thus increasing the linear bit density and the track density. Figure 1.3 shows the increase in the linear bit density, the track density and the areal recording density of hard disk drives since 1990 to date [4]. Moreover the cost per MByte has also reduced drastically over the years (Figure 1.4) making hard disk drives the primary online data storage device for all commercial as well as personnel applications.

1.2 Hard Disk Drives Basics

As shown in Figure 1.5 a typical hard disk drive consists of a single disk or several disks mounted on a spindle that rotates somewhere between 4,200 and 15,000 RPM. There are two read/write heads for each disk, one for each surface of the disk. The read/write head contains separate read and write elements that reads and writes data on the disk. This read/write head is mounted on a slider which is attached to a suspension. The head-slider-suspension assembly is known as the head gimbal assembly (HGA). The HGA is mounted on an "E-block" arm attached to the actuator. The actuator is rotated by a voice coil motor which enables the head to move across all the tracks on the disk surface. The HGA-E block-voice coil motor assembly is known as the head-stack assembly (HSA).

The disk is made of an aluminum base metal or glass substrate coated with a thin layer of magnetic material. For extremely high density recording a magnetic material with high magnetization constant and extremely small grain size is used. The data is stored as the magnetic polarization of the bits, where each bit is made up of several grains. Smaller grain size implies smaller bit size, allowing more bits per unit area of the disk surface. The disk is also covered with a layer of a protective overcoat, usually a carbon based material and a thin

lubricant layer, to increase the durability.

The strength of the read-back signal depends on the magnetic spacing between the slider and the disk, also known as the head-media spacing (HMS). The HMS includes the mechanical spacing, the slider and the disk overcoats and the protective lubricant layer on the disk as shown in Figure 1.6 [3]. The mechanical spacing between the slider and the disk is also known as the flying height. Figure 1.7 shows the decrease in the mechanical spacing between the slider and the disk over the years [4]. For current products the HMS is approx. 10 nm and the flying height is approx. 5 nm. But in order to achieve recording densities up to and beyond 3 Tbit/in^2, the HMS must be reduced to less than 5 nm and the flying height and the overcoat thicknesses must also be reduced as shown in Figure 1.8 [5].

1.3 Motivation

The disk drive industry is continuously trying to achieve higher data storage densities, faster data transfer rates, and higher reliability at lower cost. The new areal storage density goal of 3 Tbit/in^2 can only be achieved by increasing the track density and the linear bit density. The Wallace spacing loss equation, which governs the strength of the read-back signal, dictates that the linear bit density can be increased by reducing the head media spacing. This in turn requires squeezing the track misregistration (TMR) and flying height modulation (FHM) into tighter limits. But as the flying height between the slider and the disk reduces to less than 5 nm, the slider and disk will be either in intermittent or continuous contact and additional forces, such as intermolecular forces, electrostatic forces, contact force and friction force will also act on the slider and thereby excite the structural modes of the HSA and the disks, increasing the TMR and the FHM.

In order to investigate the effect of intermolecular and electrostatic forces a single degree of freedom (DOF) head-disk interface (HDI) model is first considered. This model is used to characterize the nonlinear dynamics of the slider under the influence of the electrostatic and intermolecular forces. The differential equation that describes the fly height *z(t)* of the air bearing slider is given by:

$$m\frac{d^2z}{dt^2} + c\frac{dz}{dt} + k_a(z-h) = -\nabla V_{imf}(z) - \nabla V_{elec}(z) \tag{1.1}$$

Here m, c and $k_a=\beta z^{-\alpha}$ are the effective mass (1.6 mg), the air bearing damping (0.02 Ns/m) and the nonlinear air bearing stiffness (β = 4x10^6 N/m, and α = 0.6368) respectively. The stiffness of the vertical mode is highly nonlinear for low flying sliders, so the nonlinear nature of the air bearing stiffness is considered in this analysis. The variable z describes the motion of the slider and the variable h is the steady fly height of the slider in the absence of intermolecular and electrostatic forces. $V_{imf}[z(t)]$ is the potential due to intermolecular interaction between the slider and the disk, assumed to be derived from a plane-plane interaction represented as [6]:

$$V_{imf}[z(t)] = -\frac{A\,dxdy}{12\pi z^2} + \frac{B\,dxdy}{360\pi z^8} \tag{1.2}$$

Here A (8.9238x10^{-20} J) is the effective Hamaker constant between the slider and the disk, B (10^{-76} Jm^6) is another constant and *dxdy* (250x10^{-12} m^2) is the area of the slider in close proximity with the disk. $V_{elec}[z(t)]$ is the potential due to electrostatic interaction between the slider and the disk, which can be represented as [6]:

$$V_{elec}[z(t)] = -\frac{\varepsilon_o k_e V^2 dxdy}{2z} \tag{1.3}$$

Here ε_o, k_e and V are the permittivity constant (8.85 x 10^{-12} farad/m), dielectric constant of the medium (1 for air) and the potential difference between the slider and the disk.

The stability of the HDI under the influence of the electrostatic and intermolecular forces can be analyzed by considering the energy of the system. As the air bearing sliders usually have very small damping, we consider for simplicity an un-damped system. Thus the energy of the system is conserved and the potential energy method can be used to evaluate the equilibria and analyze their stability.

The potential energy of the system which remains conserved during the motion can be expressed as:

$$U = \beta z^{-\alpha}\left(-\frac{hz}{1-\alpha}+\frac{z^2}{2-\alpha}\right)-\frac{\varepsilon_o k_e V^2 dxdy}{2z}-\frac{A\,dxdy}{12\pi z^2}+\frac{B\,dxdy}{360\pi z^8}+const \tag{1.4}$$

A close connection is obtained between the features of the interaction potential well and the nonlinear slider response. The criterion for an equilibrium point, z^*, is satisfied when the systems potential energy reaches a stationary point in a potential energy verses z plot. Thus the equilibrium equation reduces to:

$$\frac{\partial U_{tot}}{\partial z} = 0 \tag{1.5}$$

The equilibrium point is stable if the potential energy evaluated at the equilibrium is a local minimum, i.e.,

$$\left.\frac{\partial^2 U_{tot}}{\partial z^2}\right|_{z^*} > 0 \tag{1.6}$$

and it is unstable if the potential energy at the equilibrium point is a maximum, i.e.,

$$\left.\frac{\partial^2 U_{tot}}{\partial z^2}\right|_{z^*} < 0 \tag{1.7}$$

With different initial conditions, we get slider motions corresponding to different level sets of the energy of the system. The bifurcation diagram using the simple 1-DOF model is plotted in Figure 1.9 for the case of v = 0.5 volts. The ordinate is the equilibrium fly height between the slider and the disk in the presence of intermolecular and electrostatic forces while the abscissa is the steady state fly height between the slider and the disk in the absence of intermolecular and electrostatic forces. The potential difference between the slider and the disk is assumed to be 0.5 volts. We observe that at very low values of the numerical parameter h (say 0.6 nm) there exists one equilibrium point. For values of h between 1.36 nm and 4.81 nm, the system has three equilibrium points. And as the value of h increases beyond 4.81 nm the system has just one equilibrium point.

To analyze the stability of the various equilibrium points under the influence of the intermolecular and the electrostatic forces, we plot phase portraits and potential wells for the system. The phase portraits and potential wells as a function of the slider's motion for h = 0.6, 2.0 and 5.0 nm for v = 0.5 volts are plotted in Figure 1.10.

The plot of the potential well for h = 0.6 nm in Figure 1.10 (a) shows only one stationary point and it is a local minimum. Hence this is a stable equilibrium. This can be observed in

the phase portrait as well (Figure 1.10 (b)). When h is increased to 2.0 nm the potential energy curve in Figure 1.10 (c) shows three stationary points and hence three equilibria. The lower and higher ones are local minima corresponding to stable equilibria. The equilibrium point between the two stable equilibria is a local maximum and hence it corresponds to an unstable equilibrium point. This can also be observed in the phase portrait (Figure 1.10 (d)). When h is further increased to 5.0 nm the plot of potential energy shown in Figure 1.10 (e) has only one stationary point and it is a local minimum. Hence this is a stable equilibrium point. This can be observed in the phase portrait as well (Figure 1.10 (f)).

The bifurcation diagram in Figure 1.9 divides the motion of the slider into a monostable regime (far from the surface) and a bistable regime (close to the surface) where two stable and one unstable equilibria coexists. Here the equilibrium closer to the surface has a head media separation less than 0.3 nm. Thus it corresponds to a state where the slider is effectively stuck to the disk surface. This simple 1-DOF analysis indicates that the multiple equilibria heights exists when the slider is flying very close to the disk surface and even a small perturbation – due to disk roughness/waviness, aerodynamic excitation or shock – can cause the slider to oscillate about the unstable equilibrium, resulting in large slider vibrations and an unstable HDI. Thus there is a need to study the slider dynamics and stability due to intermolecular and electrostatic forces at a higher level of complexity and propose strategies for reducing slider vibrations and enhancing stability of the HDI.

Similarly, the demand for higher data transfer rates requires a reduction in the seek time and a reduction in the latency. Seek time, which is the time required to move the read/write head from one track to another, can be reduced by using faster positioning speeds of the HSA.

And, latency, which is the time for the target sector on the disk to rotate under the read/write head, can be reduced by using faster disk rotation speeds. But faster positioning speeds results in higher residual vibration of the HSA and faster disk rotation speeds results in greater flow velocities and higher levels of aerodynamic forcing on the HSA. This results in further excitation of the structural modes of the HSA and the disks, increasing the TMR and FHM.

Figure 1.11 shows the plot of the slider's vibration in the out-of-plane, on-track and off-track directions due to the aerodynamic forcing of the HSA. We observe that the FHM and the TMR due to aerodynamic forcing alone are 0.12 nm and 7.54 nm, respectively. Moreover additional excitation due to bearing hysterisis, HDI forces, spindle and disk run-out, shock and vibrations will further increase the TMR. But for an areal density of 3 Tbit/in^2 the track density should be greater 500,000 TPI which translates to a track width of 50 nm and a TMR of less than 5 nm. Thus there is a need to study the slider dynamics at a higher level of complexity and propose strategies for reducing flow-induced slider vibrations.

Similarly, with an increasing usage of HDD in digital audio/video players, digital camcorders, digital organizers and cellular telephones, the HDD is subjected to harsher conditions. The HDD is subjected to continuous vibrations when it is operated in a car driving on an unpaved road, or is subjected to shock when accidentally dropped on a floor. Such events further increase the TMR and the FHM. This may even affect the reliability of the system and can compromise its usage in a variety of applications.

With drastic reduction in the permissible TMR and the FHM in order to achieve higher areal

densities, and the elevated excitation due to windage, shock, contact, friction, electrostatic and intermolecular forces as a result of wide range of applications of HDD, faster disk rotation speeds and reduced mechanical spacing between the slider and the disk – smaller variations in slider positioning pose a potential threat of head-disk interface (HDI) failures. Consequently, effects that were formerly considered negligible are now becoming quite significant. This motivates studying the dynamics and the stability of the air bearing sliders at a higher level of complexity and proposing strategies for enhancing the HDI stability and reducing the TMR and the FHM.

1.4 Objectives

Succinctly, this dissertation aims to study the air bearing slider dynamics and stability in hard disk drives and to propose strategies not only for reducing the TMR and the FHM of the slider, but also for enhancing the stability of the HDI.

This dissertation is organizes as follows. In chapter 2 the new numerical simulator developed to model slider dynamics in a HDD is presented. This simulator consists of a disk and HSA model along with the usual 6-DOF slider and air bearing models. Various model order reduction techniques used to model the disk and HSA are presented. Several metrics developed to measure the accuracy of the reduced model are also discussed.

In chapter 3 the effect of intermolecular and electrostatic forces are discussed on slider dynamics and stability over a perfectly smooth HDI. In chapter 4 the effect of slider-disk surface topography on slider dynamics is analyzed in the presence of intermolecular and electrostatic forces.

In chapter 5 the effect of air flow on slider vibrations is discussed. In this chapter we also derive scaling laws to predict the slider in-plane and out-of-plane vibrations as a function of slider radial position and disk RPM. In chapter 6 the effect of flow mitigation devices on in-plane slider vibrations is investigated. In this chapter we also examine several other strategies, such as spinning the disk in reverse direction and reducing the suspension length, for mitigating the flow-induced slider vibrations in the HDD.

In chapter 7 the slider's flying characteristics over a patterned media is analyzed. In this chapter we also discuss the stability of the slider over a patterned media disk. And finally in chapter 8 a brief summary of this dissertation is presented.

1.5 Figures

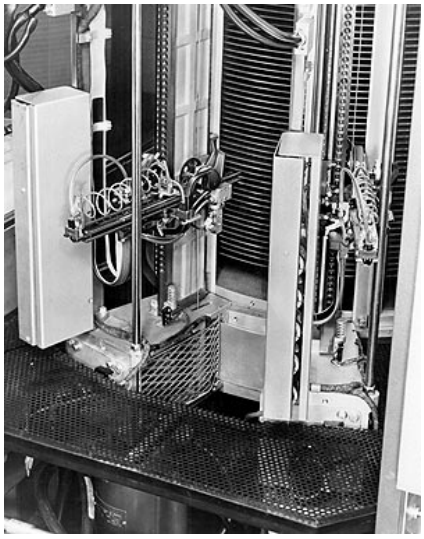

Figure 1.1: The first hard disk drive – IBM 350 (From [2])

Figure 1.2: The Seagate Savvio 15K (From [3])

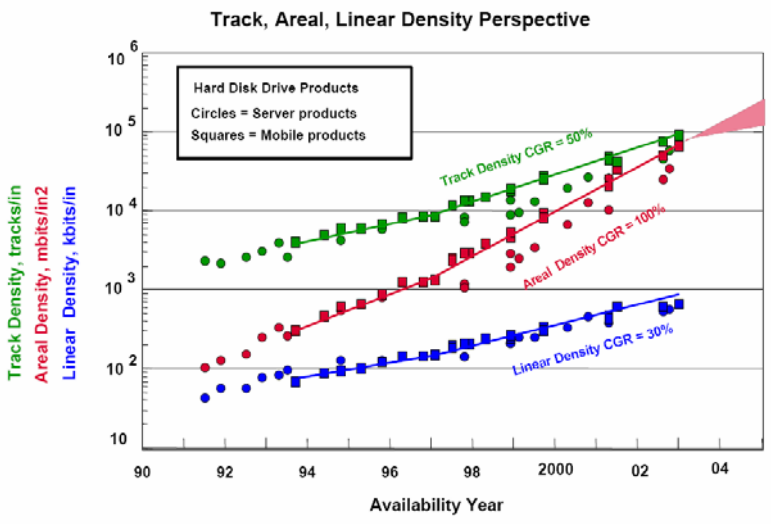

Figure 1.3: The growth in the linear bit density, track density and the areal recording density of the hard disk drive from 1990 to date (From [4])

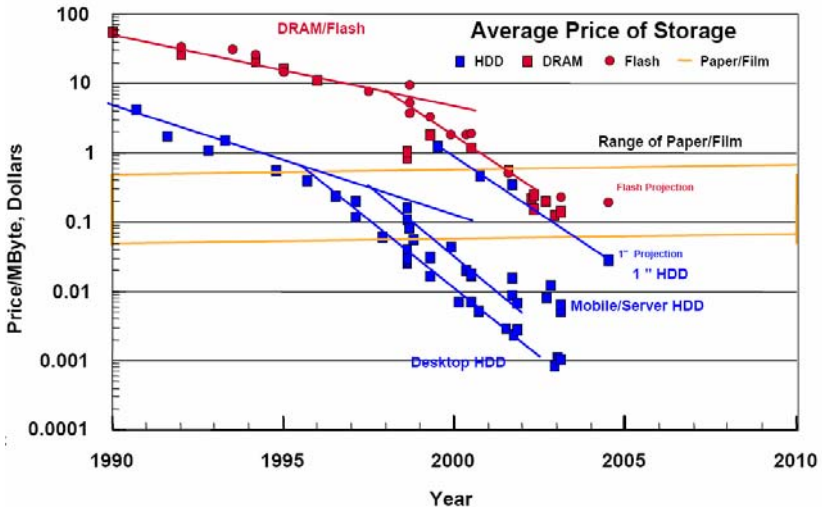

Figure 1.4: The decrease in the cost per MByte of storage capacity in hard disk drive from 1990 to date (From [4])

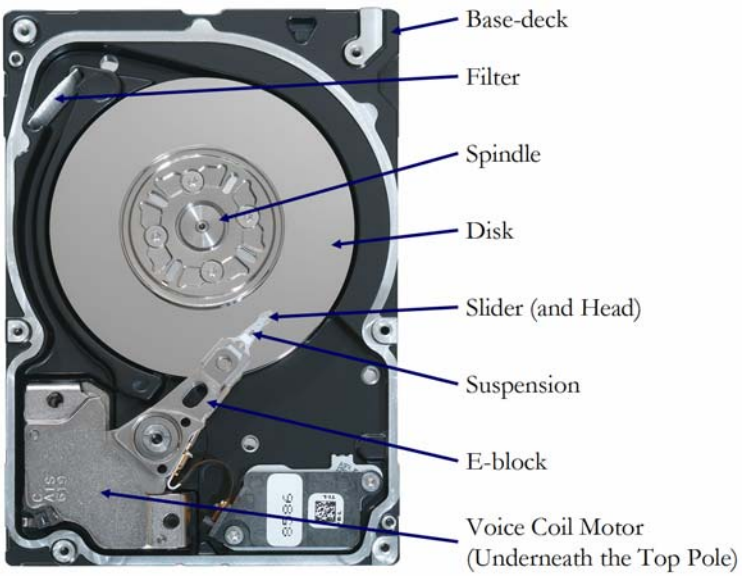

Figure 1.5: Components of a Hard Disk Drive (From [3])

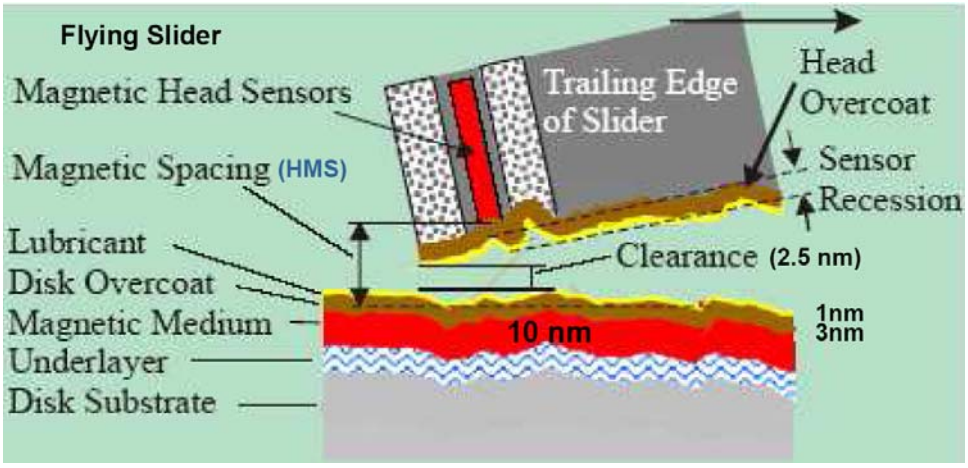

Figure 1.6: The Head to Media Spacing (HMS) in Hard Disk Drives (From [3])

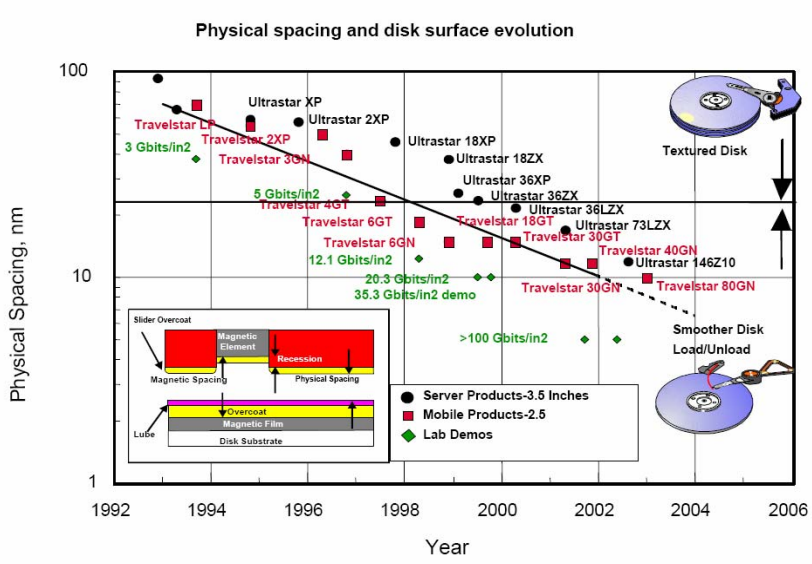

Figure 1.7: The decrease in the mechanical spacing between the slider and the disk from 1992 to date (From [4])

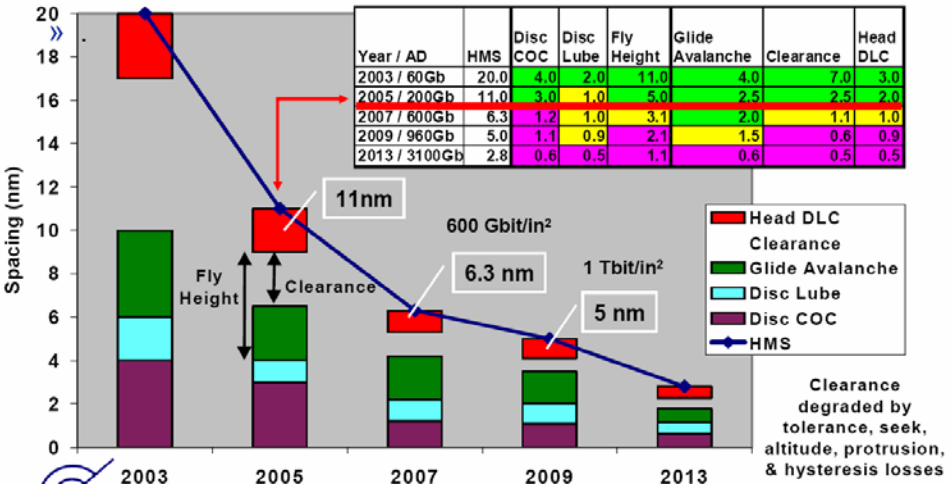

Figure 1.8: The projected head-media spacing and the overcoat/lubricant thickness for 1 Tbit/in^2 recording density (From [5])

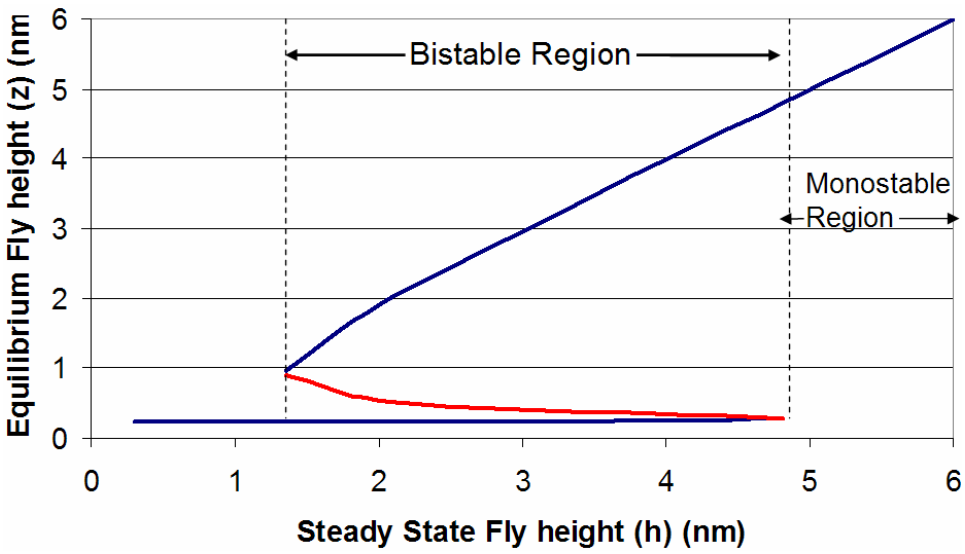

Figure 1.9: Bifurcation diagram using 1 DOF model for V = 0.5 volts with both intermolecular and electrostatic forces included. We observe bistable and monostable regions.

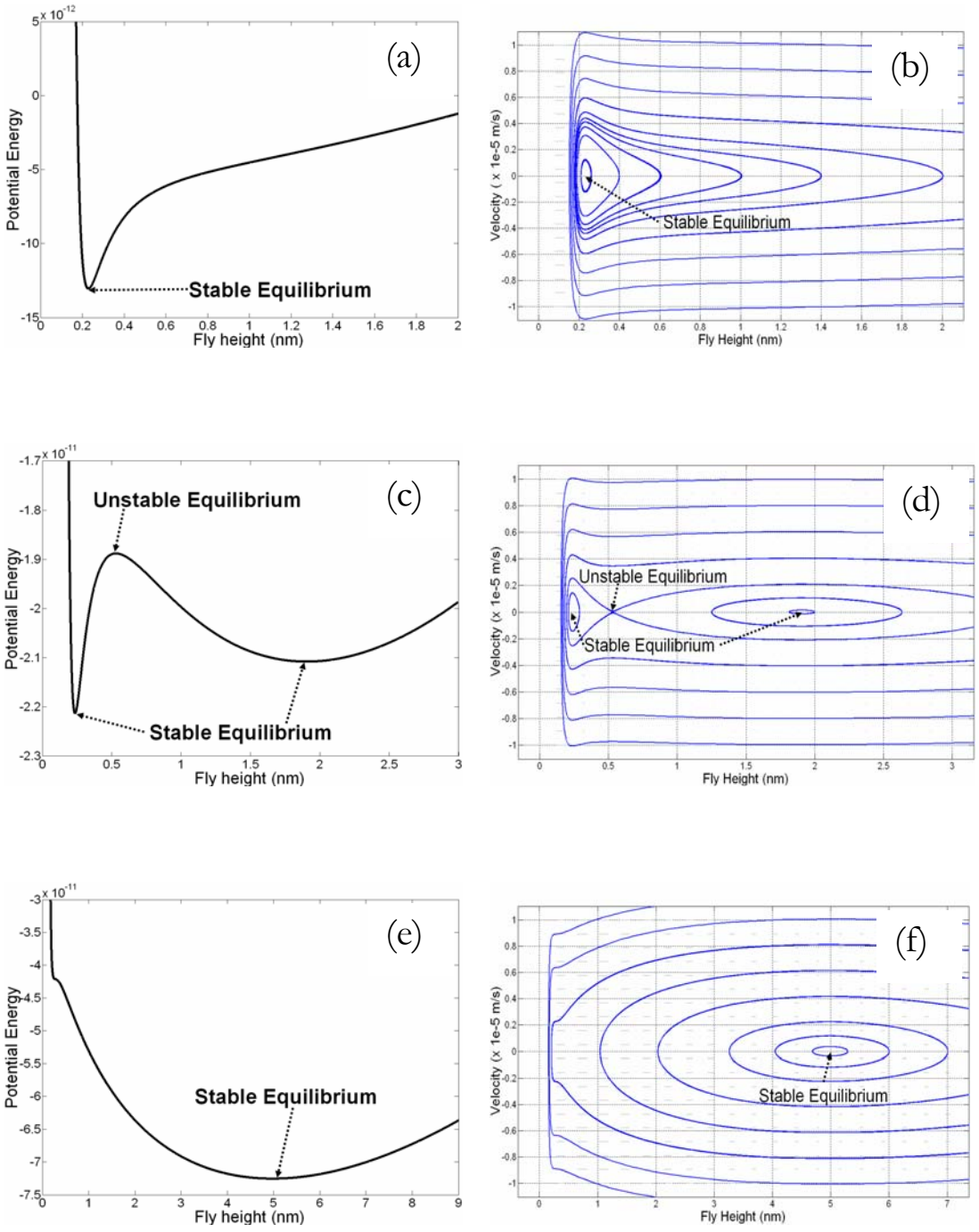

Figure 1.10: Potential energy curve and phase portrait for h = 0.6 nm (diagram (a) and (b)), h = 2.0 nm (diagram (c) and (d)) and h = 5.0 nm (diagram (e) and (f)), respectively.

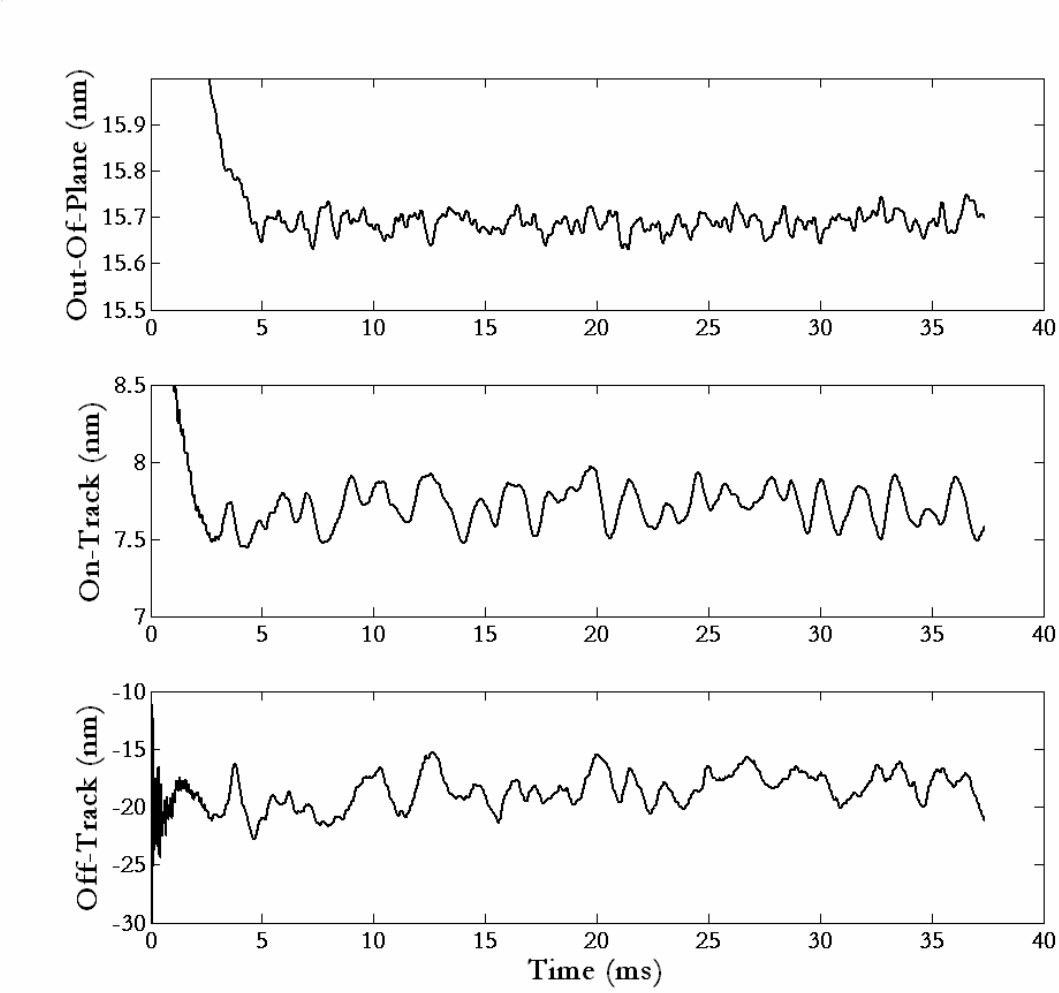

Figure 1.11: Air bearing slider's out-of-plane, on-track and off-track displacements due to aerodynamic forcing of the HSA

CHAPTER 2

THE HARD DISK DRIVE MODEL

2.1 Introduction

In order to predict the system behavior at high disk rotation speeds and at low mechanical spacing we need a reliable model that captures the system dynamics accurately. Researchers in the past have made an attempt to predict the system dynamics using a simple HDI model [7],[8] which includes the slider model and an air bearing model which solves the generalized Reynolds equation. These models completely ignore the dynamics of the HSA and the disk. It has been shown that the system dynamics predicted by these models is significantly different from the actual system response (measured experimentally) during slider-disk contact/impact, aerodynamic forcing on HSA due to disk rotation, shocks, track seek, load-unload etc. In this chapter we propose a way to improve the HDI solvers which attempt to predict the system dynamics by including the HSA and the disk model along with the usual 6 degree of freedom slider model and the air bearing model that solves the generalized Reynolds equation relating the pressure and the spacing distribution between the slider and the disk.

The hard disk drive model used to calculate the slider dynamics is divided into two parts. The first part is the slider-disk-HSA model which captures the structural dynamics of the slider, the disk and the HSA. And the second part is the HDI model that calculates the air bearing, contact, intermolecular and electrostatic forces acting at the HDI. These two models are described below.

2.2 The Slider-Disk-HSA Model

2.2.1 Modeling Techniques

The ongoing increase in the HDD storage capacity with a reduction in the allowable FHM and the TMR has placed stringent structural requirements on HSA design for new generation HDD. Multi-objective topological optimization, which maximizes the resonant frequencies while reducing the effective mass, is used to design the HSA. The HSA has a very complicated structure, and a typical HSA finite element model has over 100,000 degrees of freedom. Similarly, a finite element disk model has over 50,000 DOF. There are several ways to include the HSA and the disk model in HDD solvers.

i. Full finite element HSA and disk model (with over 100,000 and 50,000 degrees of freedom respectively): i.e. to model HSA and disk in a finite element software and model the 6 degrees of freedom slider dynamics and air bearing in FORTRAN. The two solvers will interact at each time step and exchange information regarding displacements, velocities, accelerations, forces and torques of common degrees of freedom. In this case the mass, stiffness and damping matrices of the HSA are of the size 100,000-by-100,000, and inverting and multiplying such large matrices with vectors at each time step makes this method computationally very expensive. There is also a significant amount of time lost due to the exchange of information between the two solvers at each time step. Thus, even though this method accurately models the HSA and disk, it cannot be used due to excessive computation time.

ii. Modal Superposition: Another way is to use a modal superposition method to characterize the dynamic response of the HSA and the disk to excitations. When using the modal superposition method, the responses of the individual modes of the

structure are calculated separately and then combined to produce the total response of the structure. However, this is only applicable to linear transient dynamic analysis. Since the vibrations of the HSA or the disk are of the order of a few nanometers, the nonlinearities in the system do not affect the dynamic analysis. But the modal superposition method is best suited to structures where the lower frequencies dominate the response. Typically, 10 modes will provide good accuracy for these problems. Modal superposition is not suitable for problems such as shock loads or impacts where the higher frequency modes are excited as in the case of the HDD. In this case, the model must capture about 100 or more modes and the cost to calculate this many modes can significantly offset the savings in the transient solution.

iii. Model Reduction: An alternate way to reduce the size of the problem is by using a reduced degree of freedom model with N_{red} degrees of freedom instead of full 100,000 degree of freedom model, where N_{red} is much smaller than total degrees of freedom in the full finite element model. The advantage of using a reduced model over a full model is the reduced size of the mass, stiffness and damping matrices which makes the numerical computations orders of magnitude faster. At the same time with an intelligent selection of the degrees of freedom that will be included in the reduced model, we can easily capture the first 250 eigenvalues and eigenvectors without much loss in accuracy, as will be demonstrated later in this chapter. Moreover, using this technique we can expand the response calculated at the reduced degrees of freedom to calculate the response at the remaining degrees of freedom. Thus, because of its high accuracy and low computational cost, this technique is used here to model the HSA and the disk in the HDD.

2.2.2 Model Order Reduction Techniques

Model reduction is a method to remove unwanted degrees of freedom from a full finite element model of the system. The reduced system captures the first few eigenvalues and eigenvectors of the system with high accuracy, and the computation cost is reduced by orders of magnitude at the same time. This makes this technique very attractive for modeling complex systems for purposes of numerical simulations.

The model order reduction technique was first proposed by Guyan in 1965 [9]. This derivation is summarized in [9],[10],[11]. The governing equation for any linear dynamic system can be written as:

$$M\ddot{X} + C\dot{X} + KX = F \tag{2.1}$$

where M, C and K are the mass/moment-of-inertia, damping and stiffness matrices and X and F are state and force vectors. If the damping forces are assumed to be negligible, the equations of motion of the system can be written as:

$$\begin{bmatrix} M_{mm} & M_{ms} \\ M_{sm} & M_{ss} \end{bmatrix} \begin{Bmatrix} \ddot{X}_m \\ \ddot{X}_s \end{Bmatrix} + \begin{bmatrix} K_{mm} & K_{ms} \\ K_{sm} & K_{ss} \end{bmatrix} \begin{Bmatrix} X_m \\ X_s \end{Bmatrix} = \begin{Bmatrix} F_m \\ 0 \end{Bmatrix} \tag{2.2}$$

Here the state and force vectors are divided into sub-vectors corresponding to master degrees of freedom - subscript m - which are retained in the reduced model, and slave degrees of freedom - subscript s - which are excluded from the reduced model. Similarly the mass and stiffness matrices are also divided into sub-matrices corresponding to master and slave degrees of freedom. Here no constraints are imposed on the selection of the master degrees of freedom, except that all degrees of freedom where external forces are applied must be retained in the reduced model as master degrees of freedom.

Neglecting the inertia term, the second set of equations can be written as:

$$K_{sm}X_s + K_{ss}X_s = 0 \tag{2.3}$$

Thus the state vector for the slave degrees of freedom can be expressed in terms of the state vector for the master degrees of freedom as:

$$X_s = -K_{ss}^{-1}K_{sm}X_m \tag{2.4}$$

Using the above expression we can define the full state vector in terms of the state vector for the master degrees of freedom (X_m) as follows:

$$\begin{Bmatrix} X_m \\ X_s \end{Bmatrix} = T_G \{X_m\} \tag{2.5}$$

where T_G is the Guyan transformation matrix between the full state vector and the master state vector, and it is of the form:

$$T_G = \begin{bmatrix} I \\ -K_{ss}^{-1}K_{sm} \end{bmatrix} \tag{2.6}$$

Thus the reduced mass and stiffness matrices can be expressed in terms of the full mass and stiffness matrices using the Guyan transformation matrix as:

$$\begin{aligned} M_G &= T_G^T M T_G \\ K_G &= T_G^T K T_G \end{aligned} \tag{2.7}$$

In order to achieve a good reduced model that matches the dynamic characteristics of the full model, we must select the master degrees of freedom with as much care as in selecting a good reduction technique. In the Guyan or the static reduction technique it is assumed that

the inertia terms are negligible. This assumption is true only when either the mass associated with a slave degree of freedom is small or the stiffness associated with a slave degree of freedom is very large. Thus, to justify the deletion of the inertia terms, we first consider the ratio K_{ii}/M_{ii}, where K_{ii} and M_{ii} are the i^{th} diagonal terms in the mass and the stiffness matrix corresponding to the i^{th} degree of freedom. This ratio can be identified as the square of the natural frequencies corresponding to the slave degrees of freedom, if all the other degrees of freedom are assumed to be fixed:

$$\omega_{ii}^2 = K_{ii} \Big/ M_{ii} \tag{2.8}$$

The degrees of freedom corresponding to the largest ratios are excluded from the reduced model and the rest of the degrees of freedom are included in the reduced model as the master degrees of freedom. This way we make sure that the dynamic characteristics of the reduced model matches well with the dynamic characteristics of the full model for low frequencies. Obviously, while using this criterion we assume that the coupling effects of the degrees of freedom are negligible. And that is the reason why we do not get a reduced system with the exact same dynamic characteristics as the full model even at low frequencies. But such differences can be minimized by a good choice of master degrees of freedom and reduction technique. More details on the automatic selection of master degrees of freedom can be found in [12].

Based on the criteria described above there are two ways to select and remove the slave degrees of freedom. The first way is to choose all the slave degrees of freedom at once and remove them. This technique will be referred to as the Guyan reduction technique in this

thesis. An alternate way is to remove one slave degree of freedom at each step. This technique will be referred to as the Iterative Guyan reduction technique. The advantage of Iterative Guyan reduction over Guyan reduction is that the effect of each degree of freedom removed is re-distributed to the remaining degrees of freedom, so that in the following step the degree of freedom with the highest K_{ii}/M_{ii} ratio is removed. We will show in the following sections that the Iterative Guyan reduction technique produces a much better reduced system than the Guyan reduction technique.

It should also be pointed out that the state vector obtained at the master degrees of freedom from numerical simulations can be easily expanded to compute the full state vector using the transformation matrix as follows:

$$\begin{Bmatrix} X_m \\ X_s \end{Bmatrix} = T_G \{X_m\} \tag{2.9}$$

The technique described above is arguably the simplest and the most popular reduction technique to date. This technique is sometimes also referred to as the static reduction technique because the inertia terms are neglected in deriving the transformation matrix. O'Callaghan in 1989 proposed a method to overcome this restriction by taking into account the system inertia effects while deriving the transformation matrix [13]. This technique, known as the improved reduced system (IRS), has an extra term added to the transformation matrix T_G to account for the inertial effects. The standard IRS method derivation using binomial series expansion in frequency was later proposed by Gordis in 1992 [14]. This derivation can be summarized as follows [15],[16].

For a sinusoidal excitation with frequency ω the second set of equations from equation (2.2) can be expressed in the form:

$$\begin{bmatrix} K_{sm} & K_{ss} \end{bmatrix} \begin{Bmatrix} X_m \\ X_s \end{Bmatrix} = \omega^2 \begin{bmatrix} M_{sm} & M_{ss} \end{bmatrix} \begin{Bmatrix} X_m \\ X_s \end{Bmatrix} \tag{2.10}$$

After rearranging the terms and using the binomial expansion, the state vector for the slave degrees of freedom can be expressed as a function of the state vector for the master degrees of freedom as follows:

$$X_s = -\left[K_{ss} - \omega^2 M_{ss}\right]^{-1} \left[K_{sm} - \omega^2 M_{sm}\right] X_m \tag{2.11}$$

where the inverse matrix can be calculated as follows:

$$\begin{aligned} \left[K_{ss} - \omega^2 M_{ss}\right]^{-1} &= -K_{ss}^{-1}\left[I - \omega^2 M_{ss} K_{ss}^{-1}\right]^{-1} \\ &= -K_{ss}^{-1}\left[I + \omega^2 M_{ss} K_{ss}^{-1} + O\left(\omega^4\right)\right] \end{aligned} \tag{2.12}$$

Substituting the above expression for the matrix inverse into equation (2.11), we get:

$$\begin{aligned} X_s &= -K_{ss}^{-1}\left[I + \omega^2 M_{ss} K_{ss}^{-1} + O\left(\omega^4\right)\right]\left[K_{sm} - \omega^2 M_{sm}\right] X_m \\ &= -K_{ss}^{-1}\left[K_{sm} + \omega^2\left(M_{ss} K_{ss}^{-1} K_{sm} - M_{sm}\right) + O\left(\omega^4\right)\right] X_m \end{aligned} \tag{2.13}$$

where $O(\omega^4)$ denotes an error of order ω^4.

Similarly the reduced mass and stiffness matrices, M_R and K_R, respectively, computed using the Guyan reduction satisfies:

$$\begin{aligned} \omega^2 M_G X_m &= K_G X_m \\ \omega^2 X_m &= M_G^{-1} K_G X_m \end{aligned} \tag{2.14}$$

where ω and X_m are the eigenvalues and eigenvectors respectively. Substituting $\omega^2 X_m$ from the above equation into equation (2.13) we obtain:

$$
\begin{aligned}
X_s &= -\left[K_{ss}^{-1}K_{sm}X_m + K_{ss}^{-1}\left(M_{ss}K_{ss}^{-1}K_{sm} - M_{sm}\right)\left(\omega^2 X_m\right)\right] \\
&= -\left[K_{ss}^{-1}K_{sm}X_m + K_{ss}^{-1}\left(M_{ss}K_{ss}^{-1}K_{sm} - M_{sm}\right)\left(M_G^{-1}K_G X_m\right)\right] \\
&= -\left[K_{ss}^{-1}K_{sm} + K_{ss}^{-1}\left(M_{ss}K_{ss}^{-1}K_{sm} - M_{sm}\right)M_G^{-1}K_G\right]X_m
\end{aligned}
\tag{2.15}
$$

Using the above expression we can define the full state vector in terms of X_m as follows:

$$
\begin{Bmatrix} X_m \\ X_s \end{Bmatrix} = T_{IRS}\{X_m\} \tag{2.16}
$$

where T_{IRS} is the transformation matrix based on the IRS technique, between the full state vector and the master degree of freedom state vector, and it is of the form:

$$
\begin{aligned}
T_{IRS} &= \begin{bmatrix} I \\ -K_{ss}^{-1}K_{sm} + K_{ss}^{-1}\left(-M_{ss}K_{ss}^{-1}K_{sm} + M_{sm}\right)M_G^{-1}K_G \end{bmatrix} \\
&= \begin{bmatrix} I \\ -K_{ss}^{-1}K_{sm} \end{bmatrix} + \begin{bmatrix} 0 \\ K_{ss}^{-1}\left(-M_{ss}K_{ss}^{-1}K_{sm} + M_{sm}\right) \end{bmatrix} M_G^{-1}K_G \\
&= T_G + \begin{bmatrix} 0 & 0 \\ 0 & K_{ss}^{-1} \end{bmatrix} M T_G M_G^{-1}K_G \\
&= T_G + ZMT_G M_G^{-1}K_G
\end{aligned}
\tag{2.17}
$$

where the matrix Z is:

$$
Z = \begin{bmatrix} 0 & 0 \\ 0 & K_{ss}^{-1} \end{bmatrix} \tag{2.18}
$$

Thus the reduced mass and stiffness matrices can be expressed in terms of the full mass and stiffness matrices using the IRS transformation matrix as:

$$
\begin{aligned}
M_{IRS} &= T_{IRS}^T M T_{IRS} \\
K_{IRS} &= T_{IRS}^T K T_{IRS}
\end{aligned}
\tag{2.19}
$$

To further improve the accuracy of the reduced model Friswell proposed an Iterated IRS

technique [15],[16]. As the name suggests this method follows an iterative technique to update the transformation matrix, which in turn is used to update the reduced mass and stiffness matrices. In this technique the transformation matrix for the first iteration is the same as the IRS technique given by equations (2.17). For the subsequent iterations the transformation matrix is calculated as follows:

$$T_{IRS,i+1} = T_G + ZMT_{IRS,i}M_{IRS,i}^{-1}K_{IRS,i} \tag{2.20}$$

And the updated mass and stiffness matrices are given by the equations:

$$\begin{aligned} M_{IRS,i+1} &= T_{IRS,i+1}^T MT_{IRS,i+1} \\ K_{IRS,i+1} &= T_{IRS,i+1}^T KT_{IRS,i+1} \end{aligned} \tag{2.21}$$

Later Friswell proved that if a good choice of the master degrees of freedom is made, then in most cases the iteration converges. He also proved that if the iteration converges then the eigenvalues and eigenvectors of the reduced system converge to the first few eigenvalues and eigenvectors of the full system. A detailed proof of convergence can be found in [15],[16].

All of the reduction techniques presented above modify the dynamic characteristics of the full finite element model. It has been observed that the frequencies of the reduced model are slightly higher that the frequencies of the full model. O'Callahan in 1989 proposed a new method that can preserve the dynamic characteristics of the full model for selected modes of interest [17]. This technique is called as System Equivalent Reduction Expansion Process (SEREP). Friswell proved that SEREP and the Iterative IRS techniques are equivalent [15],[16], thus SEREP will not be discussed in this chapter. The reader can find out more about SEREP in [11],[17].

All of the methods discussed above are applicable to linear systems only. Friswell demonstrated the use of linear model reduction techniques to investigate the dynamics of structures with local nonlinearities. A good discussion on reduction techniques for systems with local nonlinearities can be found in [18],[19].

2.2.3 Estimating the Accuracy of the Reduced Model

A good reduction technique is one that gives a reduced model with dynamic characteristics close to that of the full model for the low frequencies. Two criteria have been used in this study to compare the various reduction techniques we have discussed in above section.

a) Percentage error of natural frequencies (PE): One requirement of a good reduction technique is that the reduced model should have similar eigenvalues (or the natural frequencies) as the first few eigenvalues (or the natural frequencies) of the full model. Thus, the percentage error between the natural frequencies of the full and the reduced model is used as a criterion to check the accuracy of the reduction technique.

$$PE\left(\omega_i^r\right) = \left|\frac{\omega_i^r - \omega_i^f}{\omega_i^f}\right| \times 100\% \quad \forall i = \{1,2,...n_{red}\} \tag{2.22}$$

Here ω_i^r and ω_i^f are the i^{th} natural frequency of the reduced and the full model, respectively.

b) Correlation coefficient for modal vectors (CCFMV): Comparison of eigenvalues or natural frequencies is not enough to insure the accuracy of the reduced model. The comparison of eigenvectors or mode shapes is also important. To estimate the accuracy of the modal vectors the correlation coefficient between the estimated eigenvector based on the

reduced model (Φ_i^r) and the exact eigenvector based on the full model (Φ_i^f) is calculated as follows:

$$CCFMV\left(\Phi_i^r, \Phi_i^f\right) = \frac{\Phi_i^{rT}.\Phi_i^f}{\left\{\left(\Phi_i^{rT}.\Phi_i^r\right)\left(\Phi_i^{fT}.\Phi_i^f\right)\right\}^{1/2}} \tag{2.23}$$

We observe that the eigenvector for the reduced model is of the form

$$\Phi^r = \begin{bmatrix} \Phi_m^r \\ \Phi_s^r \end{bmatrix} \tag{2.24}$$

where Φ_m^r and Φ_s^r are the eigenvectors for the master and slave degrees of freedom, respectively. It is fairly straight forward to calculate Φ_m^r from the reduced mass and stiffness matrices, but Φ_s^r must be estimated. The most straight forward way to estimate Φ_s^r is by using the Guyan transformation matrix, usually referred to as the exact mode expansion [11]:

$$\Phi^r = \begin{bmatrix} \Phi_a^r \\ \Phi_d^r \end{bmatrix} = \begin{bmatrix} I \\ -K_{dd}^{-1}K_{da} \end{bmatrix} \Phi_a^r = T_G \Phi_a^r \tag{2.25}$$

Other mode expansion formulas often used to estimate the eigenvector for the slave degrees of freedom have been proposed by Kidder and Miller. A brief introduction of their expansion formulas can be found in [11],[20],[21].

A CCFMV value close to 1 implies that the two eigenvectors are well correlated and thus the reduced model is a good approximation of the full model for lower eigenmodes. But a CCFMV value close to 0 suggests that the two vectors are poorly correlated and the reduced model is not a good approximation of the full model.

2.2.4 Comparison of Reduction Techniques

The HSA and disk models we used to compare the reduction techniques are shown in Figure 2.1 and Figure 2.2, respectively. The full finite element HSA and disk models have 143,756 and 12,672 degrees of freedom, respectively. The reduction techniques discussed above are used to obtain reduced models for the HSA and the disk with 250 and 100 degrees of freedom, respectively. The eigenvalues and eigenvectors of these reduced models are computed and compared with the first 250 and 100 eigenvalues and eigenvectors of the full HSA and disk models, respectively.

Figure 2.3 plots the HSA frequencies in KHz and Figure 2.4 plots the percentage error in the HSA frequencies of the reduced models with 250 degrees of freedom when compared with the first 250 frequencies of the full HSA model that has 143,756 degrees of freedom. We observe that the 250 frequencies for the HSA reduced model obtained using Iterative IRS is indistinguishable from the first 250 frequencies of full HSA model. The frequencies for the reduced model obtained using the Iterative Guyan technique are also close to the first 50 HSA frequencies, but the error increases for higher HSA frequencies. It can also be observed that the percentage error in frequencies for the reduced models obtained using IRS and Guyan techniques is large and therefore such reduced models cannot be used for modeling the HSA in hard disk drives, unless reduced models with over 1000 degrees of freedom are used.

Most commercially available finite element packages also have built-in reduction techniques. The HSA frequencies for the 250 degree of freedom reduced model obtained using ANSYS is plotted in Figure 2.3, and the corresponding percentage error term is plotted in Figure 2.4.

The error for the reduced model obtained using ANSYS is very large, and so use of such a reduced model will compromise the accuracy of the numerical solution.

Figure 2.5 plots the correlation coefficient for the modal vectors (CCFMV) for the reduced models obtained using Guyan, Iterative Guyan, IRS and Iterative IRS. We observe that the CCFMV is always close to 1 for the reduced model obtained using the Iterative IRS technique. But the reduced models obtained using the Guyan, Iterative Guyan and IRS reduction techniques are not as good, especially at higher frequencies. This implies that the Iterative IRS is the most suitable technique for obtaining reduced models for complex structures like HSA.

Similar, analysis is carried out for the disk model. Figure 2.6 plots the disk frequencies in KHz and Figure 2.7 plots the percentage error in disk frequencies of the reduced models with 100 degrees of freedom when compared with the first 100 frequencies of the full disk model that has 12,672 degrees of freedom. We observe that the 100 frequencies for the disk reduced model obtained using the Iterative IRS matches very well with the first 100 frequencies of the full disk model. The frequencies for the reduced model obtained using the Iterative Guyan technique also has small error for the first 25 disk frequencies, but the error increases for higher disk frequencies. It can also be observed that the percentage error in frequencies for the reduced models obtained using the IRS and Guyan techniques is large and therefore such reduced models cannot be used for modeling the disk in HDD solvers, unless reduced disk models with over 500 degrees of freedom are used.

Figure 2.8 plots the correlation coefficient for the modal vectors (CCFMV) for the reduced

disk models obtained using the Guyan, Iterative Guyan, IRS and Iterative IRS methods. We observe that the CCFMV is always close to 1 for reduced model obtained using the Iterative IRS technique. But the reduced models obtained using Guyan, Iterative Guyan and IRS reduction techniques are not as good, especially at higher frequencies. This again implies that the Iterative IRS is the most suitable technique for obtaining reduced models for complex structures like the HSA and the disk.

2.3 The Head-Disk Interface Model

The mechanical spacing between the slider and the disk is of the order of a few nanometers. An extremely thin air bearing is formed between the slider and the rotating disk at such small spacing which provides the necessary equilibrium lifting force, so the slider can fly at the desired height. Conventionally, Reynolds equation [22] based on the continuum assumption has been used to model this air bearing.

$$\frac{\partial}{\partial X}\left(PH^3 \frac{\partial P}{\partial X} - \Lambda_x PH \right) + \frac{\partial}{\partial Y}\left(PH^3 \frac{\partial P}{\partial Y} - \Lambda_y PH \right) = \sigma \frac{\partial}{\partial T}(PH) \tag{2.26}$$

Here P and H are dimensionless pressure and spacing variation between the head and the disk. Λ_x, Λ_y and σ are the bearing numbers in the X and Y directions and the squeeze number.

But the conventional theory of air lubricated bearings assumes the fluid to be a continuous medium. This assumption, however, is limited to the flows where the Knudsen number, Kn – defined as the ratio of the molecular mean free path of the air and the characteristic dimension of the flow passage – is << 1 [23]. The fluid flow phenomenon in an air lubricated bearing in hard disk drives fails to satisfy this assumption. Rarefaction effects

become increasingly important as the mechanical spacing between the slider and the disk decreases and the Knudsen number increases in the air lubricated bearings in hard disk drives, and thus pressure drop, shear stress and corresponding mass flow rates cannot be predicted from flow models based on the continuum hypothesis.

Thus slip flow air bearing models have been proposed by several researchers to overcome the shortcomings of the continuum based Reynolds equation [24],[25],[26],[27]. In the slip flow regime the flow is governed by the Navier-Stokes equation and rarefaction effects are modeled through the partial slip at the disk surface using Maxwell's velocity slip and von Smoluchowski's temperature jump conditions. The occurrence of slip at the boundaries implies that the velocity gradient in the film is decreased. Thus the apparent viscosity of the air is reduced and the load carrying capacity of the slider is diminished.

To model the relationship between the air bearing between the slider and the rotating disk we use the following generalized Reynolds equation model base on the Fukui-Kaneko correction [28],[29]:

$$\frac{\partial}{\partial X}\left(QPH^3\frac{\partial P}{\partial X}-\Lambda_x PH\right)+\frac{\partial}{\partial Y}\left(QPH^3\frac{\partial P}{\partial Y}-\Lambda_y PH\right)=\sigma\frac{\partial}{\partial T}(PH) \tag{2.27}$$

$$Q=f\left(\frac{K_n}{PH}\right)$$

Here Q is the flow factor assuming the F-K correction and K_n is the Knudsen number.

As discussed earlier, in order to increase the linear bit density the mechanical spacing between the slider and the disk should be reduced. When the slider is flying at mechanical separations less than 5 nm several forces such as the intermolecular and the electrostatic

forces become significant. Thus these forces have also been included in the HDI model. The intermolecular forces acting at the HDI can be expressed as [6]:

$$F_{IMF}(z) = -\frac{A}{6\pi}\iint_{\substack{Rect\\Area}}\frac{dx\,dy}{z^3} + \frac{B}{45\pi}\iint_{\substack{Rect\\Area}}\frac{dx\,dy}{z^9} \tag{2.28}$$

And, the electrostatic forces acting at the HDI can be expressed as [6]:

$$F_{ELEC}(z) = -\frac{\varepsilon_o k_e V^2}{2}\iint_{\substack{Rect\\Area}}\frac{dx\,dy}{z^2} \tag{2.29}$$

Here A is the Hamaker constant and B is another constant. The Hamaker constant is a function of the refractive index, dielectric constant and the thickness of the various material layers at the HDI. A typical value of the Hamaker constant (A) for representative values of diamond like carbon (DLC) layer thicknesses on the slider and the disk and lubricant layer thickness on the disk is $8.9*10^{-19}$J [6]. The value of the constant B is taken as $1*10^{-76}$Jm^6 [6]. Similarly, ε_o, k_e and V are the permittivity constant ($8.85*10^{-12}$ farad/m), dielectric constant of the medium (1 for air) and the potential difference between the slider and the disk. The derivation of intermolecular and electrostatic force model will be discussed in detail in chapter 3.

2.4 The Hard Disk Drive Model

The hard disk drive model used to calculate the slider dynamics is divided into two parts. As discussed earlier, the first part is the slider-disk-HSA model which captures the structural dynamics of the slider, the disk and the HSA. And the second part is the HDI model that calculates the air bearing, contact, intermolecular and electrostatic forces acting at the HDI.

Thus in order to calculate the flying characteristics of the air bearing slider, we considered a

reduced disk and HSA model which includes 6 degrees of freedom of the slider.

$$M_{red}\frac{d^2X_m}{dt^2}+C_{red}\frac{dX_m}{dt}+K_{red}X_m=F_m \tag{2.30}$$

Here X_m and F_m are the state and force vectors at the master degrees of freedom, which includes the 6 degrees of freedom of the slider. M_{red} and K_{red} are the reduced mass and stiffness matrices. The damping matrix C_{red}, is computed assuming proportional (Rayleigh) damping.

$$C_{red}=\alpha_1 M_{red}+\alpha_2 K_{red} \tag{2.31}$$

Here α_1 and α_2 are chosen such that the damping values at 10 Hz and at 50 KHz are 0.1%.

To model the relationship between the pressure distribution and the HDI spacing we use the generalized Reynolds equation (2.27). And the intermolecular and electrostatic forces are modeled using equation's (2.28) and (2.29), respectively.

The equation's (2.27) and (2.30) are used to calculate the dynamic response of the air bearing slider. The Newmark-Beta method is used to solve the governing equations of the slider, the HSA and the disk. The Reynolds equation is solved using Patankar's finite volume technique. Further details about the Patankar's finite volume technique can be found in [30].

2.5 Dynamic Analysis and Convergence Results

We now illustrate the application of the reduced HSA models, computed using the Iterative IRS technique, for dynamic simulations in hard disk drives. Two sets of simulations are carried out to prove the convergence with reduced models. For the first example we did four simulations with 250, 500, 1000 and 5000 degrees of freedom reduced models and a fifth

simulation with just a slider model (i.e. 6 degree of freedom reduced model). The disk rotation speed is 7200 RPM and the slider is at the middle diameter (MD) location. The forces/moments acting at the HDI are the air bearing forces/moments, contact forces/moments and the intermolecular forces/moments. Air flow-induced forcing on the HSA due to disk rotation is not applied in this case. Thus the forces/moments are acting only at the slider's 6 degrees of freedom in these simulations. These simulations are started at certain initial displacements different from the steady state values. Thus the slider and the HSA undergo some transients before converging to the steady state.

Table 2.1 shows the steady state displacements along all 6 slider degrees of freedom. The steady state displacements are exactly the same for the 6, 250, 500, 1000 and 5000 degrees of freedom models. This is because at steady state with no dynamic forcing, the velocity and acceleration state vectors are zero, and thus the inertia and damping terms are zero. This implies that at steady state, with no dynamic forcing, the derivation based on neglecting the inertia and damping forces does not compromise the accuracy of the reduced model. And thus the steady state values are exactly the same for all the reduced models.

Here we should point out that the numerical simulations with the 6 and 250 degree of freedom models converged with a time step of 1E-6 seconds, but the numerical solutions with 500, 1000 and 5000 degrees of freedom required time steps of 1E-7 sec, 1E-8 sec and 5E-10 sec for convergence, respectively. This indicates that smaller models are better if they have sufficient accuracy because the computational cost can be drastically reduced.

The displacements are not the same for transient dynamics for all five reduced models.

Figure 2.9 plots the power spectra of the slider displacements along all 6 degrees of freedom. We observe that the power spectra obtained using the 250, 500, 1000 and 5000 degrees of freedom reduced models are exactly similar for frequencies up to 100 KHz. This is because these models capture the dynamic characteristics of the full HSA model for all frequencies up to and beyond 100 KHz. But the power spectra obtained using the 6 degree of freedom reduced HSA model is quite different. This is because the 6 degree of freedom reduced model captures only 6 frequencies and thus the dynamic response is quite different. Figure 2.10 plots the contribution to the RMS in (a) out-of-plane, (b) on-track, (c) off-track, (d) roll, (e) pitch and (f) yaw by different frequency bands for the 6, 250, 500, 1000 and 5000 degrees of freedom reduced models. We again observe that the RMS contribution in all 6 slider degrees of freedom are very similar for the 250, 500, 1000 and 5000 degrees of freedom reduced models, but the 6 degree of freedom reduced model differs significantly in all frequency bands especially along the out-of-plane, on-track, off-track and yaw directions. This shows that 250 degrees of freedom reduced HSA model is sufficiently accurate for dynamic simulations without much increase in the computation cost.

For the second example we did four simulations using the 250, 500, 1000 and 5000 degrees of freedom reduced models. The disk rotation speed is 7200 RPM and the slider is at the MD location. The forces/moments acting at the HDI are the air bearing forces/moments, contact forces/moments and the intermolecular forces/moments. In this case the air flow-induced forcing due to disk rotation, computed by Kirpekar [31],[32],[33] using a commercial computational fluid dynamics package, is applied on the HSA. Due to this dynamic forcing on the HSA, all of the master degrees of freedom oscillate about a mean. Figure 2.11 plots the power spectra of the slider displacements along all 6 degrees of freedom. We again

observe that the power spectra obtained using the 250, 500, 1000 and 5000 degrees of freedom reduced models are very similar for frequencies up to 100 KHz. This is because these models capture the dynamic characteristics of the full HSA model for all frequencies up to and beyond 100 KHz. Figure 2.12 plots the contributions to the RMS in (a) out-of-plane, (b) on-track, (c) off-track, (d) roll, (e) pitch and (f) yaw by different frequency bands for the 250, 500, 1000 and 5000 degrees of freedom reduced models. We again observe that the RMS contributions in all 6 slider degrees of freedom are very similar for the 250, 500, 1000 and 5000 degrees of freedom reduced models. This again shows that 250 degrees of freedom reduced HSA model is sufficiently accurate for complex dynamic simulations with air flow-induced forcing acting on the HSA.

2.6 Conclusions

There is a need for a solver that can reliably predict the system behavior at low mechanical spacing due to various disturbances. In this chapter we presented a new numerical simulator developed to model slider dynamics in a HDD. This simulator consists of a disk and HSA model along with the usual 6-DOF slider and air bearing models. Various model order reduction techniques used to model the disk and HSA are presented in this chapter. Several metrics developed to measure the accuracy of the reduced model are also discussed. The Iterative IRS is shown to be the best technique to obtain reduced HSA and disk models with highly accurate dynamic characteristics for the first few modes. The increase in the computation cost is also negligible. We also illustrated the application of the reduced HSA models, computed using the Iterative IRS technique, for dynamic simulations in hard disk drives.

2.7 Tables

Table 2.1: Steady state values of slider displacements with 6, 250, 500, 1000 and 5000 degrees of freedom HSA model

Min Flying Height (nm)	15.4807
On-Track Displacement (nm)	7.9347
Off-Track Displacement (nm)	-1.8175
Roll (μrad)	17.2782
Pitch (μrad)	86.7156
Yaw (μrad)	-0.1344

2.8 Figures

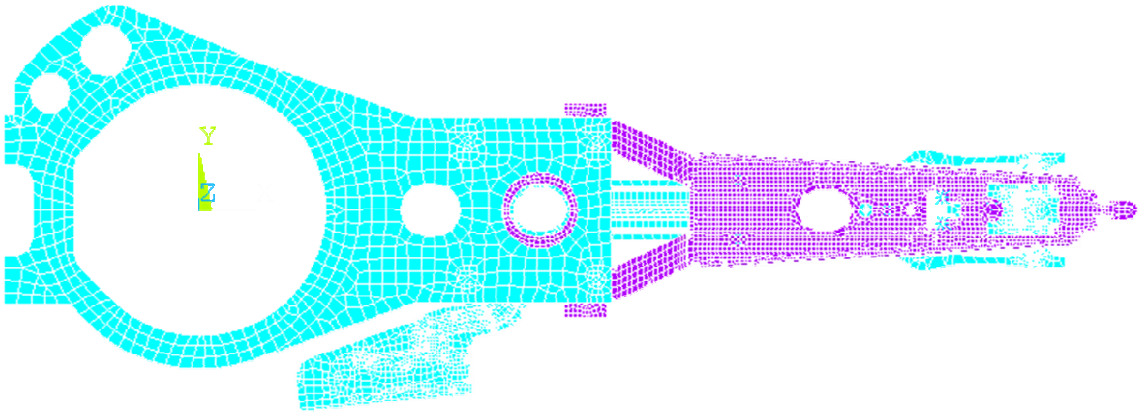

Figure 2.1: Full finite element model of the HSA with 143,756 degrees of freedom

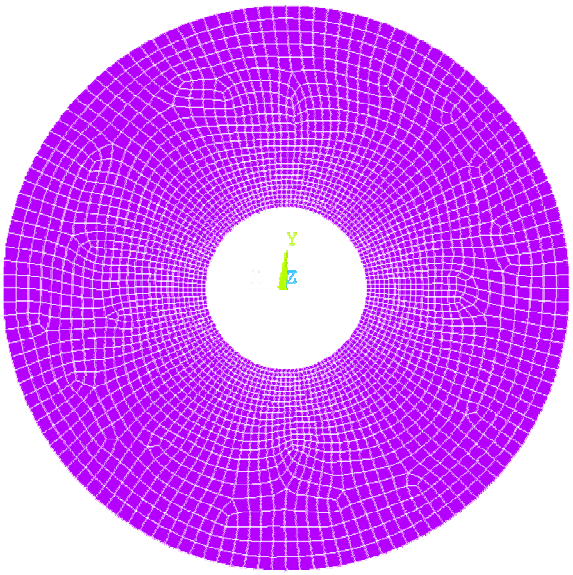

Figure 2.2: Full finite element model of the disk with 12,672 degrees of freedom

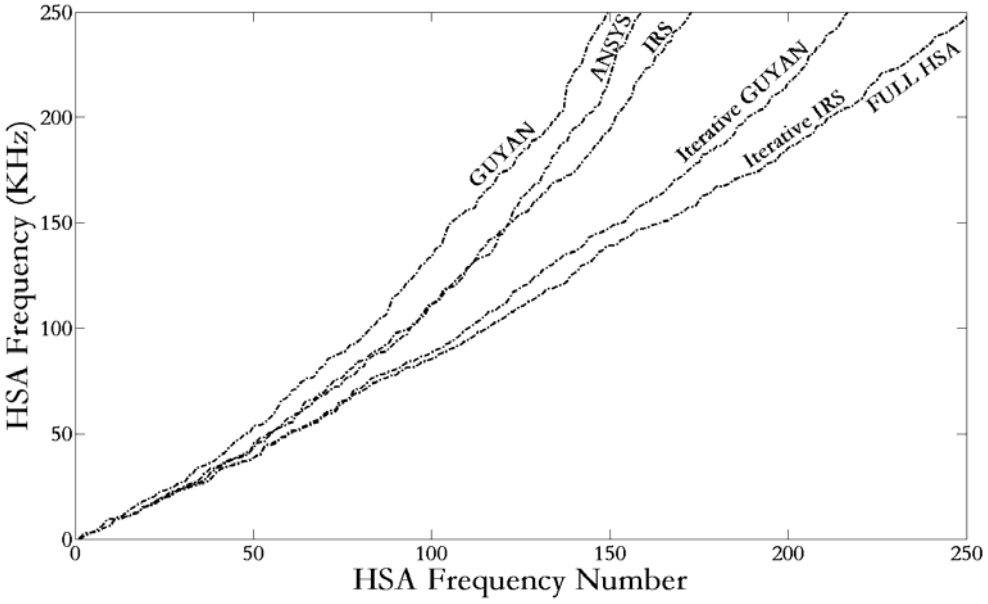

Figure 2.3: Frequencies of Full HSA and reduced HSA model

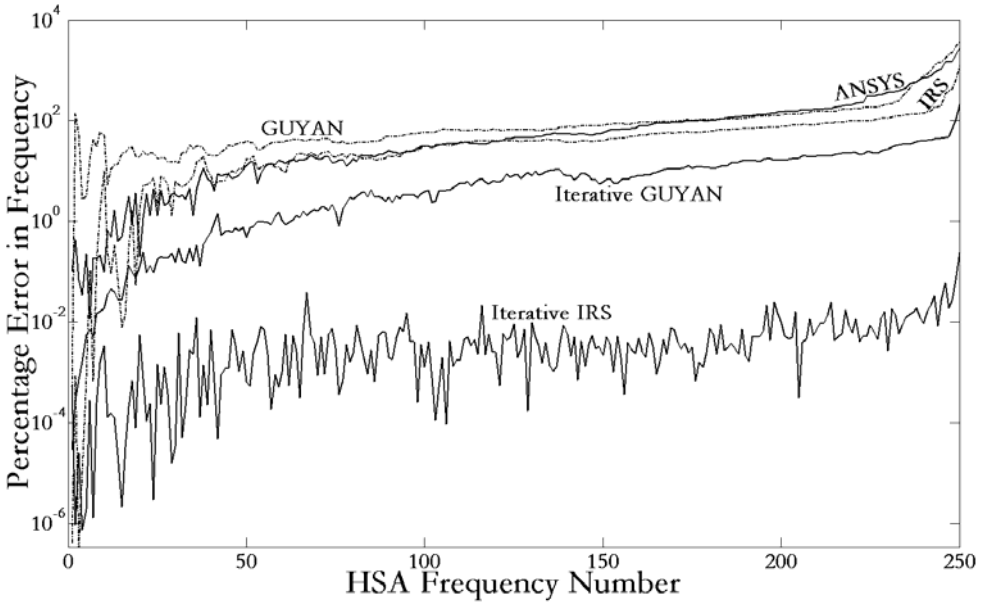

Figure 2.4: Percentage Error in frequencies of reduced HSA model

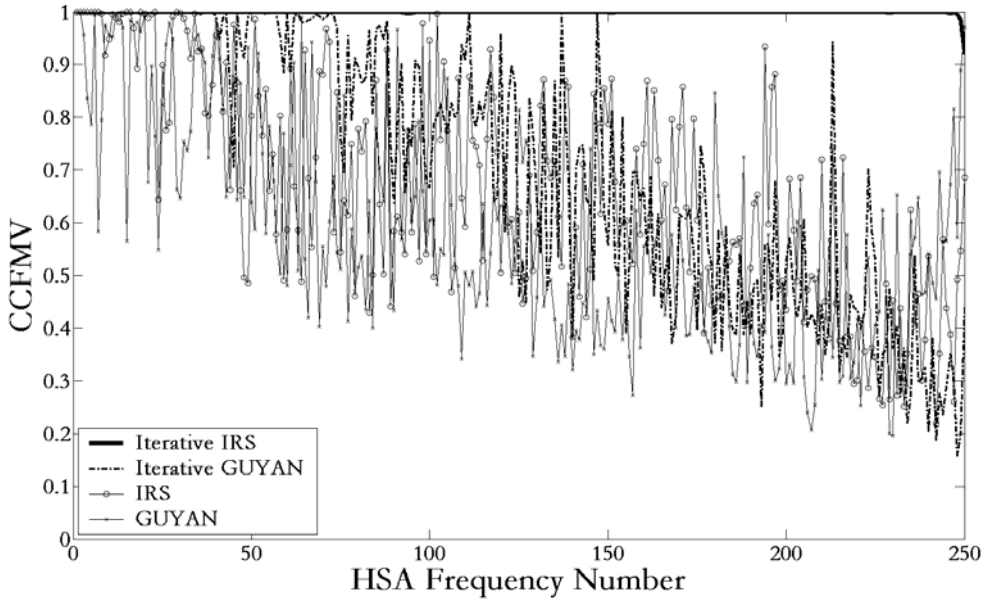

Figure 2.5: CCFMV of reduced HSA model

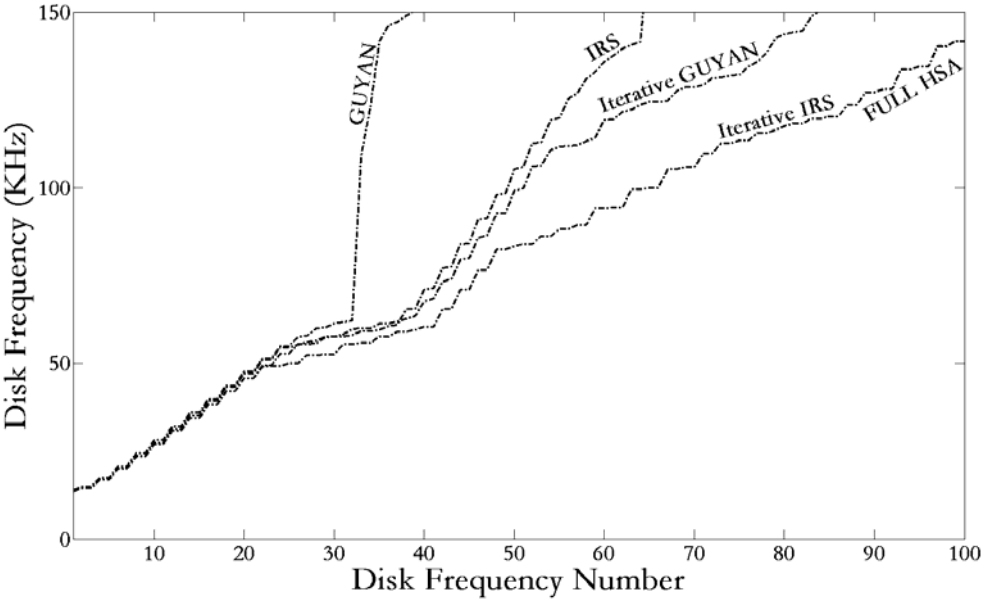

Figure 2.6: Percentage Error in frequencies of reduced disk model

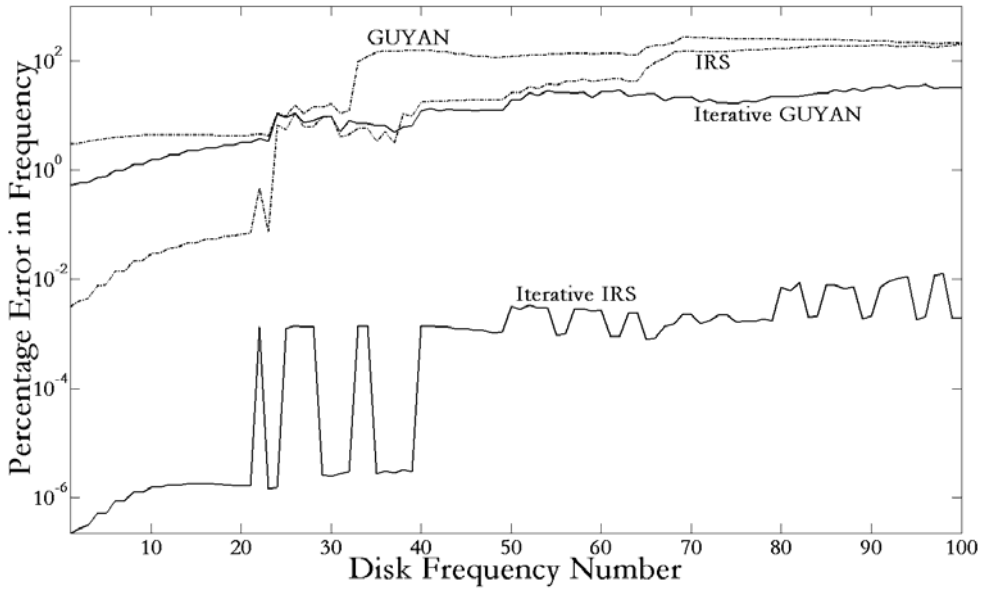

Figure 2.7: Percentage Error in frequencies of reduced disk model

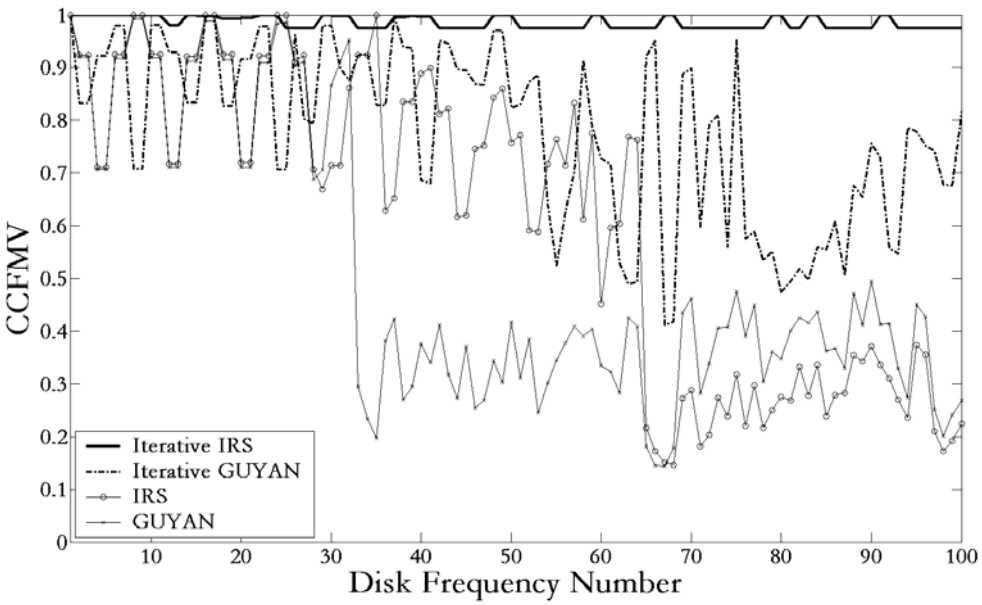

Figure 2.8: CCFMV of reduced disk model

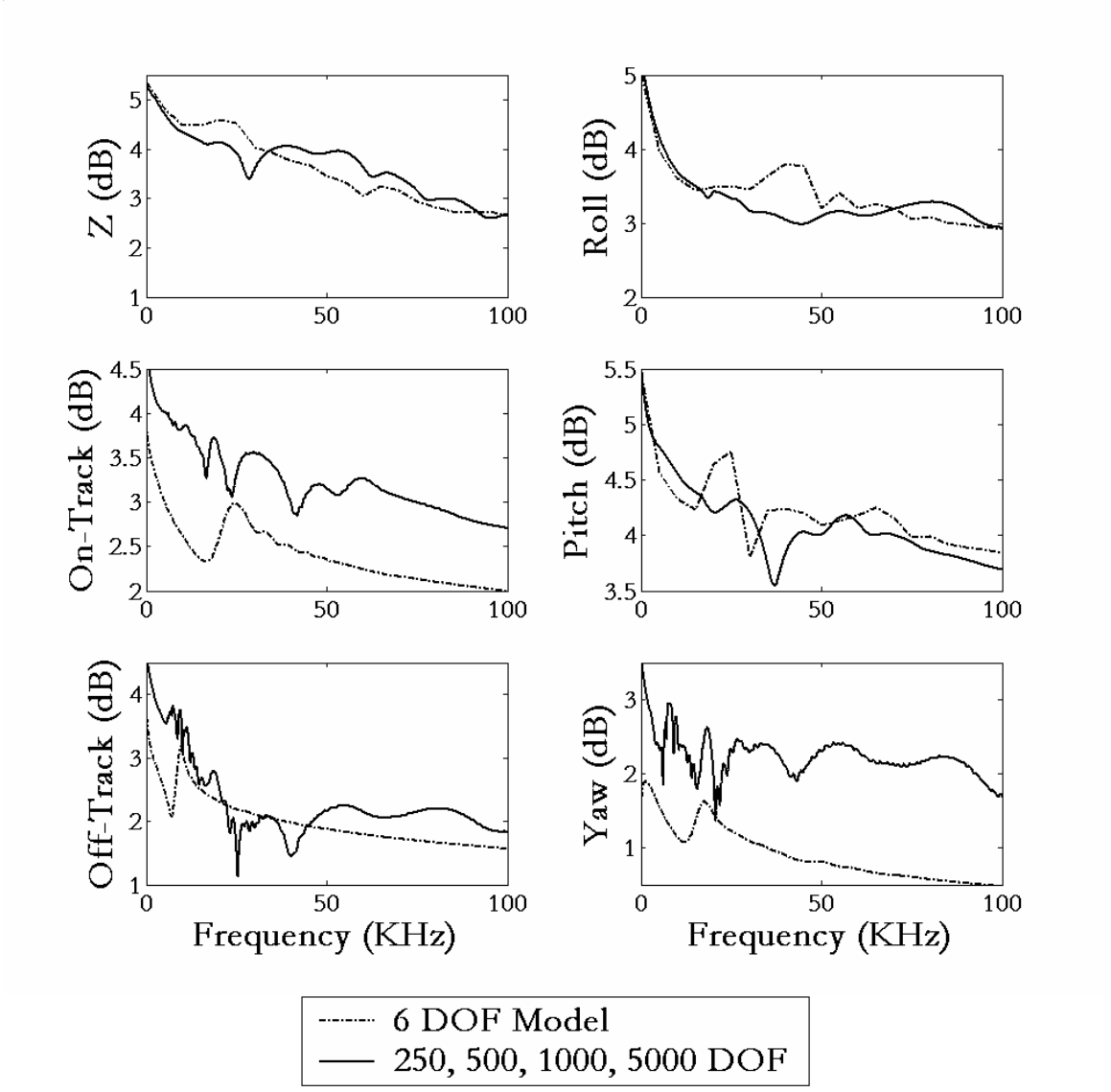

Figure 2.9: Power spectra of the slider displacements in all 6 degrees of freedom for the 6, 250, 500, 1000 and 5000 degrees of freedom reduced models

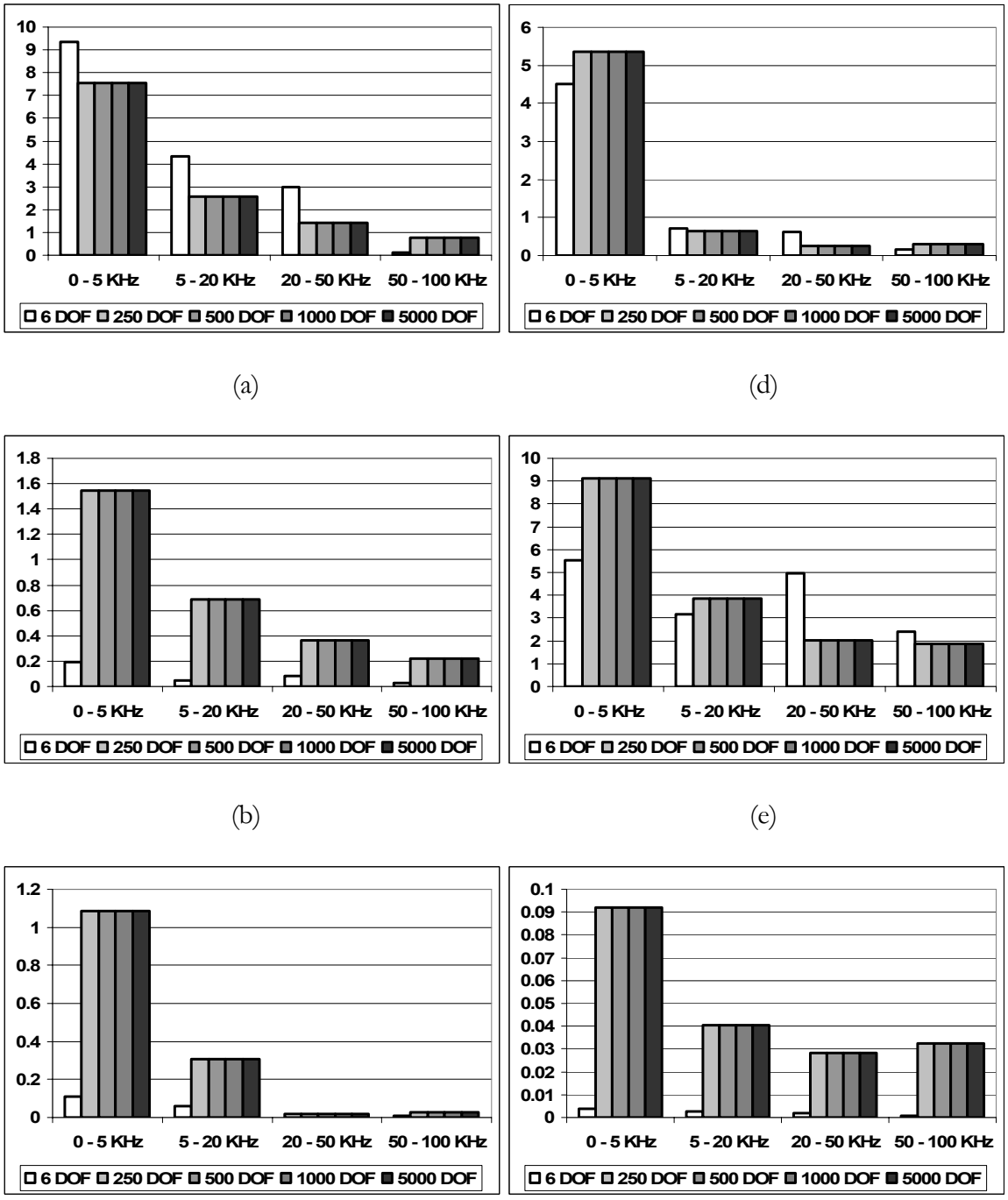

Figure 2.10: Contributions to the RMS in (a) out-of-plane, (b) on-track, (c) off-track, (d) roll, (e) pitch and (f) yaw by different frequency bands for the 6, 250, 500, 1000 and 5000 degrees of freedom reduced models

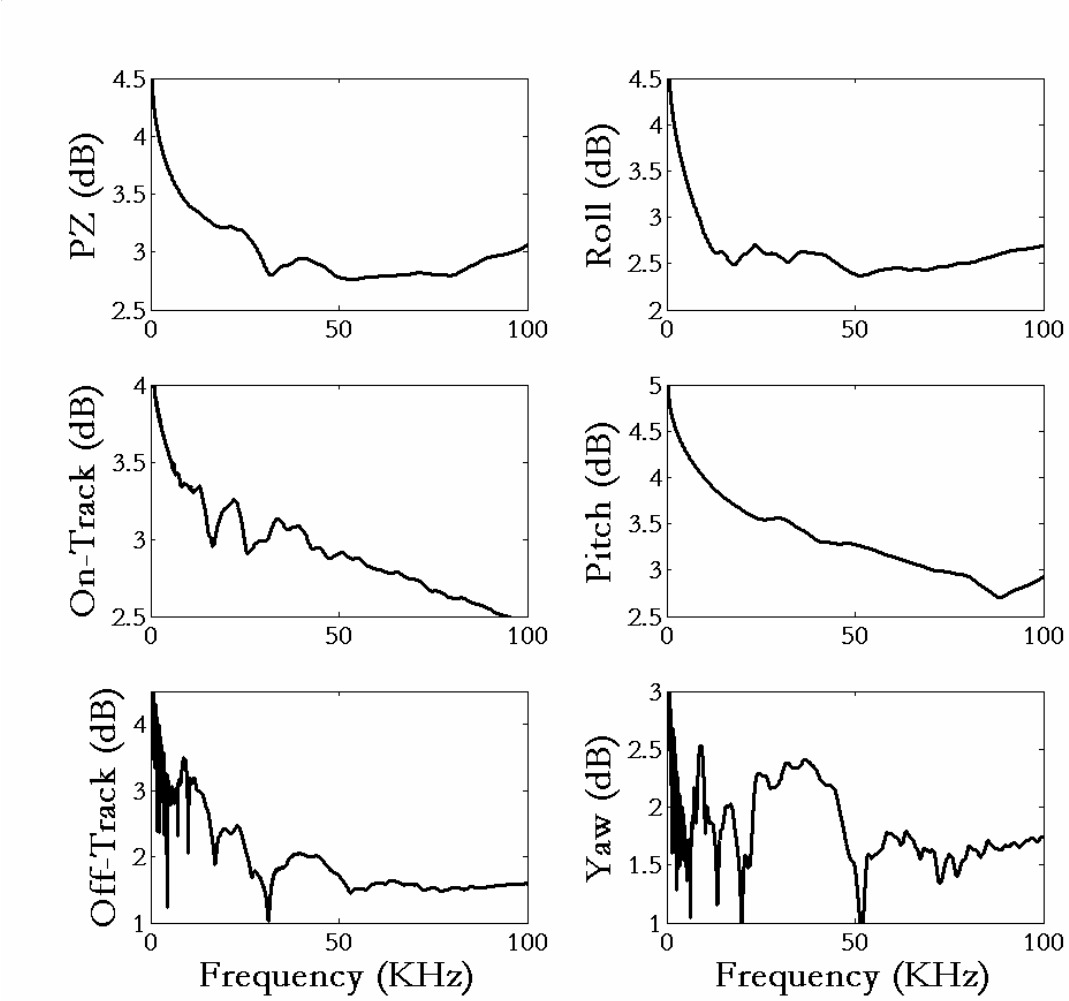

Figure 2.11: Power spectra of the slider displacements in all 6 degrees of freedom for the 250, 500, 1000 and 5000 degrees of freedom reduced model

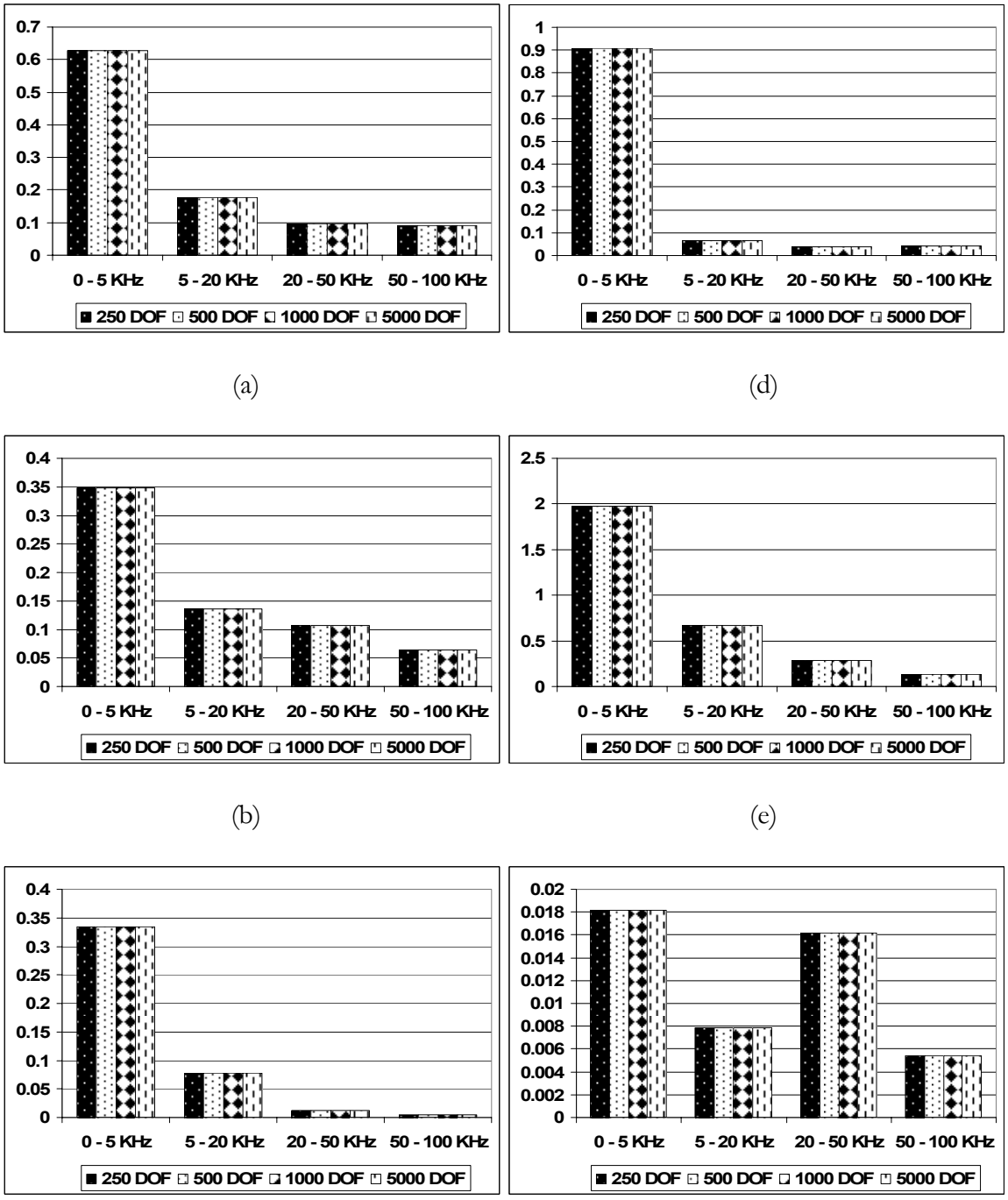

Figure 2.12: Contributions to the RMS in (a) out-of-plane, (b) on-track, (c) off-track, (d) roll, (e) pitch and (f) yaw by different frequency bands for the 250, 500, 1000 and 5000 degrees of freedom reduced models

CHAPTER 3

SLIDER DYNAMICS AND STABILITY IN THE PRESENCE OF THE INTERMOLECULAR AND THE ELECTROSTATIC FORCES ON A PERFECTLY SMOOTH HEAD-DISK INTERFACE

3.1 Introduction

As the flying height between the slider and the disk reduces to less than 5 nm, physical phenomena such as intermolecular and electrostatic forces, which show inverse relationship with head media spacing, become very significant. These forces are attractive in nature and cause the total stiffness between the slider and the disk to become negative, thus resulting in HDI failure [34],[35],[36]. In this chapter we investigate the effect of intermolecular and electrostatic forces on the slider's flying characteristics along all 6 degrees of freedom – 3 translational and 3 rotational.

3.2 Intermolecular Force Model

Intermolecular forces act between all atoms and molecules, even if they are neutral. These universal attractive forces acting between all atoms, molecules, ions, etc. have been explained on the basis of wave mechanics [6]. If the two molecules carry dipole moments they mutually influence their spatial orientations in such a way that, on average, there is an attractive force. Moreover, each molecule induces a dipole in the other molecule and the attraction is reinforced by this mutual polarization.

There are also strong repulsive forces at very small interatomic distances, which determine how close two atoms or molecules can approach each other. These repulsive forces are due

to an overlap of the electron clouds of atoms. They are short range forces and increase sharply as the two molecules come together.

The total pair potential is obtained by summing the attractive and the repulsive potentials. The Lennard-Jones or '6-12' potential is used in this study to model the total pair potential due to the attractive and the repulsive forces [6]. This model is described below.

In order to calculate the van der Waals interaction energies in vacuum for a pair of bodies with different geometries, the interaction is assumed to be non-retarded and additive. Thus the interatomic van der Waals pair potential is of the form

$$U_{IMF}(z) = -\frac{C}{z^6} + \frac{D}{z^{12}} \tag{3.1}$$

Here C ($=10^{-77}$Jm^6) and D ($=10^{-134}$Jm^{12}) are constants for atoms in vacuum. On integrating the energies of all the atoms in one body with respect to all the atoms in the other we obtain the two body potential per unit area of one surface interacting with an infinite area of another surface, as

$$U_{IMF}(z) = -\frac{\pi C \rho_1 \rho_2}{12 z^2} + \frac{\pi D \rho_1 \rho_2}{360 z^8} \tag{3.2}$$

Here ϱ_1 and ϱ_2 are the number densities of atoms in the disk and the slider, respectively. This equation can be alternatively written as

$$U_{IMF}(z) = -\frac{A}{12\pi z^2} + \frac{B}{360\pi z^8} \tag{3.3}$$

Here A $\left(=\pi^2 C\rho_1\rho_2\right)$ is the Hamaker constants and B $\left(=\pi^2 D\rho_1\rho_2\right)$ is another constant. The effective value of the Hamaker constant (A) is a function of the refractive indices and the dielectric constants of the various interface layers and the thickness of each of these layers. Typical values for the Hamaker constant for the HDI can vary from as low as $0.1*10^{-19}$J to as high as $5*10^{-19}$J. And a typical value of B is about 10^{-76} Jm^6.

The total interaction energy between the slider and the disk, obtained by integrating the above expression over the slider surface, is given by

$$U_{IMF\ Total}(z) = -\frac{A}{12\pi}\iint\limits_{\substack{Rect\\Area}}\frac{dx\,dy}{z^2} + \frac{B}{360\pi}\iint\limits_{\substack{Rect\\Area}}\frac{dx\,dy}{z^8} \tag{3.4}$$

And the intermolecular forces between the slider and the disk can be expressed as

$$F_{IMF}(z) = -\frac{d\left(U_{IMF\ Total}\right)}{dz} = -\frac{A}{6\pi}\iint\limits_{\substack{Rect\\Area}}\frac{dx\,dy}{z^3} + \frac{B}{45\pi}\iint\limits_{\substack{Rect\\Area}}\frac{dx\,dy}{z^9} \tag{3.5}$$

3.3 Electrostatic Force Model

The electrostatic forces are due to the spurious charge buildup at the HDI, which is due to a tribocharging phenomenon. Several researchers have studied the cause of the tribocharging phenomenon at the HDI. Kiely and Hsia [37] proposed that the tribocharging can be due to two factors – wear and surface potential. They developed models for both wear and surface potential induced tribocharging and found that the overall magnitudes of both the current and the voltage are dependent on the rate of disk rotation. Thus they predicted the effect of disk rotation speed on charging. Feng et al. [38] also studied the effects of lubricants, carbon

overcoats and relative humidity on tribocharging at the HDI. They found that the tribocharging increases with the severity of head-disk interactions and decreases with the conductivity of the carbon overcoat on the magnetic disk. Vander Oetelaar et al. [39] also studied the tribocharging phenomena at the HDI. They proposed that the tribocharging can be either due to the chemical modification of the surface by the removal of oxygen bonded to the surface, or due to the charge injection and trapping in electronic states in the gap of the insulating region of the DLC coating. They further suggested that at higher humidity the charge buildup due to chemical modification of the surface decays at a faster rate.

The parallel plate potential model is used in this study to model the electrostatic forces at the HDI [6]. This model is described below.

$$U_{Elec}(z) = -\frac{\varepsilon_o k_e V^2 \, dx \, dy}{2z} \tag{3.6}$$

Here ε_o, k_e and V are the permittivity constant (8.85 x 10^{-12} farad/m), the dielectric constant of the medium (1 for air) and the potential difference between the slider and the disk. Typical values of the potential difference (V) are 0 to 1 volts.

The total interaction energy between the slider and the disk, obtained by integrating the above expression over the slider surface, is given by

$$U_{Elec\,Total}(z) = -\frac{\varepsilon_o k_e V^2}{2} \iint_{\substack{Rect \\ Area}} \frac{dx \, dy}{z} \tag{3.7}$$

And the electrostatic forces between the slider and the disk can be written as

$$F_{IMF}(z) = -\frac{d\left(U_{Elec\,Total}\right)}{dz} = -\frac{\varepsilon_o k_e V^2}{2} \iint\limits_{\substack{Rect \\ Area}} \frac{dx\,dy}{z^2} \tag{3.8}$$

3.4 Air Bearing Slider's Static Response

In order to study the effect of intermolecular and electrostatic forces on the slider's flying characteristics, we carried out numerical simulations for two low flying sliders – one flying at a minimum mechanical spacing of 5 nm (ABS-1) and the other one flying at a minimum mechanical spacing of 3 nm (ABS-2). Figure 3.1 shows the air bearing slider designs of both sliders used in this investigation. The disk RPM is 7200 and the slider radial position is 32 mm in both cases.

As we discussed in the previous sections, the magnitude of the intermolecular force is a function of the Hamaker constant (A) and the magnitude of the electrostatic force is a function of the potential difference between the slider and the disk (V). A typical value of the Hamaker constant with a representative thickness of the DLC layer on the slider and lubricant layer on the disk is $0.89*10^{-19}$J. Similarly typical values of the Hamaker constant for a DLC-DLC interface and a Lubricant-Lubricant interface are $2.7*10^{-19}$J and $0.29*10^{-19}$J, respectively [6]. Thus in this study the numerical simulations are carried for values of A equal to $0.2*10^{-19}$J, $0.5*10^{-19}$J, $1*10^{-19}$J, $2*10^{-19}$J and $5*10^{-19}$J. Similarly, typical value of the potential difference between the slider and the disk are 0 to 1 Volt, so we used values of potential difference equal to 0V, 0.1V, 0.5V, 0.7V and 1.0V.

Table 3.1 and Table 3.2 show the steady state slider displacements without considering the effect of intermolecular and electrostatic forces (i.e. A = 0E-19J and V = 0 Volt) along all 6

degrees of freedom for the air-bearing slider design-1 (ABS-1) and the air-bearing slider design-2 (ABS-2), respectively. We also observe that for ABS-1 the minimum mechanical spacing between the slider and the disk is 5 nm with the pitch and the roll angles of 148.78 μrad and 7.43 μrad, respectively. And for ABS-2 the minimum mechanical spacing between the slider and the disk is 3 nm and the pitch and the roll angles are 122.71 μrad and 3.55 μrad, respectively.

Between the two slider designs we considered, ABS-2 has a smaller overall mechanical spacing as it has smaller minimum flying height and smaller pitch and roll angles compared to ABS-1. Thus for the same values of the Hamaker constant and potential difference between the slider and the disk ABS-2 must be effected more by these forces.

Numerical simulations are carried out for both slider designs at several values of the Hamaker constant and potential difference. Figure 3.2 shows bar graphs of the total attractive force (i.e. intermolecular force + electrostatic force) acting on the sliders at the HDI for various values of the Hamaker constant and potential difference for ABS-1 and ABS-2. As mentioned above, we observe that the magnitude of total attractive force is much higher for ABS-2 compared to ABS-1.

Figure 3.3 and Figure 3.4 show the bar graph of the steady state values of the slider's displacements for ABS-1 and ABS-2, respectively, along all 6 degrees of freedom. For both slider designs we observe that as the magnitude of the intermolecular forces increase, i.e. as the value of the Hamaker constant (A) increases, the minimum flying height between the slider and the disk decreases. Similarly, as the magnitude of the electrostatic force increases,

i.e. as the values of potential difference (V) increases, the minimum flying height between the slider and the disk decreases. The drop in the flying height is as much as 0.84 nm and 0.93 nm at very high magnitudes of attractive force. At a reasonable HDI value of A = $1*10^{-19}$J and V = 0.3 volt, the drop in the flying height is around 0.19 nm (3.8%) and 0.30 nm (10%) for ABS-1 and ABS-2, respectively. This shows a significant reduction in mechanical spacing between the slider and the disk in the presence of intermolecular and electrostatic forces, and the effect is higher for the lower flying slider.

The change in the steady state values of the off-track and the on-track displacements are relatively small even when the magnitudes of the intermolecular or the electrostatic force have the larger values. The maximum change in the off-track displacement is 0.017 nm for ABS-1 and 0.402 nm for ABS-2, which is quite small compared to the current track width of 200 nm. The maximum change in the on-track displacements is 0.280 nm for ABS-1 and 0.284 nm for ABS-2. But at the reasonable HDI values of A = $1*10^{-19}$J and V = 0.3 volt, the change in the off-track displacement is 0.001 nm and 0.040 nm for ABS-1 and ABS-2, respectively, and the change in the on-track displacement is 0.059 nm and 0.097 nm for ABS-1 and ABS-2, respectively. This shows that the effects of intermolecular and electrostatic forces are relatively small on slider off-track and on-track displacements.

From Figure 3.3 and Figure 3.4 we also observe that the change in the steady state values of the pitch, roll and yaw angles are relatively small even when the magnitudes of the intermolecular or the electrostatic force have larger values. The pitch angle slightly increases as the magnitude of the attractive forces increases. The maximum increase in the value of the pitch angle is 1.61 μrad and 1.82 μrad for ABS-1 and ABS-2, respectively, which is quite

small compared to the pitch angles of 148.74 μrad and 122.71 μrad for the two cases, respectively. Similarly, the maximum change in the value of the roll angle is 0.3983 μrad and 0.6843 μrad for ABS-1 and ABS-2, respectively and the maximum change in the value of the yaw angle is 0.00507 μrad and 0.00798 μrad, respectively. But again at the reasonable HDI values of $A = 1*10^{-19}$J and V = 0.3 volt, the change in the pitch angle is 0.34 μrad and 0.59 μrad, the change in the roll angle is 0.0754 μrad and 0.1317 μrad, and the change in the yaw angle is 0.00092 μrad and 0.00205 μrad for ABS-1 and ABS-2, respectively. This shows that the effects of intermolecular and electrostatic forces are relatively small for slider pitch, roll and yaw rotations.

It should be noted that in this study we assumed no slider disk contact. Bur if the reduced flying height caused by the intermolecular and electrostatic forces brings the sliders into contact with the disk then the results will be quite different, especially along the off-track direction.

3.5 Stability Criteria for the Head-Disk Interface

In order to have a stable HDI, the real part of all the eigenvalues of the linearized system should be negative. If even one eigenvalue of the linearized system has positive real part then the system will be unstable.

In this study the stability/instability of the HDI is analyzed using a "flying height diagram". The flying height diagram plots the slider flying height versus disk RPM. The minimum mechanical spacing between the slider and the disk is referred to as the flying height. A typical flying height diagram is shown in Figure 3.5. The points on curve 1 give the steady

state flying height as a function of disk RPM without considering the effects of intermolecular and electrostatic forces. All of the points on this curve have all eigenvalues with negative real part and hence represent stable conditions. Curves 2 and 3 plot the flying height versus disk RPM, taking into consideration the effect of intermolecular and electrostatic forces. From this figure we observe multiple equilibrium points for disk RPM between 1900 and 4300. The equilibrium points on curve 2 have all eigenvalues with negative real part and hence are stable equilibrium points. However the points on curve 3 have at least one eigenvalues with positive real part and hence are unstable equilibrium points.

From the flying height diagram we observe that as the disk RPM decreases from 12000 to as low as 1900, a stable flying height is given by the curve 2. Below 1900 RPM (corresponding to a flying height of 3.4 nm) the slider becomes unstable and contact occurs between the slider and the disk. This value of disk RPM gives the touchdown RPM. If the disk RPM is increased from 1900, the slider remains unstable until a disk RPM of 4300. For RPM above 4300 (corresponding to a flying height of 5.05 nm) there is only one equilibrium point, which is stable and hence the stability of the HDI is restored at 4300. This value of RPM gives the takeoff RPM. The stable flying height for the system is 5.05 nm above which the system will always converge to a stable equilibrium if it is perturbed about its steady state due to external disturbances such as air flow, disk roughness etc. We call this fly height the "desired fly height". The RPM range of curve 3 in the flying height diagram gives an estimate of the hysterisis observed in touchdown-takeoff experiments. We can also conclude that the larger the range of the unstable region (curve 3), the higher will be the hysterisis observed in the touchdown-takeoff experiments.

3.6 Air Bearing Slider's Stability at the Head-Disk Interface

Simulations are carried out for the slider design shown in Figure 3.6 for potential differences of V = 0.3 volts and V= 1.0 volts, with and without intermolecular forces. The flying height diagrams are shown in Figure 3.7. The equilibrium points for which the head media spacing is less than 0.3 nm are considered to be contact and are not included in this flying height diagram.

We found that the hysteretic behavior depends on the potential difference between the slider and the disk, which characterizes the strength of the interaction. The potential difference between the slider and the disk increases the width of the unstable region regardless of whether the intermolecular forces are present. On comparing the flying height diagrams for the cases with V = 0.0 volts and V = 0.3 volts, we observe that a potential difference of 0.3 volts does not have a significant effect for flying heights greater than 4 nm. But on the other hand a potential difference of 1 volt has a very significant effect even at higher flying heights.

To validate our simulation results we carried out static simulations for the slider design shown in Figure 3.6 with intermolecular forces and various values of potential difference between the slider and the disk. A suitable disk rpm is chosen at which the slider's flying height is 30 nm with V = 0 volts. The potential difference is then increased between the slider and the disk until the air bearing is unable to maintain the spacing between the slider and the disk, i.e. the stiffness becomes negative and contact occurs as shown in Figure 3.8.

These results are compared with similar experimental results recently published by Song et

al. [40]. Excellent agreement is seen between the simulation results and the experimental data. Similar simulations are also carried out for two other 30 nm flying height slider designs. We found that the simulation results are not exactly the same as shown in Figure 3.8, but the differences are not much.

Static simulations are also carried out at suitable disk rpm's such that the slider design shown in Figure 3.6 has flying height's of 15nm, 10nm and 5nm for V = 0 volts. The breakdown voltages are then calculated for these three cases. Figure 3.9 shows the increase in breakdown voltage as the slider flying height increases. As expected for high flying sliders the air bearing can withstand higher voltage across it before it breaks down.

But, on the other hand, as the potential difference between the slider and the disk increases the air bearing breaks down at higher flying heights. For example, for a 30 nm flying slider, when the potential difference between the slider and the disk increases the flying height decreases and the air bearing finally breaks down at a spacing of 9.45 nm when the potential difference is 7.13 volts, and for a 15 nm flying slider the air bearing breaks down at 4.65 nm when the potential difference between the slider and the disk in 3.96 volts.

Further, static simulations are carried out for the two different slider designs shown in Figure 3.6 and Figure 3.10. Suitable disk rpm's are chosen for both slider designs so that they fly at 5 nm. The slider design shown in Figure 3.6 is a higher pitch slider with a pitch angle close to 245 μrad and the slider design shown in Figure 3.10 is a lower pitch slider with a pitch angle close to 190 μrad.

The potential difference is then increased between the slider and the disk in the simulations until the air bearing is unable to maintain the spacing between the slider and the disk, i.e. the stiffness becomes negative and contact occurs as shown in Figure 3.11. We observe that the high pitch slider air bearing can sustain higher voltage across it before it breaks down. It is also observed that as the potential difference between the slider and the disk increases the magnitude of the pitch angle also increases slightly.

The dynamic response is also simulated at a disk rpm of 7200 for the slider design shown in Figure 3.6. The slider is "dropped" from a 10 nm flying height. We observe that the solver converges to a steady state when the potential difference between the slider and the disk is 0.3 volts and 1.0 volts as shown in the Figure 3.12. But for higher potential differences the system becomes unstable and contact occurs between the slider and the disk. From the flying height diagram shown in Figure 3.7 we observe that at the disk rpm of 7200 there exists only one (stable) equilibrium point when the potential difference between the slider and the disk is 0, 0.3 and 1.0 volts. Hence the system always converges to a steady state for small perturbations about the equilibrium point as shown in Figure 3.12.

3.7 Conclusions

In this chapter we studied the effect of intermolecular and electrostatic forces on slider displacements in all 6 degrees of freedom. We found that the magnitude of these forces increase as the mechanical spacing between the slider and the disk decreases, which may result in a significant drop in the mechanical spacing at the HDI. This reduction in the spacing can be as high as 10% or more of the mechanical spacing between the slider and the disk for reasonable values of Hamaker constant (A) and potential difference (V). But the

change in the other 5 degrees of freedom, i.e. the off-track and the on-track displacement and the pitch, roll and yaw angle is relatively small, assuming the reduced flying height does not lead to more slider disk contact.

A theoretical investigation of the stability and dynamics of air bearing sliders at the HDI is presented. A fly height diagram is used to analyze the stability of the HDI. It is observed that high flying sliders can withstand higher potential difference between the slider and the disk before the air bearing breaks down. We also found that high pitch sliders are more stable in the presence of intermolecular and electrostatic forces. Further, the simulation results are compared with previously published experiments giving strong validation of the HDD model.

3.8 Tables

Table 3.1: Steady state values of slider displacements for ABS-1

Min Flying Height (nm)	5.0166
On-Track Displacement (nm)	24.36
Off-Track Displacement (nm)	10.66
Roll (μrad)	7.4349
Pitch (μrad)	148.74
Yaw (μrad)	0.2659

Table 3.2: Steady state values of slider displacements for ABS-2

Min Flying Height (nm)	2.9919
On-Track Displacement (nm)	11.462
Off-Track Displacement (nm)	23.405
Roll (μrad)	3.5528
Pitch (μrad)	122.71
Yaw (μrad)	0.5948

3.9 Figures

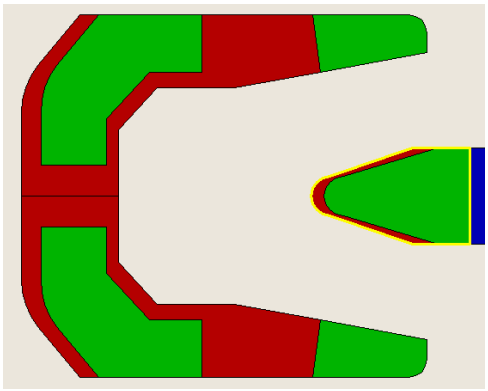

(a)

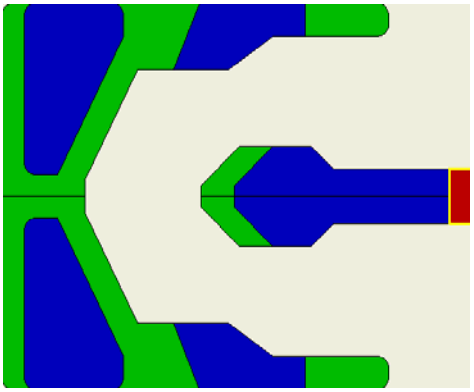

(b)

Figure 3.1: Femto slider designs (a) ABS-1 with a minimum flying height of 5 nm w/o intermolecular and electrostatic force (b) ABS-2 with a minimum flying height of 3 nm w/o intermolecular and electrostatic force.

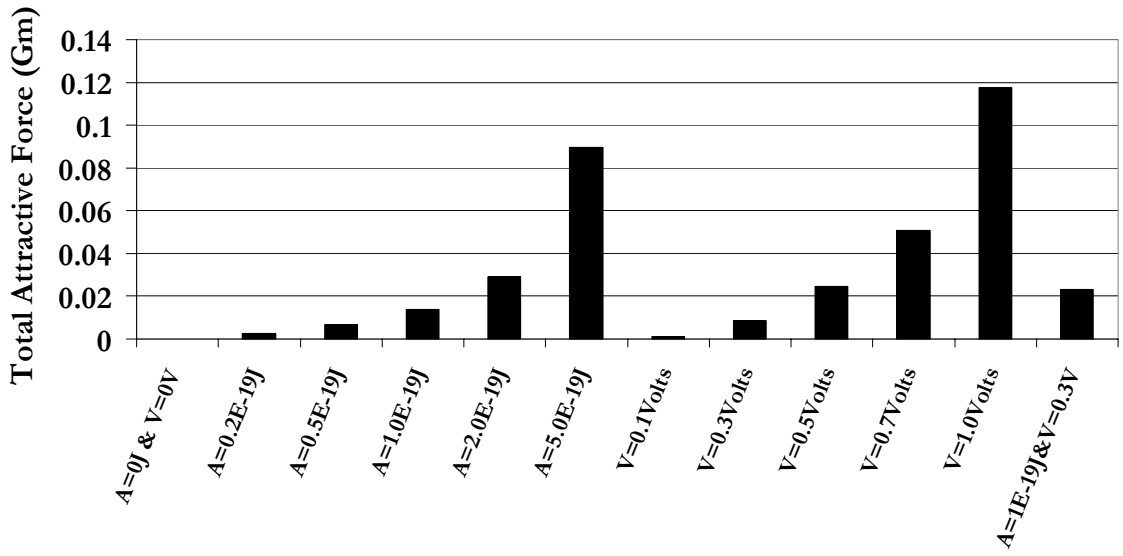

(a)

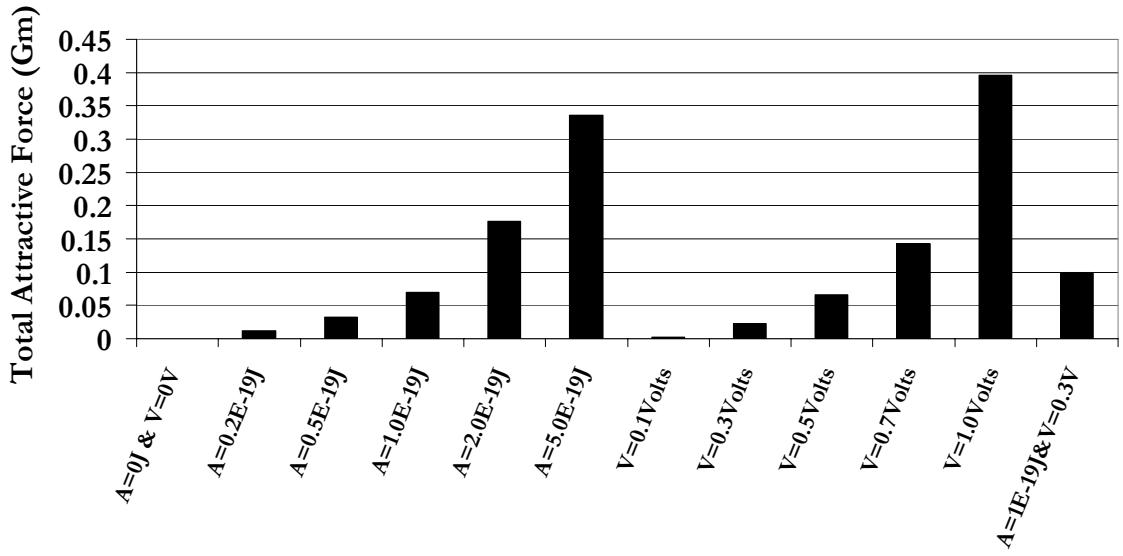

(b)

Figure 3.2: Total attractive force for (a) ABS-1 and (b) ABS-2

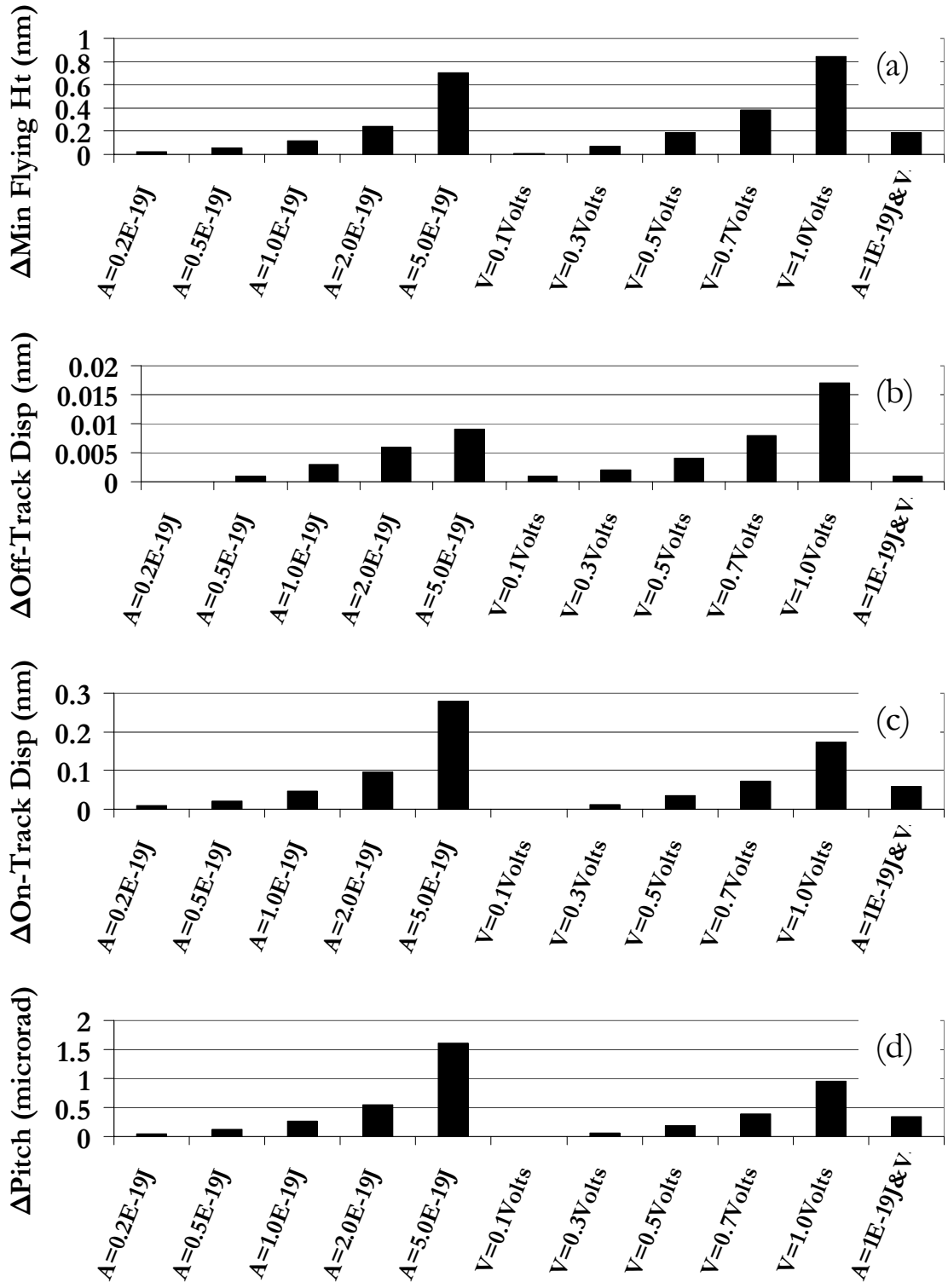
ΔMin Flying Ht (nm)
1
0.8
0.6
0.4
0.2
0
(a)
A=0.2E-19J
A=0.5E-19J
A=1.0E-19J
A=2.0E-19J
A=5.0E-19J
V=0.1Volts
V=0.3Volts
V=0.5Volts
V=0.7Volts
V=1.0Volts
A=1E-19J&V
ΔOff-Track Disp (nm)
0.02
0.015
0.01
0.005
0
(b)
A=0.2E-19J
A=0.5E-19J
A=1.0E-19J
A=2.0E-19J
A=5.0E-19J
V=0.1Volts
V=0.3Volts
V=0.5Volts
V=0.7Volts
V=1.0Volts
A=1E-19J&V
ΔOn-Track Disp (nm)
0.3
0.2
0.1
0
(c)
A=0.2E-19J
A=0.5E-19J
A=1.0E-19J
A=2.0E-19J
A=5.0E-19J
V=0.1Volts
V=0.3Volts
V=0.5Volts
V=0.7Volts
V=1.0Volts
A=1E-19J&V
ΔPitch (microrad)
2
1.5
1
0.5
0
(d)
A=0.2E-19J
A=0.5E-19J
A=1.0E-19J
A=2.0E-19J
A=5.0E-19J
V=0.1Volts
V=0.3Volts
V=0.5Volts
V=0.7Volts
V=1.0Volts
A=1E-19J&V

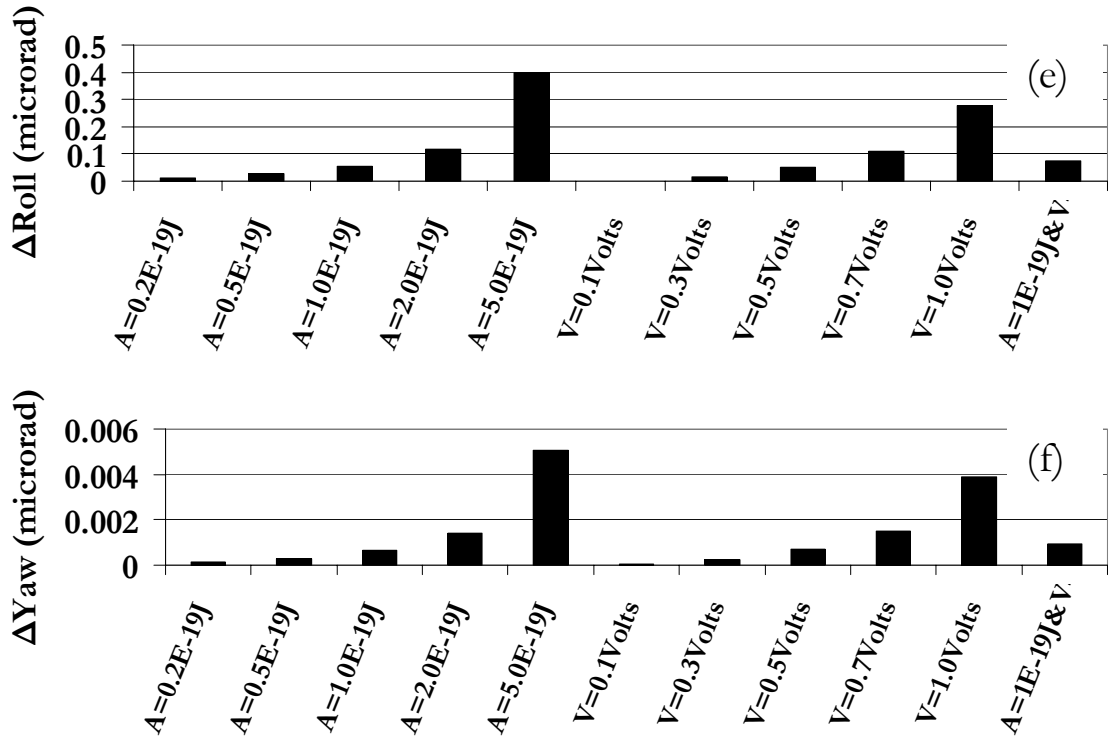

Figure 3.3: Steady state values for ABS-1 along (a) vertical, (b) off-track, (c) on-track, (d) pitch, (e) roll and (f) yaw directions for various values of Hamaker constant and potential difference between the slider and the disk

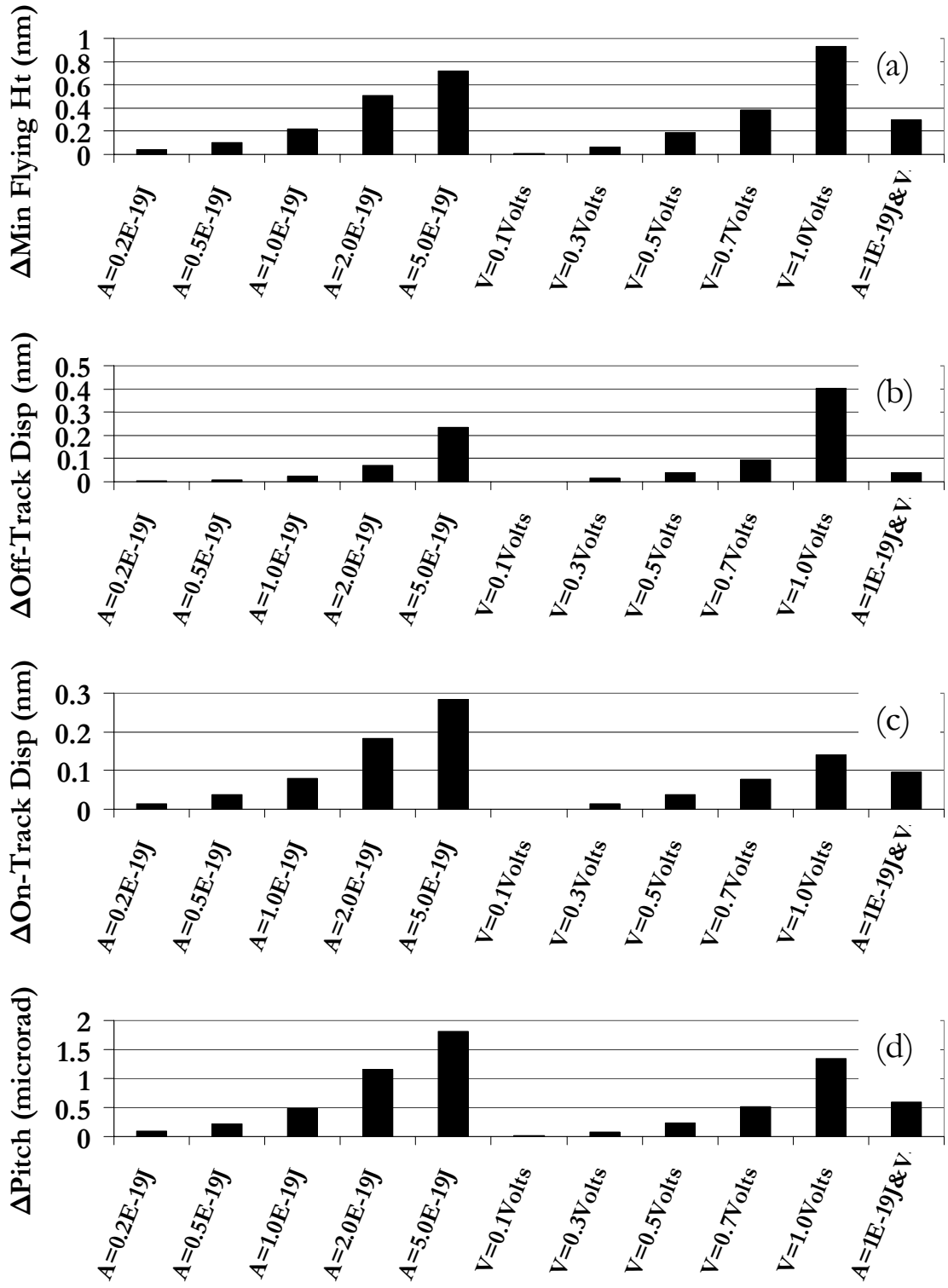
ΔMin Flying Ht (nm)
1
0.8
0.6
0.4
0.2
0
(a)
A=0.2E-19J
A=0.5E-19J
A=1.0E-19J
A=2.0E-19J
A=5.0E-19J
V=0.1Volts
V=0.3Volts
V=0.5Volts
V=0.7Volts
V=1.0Volts
A=1E-19J&V
ΔOff-Track Disp (nm)
0.5
0.4
0.3
0.2
0.1
0
(b)
A=0.2E-19J
A=0.5E-19J
A=1.0E-19J
A=2.0E-19J
A=5.0E-19J
V=0.1Volts
V=0.3Volts
V=0.5Volts
V=0.7Volts
V=1.0Volts
A=1E-19J&V
ΔOn-Track Disp (nm)
0.3
0.2
0.1
0
(c)
A=0.2E-19J
A=0.5E-19J
A=1.0E-19J
A=2.0E-19J
A=5.0E-19J
V=0.1Volts
V=0.3Volts
V=0.5Volts
V=0.7Volts
V=1.0Volts
A=1E-19J&V
ΔPitch (microrad)
2
1.5
1
0.5
0
(d)
A=0.2E-19J
A=0.5E-19J
A=1.0E-19J
A=2.0E-19J
A=5.0E-19J
V=0.1Volts
V=0.3Volts
V=0.5Volts
V=0.7Volts
V=1.0Volts
A=1E-19J&V

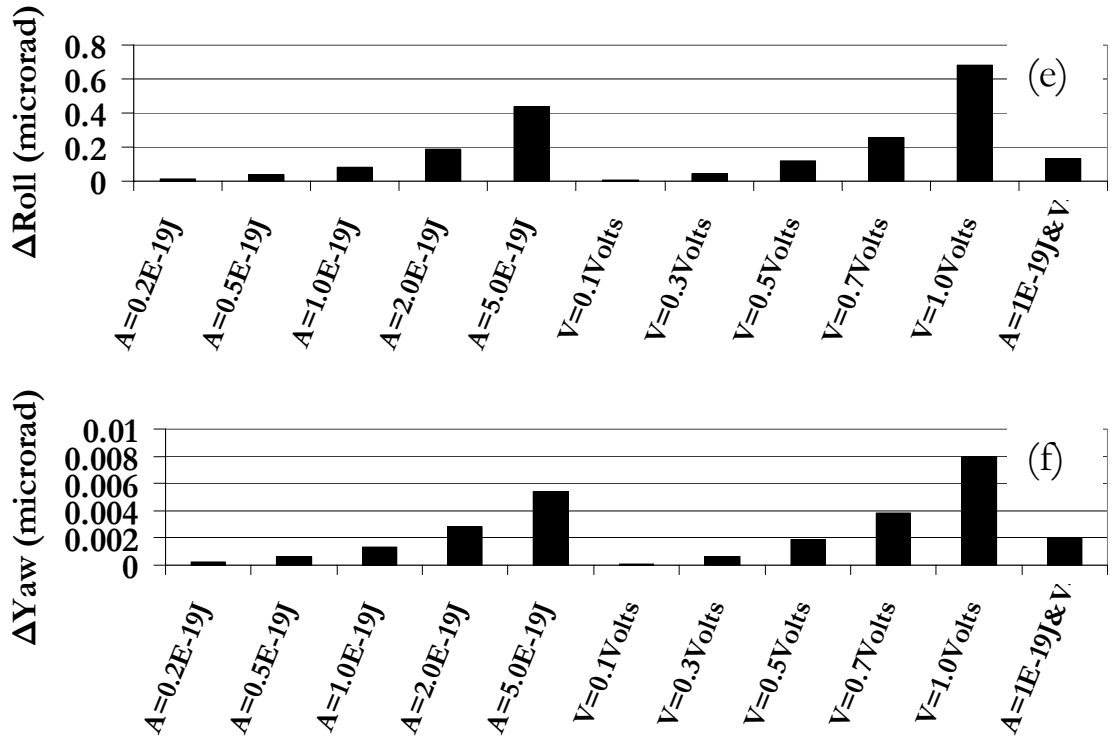

Figure 3.4: Steady state values for ABS-2 along (a) vertical, (b) off-track, (c) on-track, (d) pitch, (e) roll and (f) yaw directions for various values of Hamaker constant and potential difference between the slider and the disk

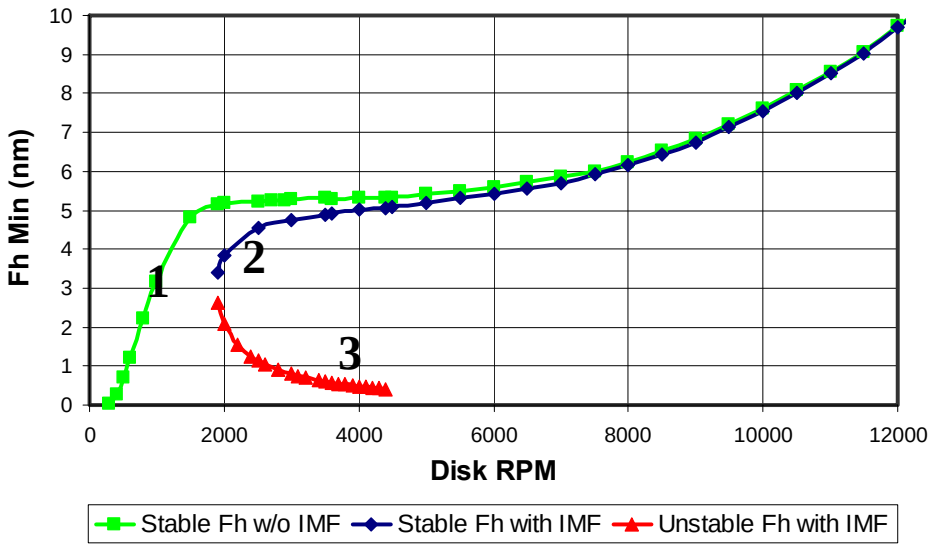

Figure 3.5: The flying height diagram

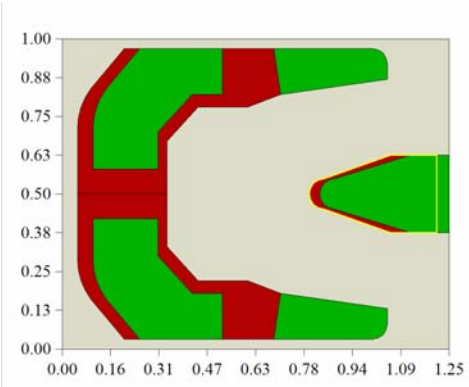

Figure 3.6: High pitch pico slider with crown of 30 nm and a camber of -5 nm. The base recess is 1.397 µm.

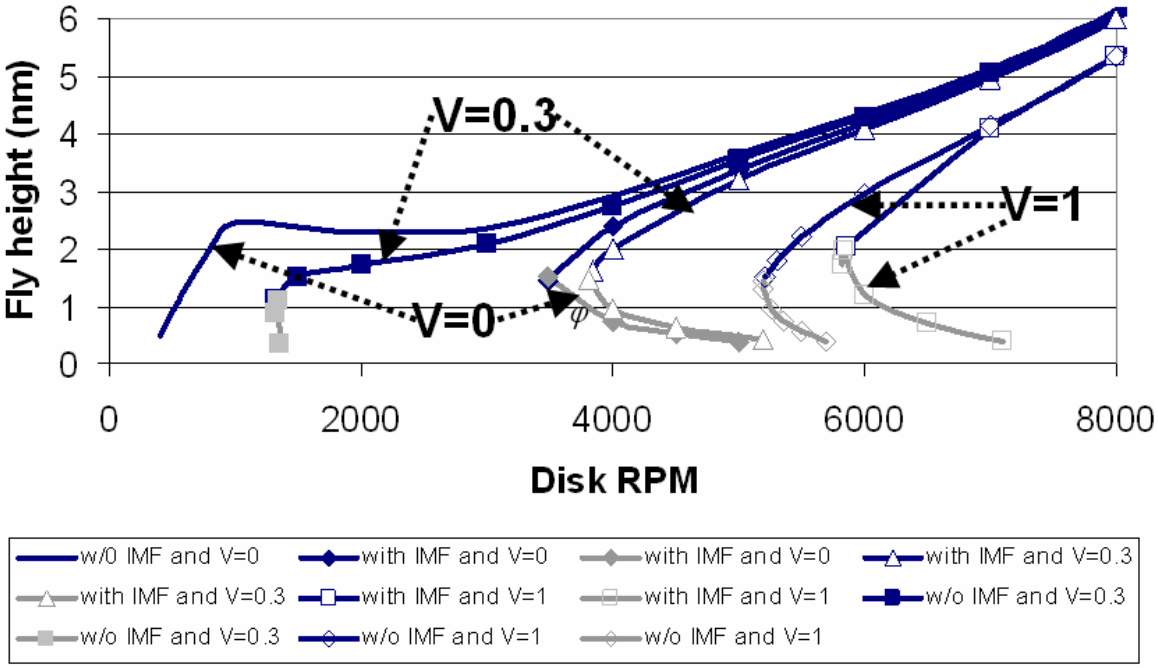

Figure 3.7: Flying height diagram using HDI model for slider design shown in Figure 3.6

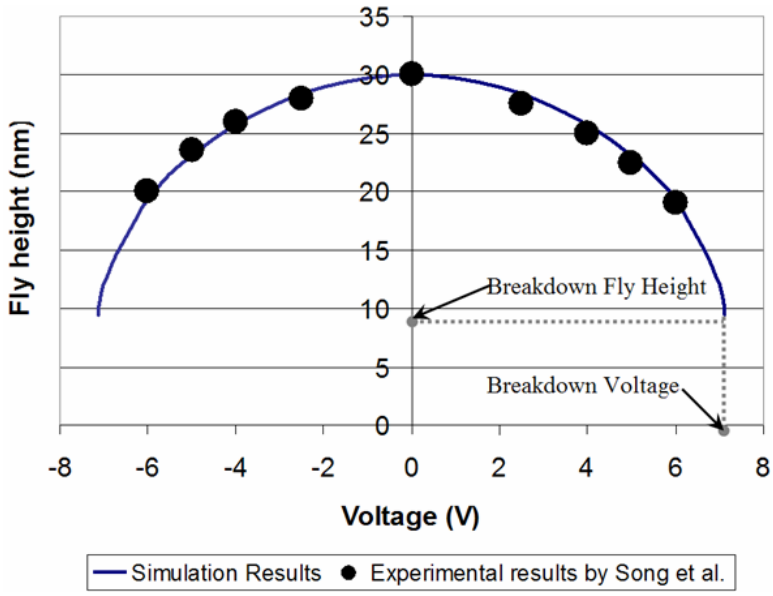

Figure 3.8: Fly height variation as a function of potential difference.

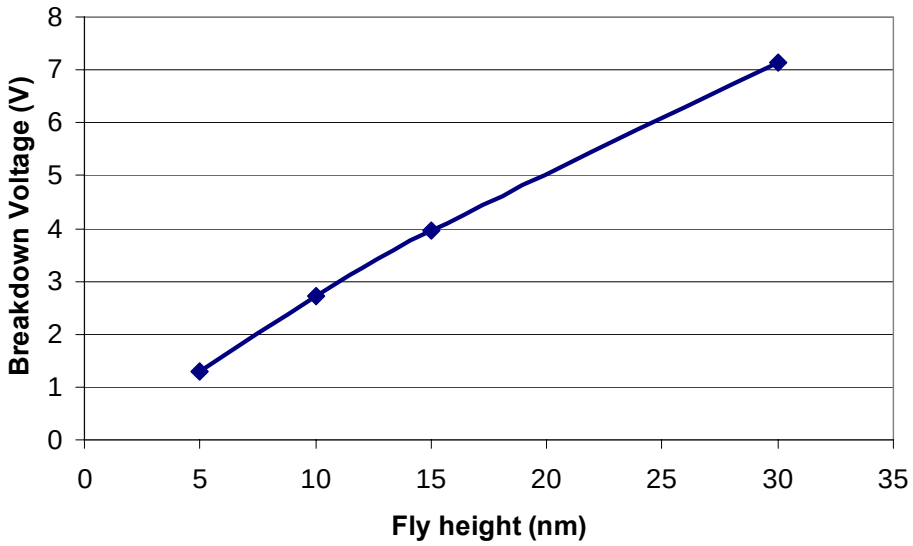

Figure 3.9: Increase in breakdown potential as the slider fly height increases.

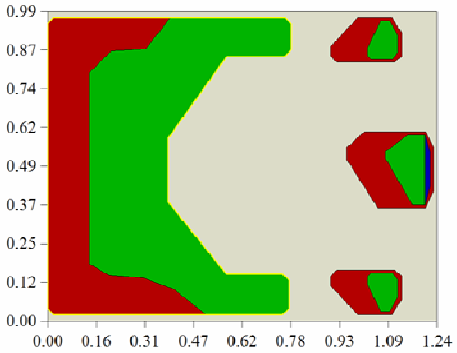

Figure 3.10: Low pitch pico slider with crown of 30 nm and a camber of -5 nm. The base recess is 1.397 μm.

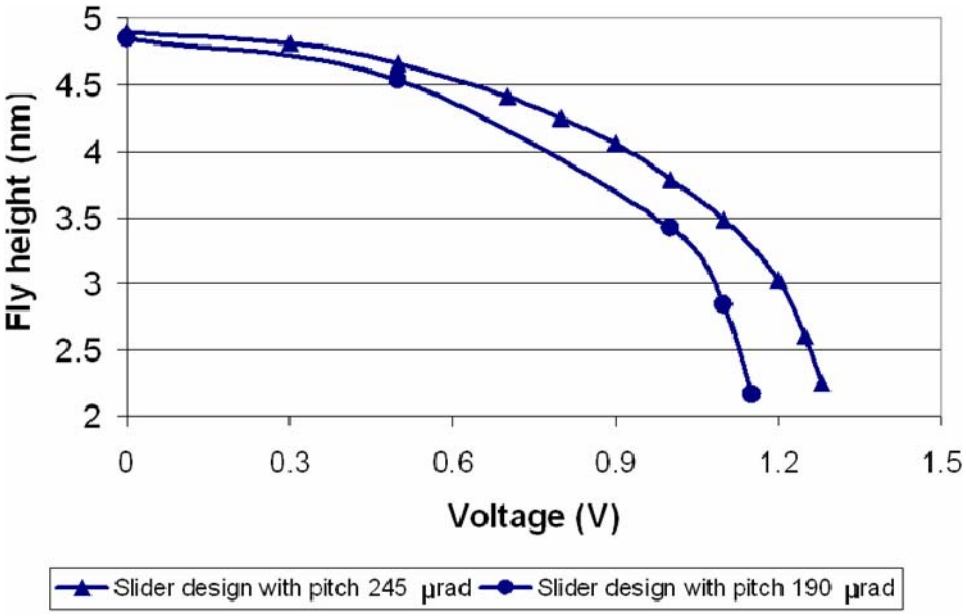

Figure 3.11: Fly height variation as a function of potential difference.

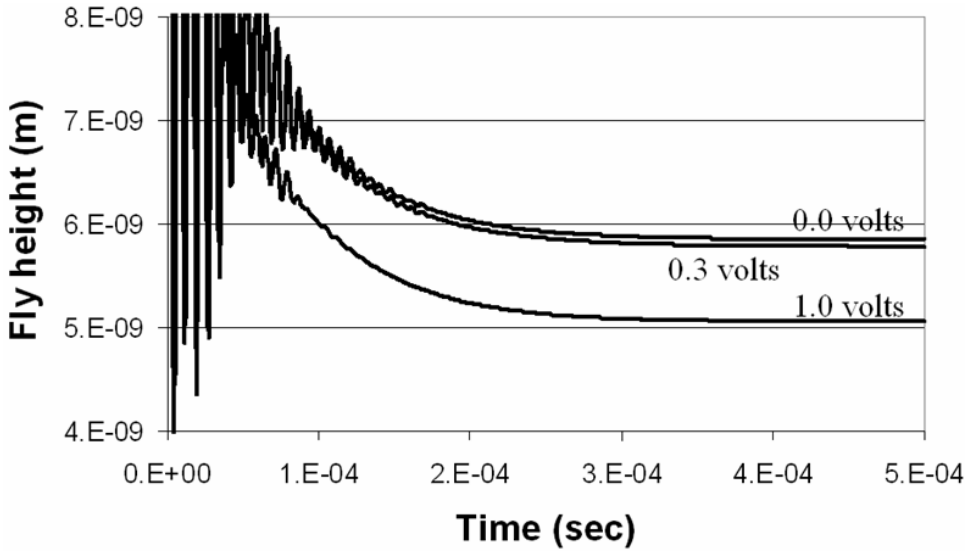

Figure 3.12: Dynamic response of the slider in Figure 3.6 at a disk rpm of 7200 as the potential difference increases between the slider and the disk.

CHAPTER 4

THE EFFECT OF SLIDER-DISK SURFACE TOPOGRAPHY ON SLIDER VIBRATIONS AND STABILITY AT THE HEAD-DISK INTERFACE

4.1 Introduction

In the last chapter the effect of the intermolecular and the electrostatic forces is investigated without considering the effect of slider-disk surface topography. We observe that these forces cause a significant reduction in the mechanical spacing between the slider and the disk at the HDI. Thus at such small mechanical spacing of less than 5 nm, the slider-disk topographies will significantly affect the vibrations and stability of the slider at the HDI. On one hand the waviness (macro, micro and nano) will excite the structural modes of the HSA increasing the TMR and the FHM. And on the other hand the roughness will affect the magnitude of the adhesion forces and hence the stability of the slider at the HDI. Thus the effect of slider-disk topography on slider dynamics is investigated in this chapter. Optimal slider-disk topography has been proposed not only to reduce the slider vibrations but also to increase the HDI stability.

4.2 The Adhesion and the Contact Force Model

When the slider is flying at a mechanical spacing of less than 5 nm from the disk surface the magnitude of the adhesion and contact forces becomes significant. The total adhesion force between the slider and the disk can be divided into two parts: the adhesion force due to non-contacting asperities and the adhesion force due to non-contacting part of the contacting asperities [41],[42],[43]. This can be expressed as:

$$F_A = \frac{8\pi}{3} R\Delta\gamma\eta A\varepsilon^{*2}\left\{\int_{-\infty}^{h^*-y_s^*}\left[\frac{1}{(\varepsilon^*-\omega^*)^2}-\frac{\varepsilon^{*6}}{(\varepsilon^*-\omega^*)^8}\right]\phi^*(u^*)du^* + 2\int_{h^*-y_s^*}^{\infty}\int_{-\infty}^{h^*-y_s^*}\left[\frac{1}{Z^{*3}}-\frac{\varepsilon^{*6}}{Z^{*9}}\right]\phi^*(u^*)s^*ds^*du^*\right\} \quad (4.1)$$

Here $\Delta\gamma$, R, η, A, and u are the change in surface energy, radius of curvature of asperities, asperity density, nominal contact area and height of asperity from the mean of asperity heights. The variables h, y_s, ω and ε are the separation between the surfaces, difference between the mean of the asperity height and the surface height, the interference and the intermolecular distance, and the $(^*)$ denotes the normalized length units by standard deviation of surface heights. In the above expression $\phi^*(u^*)$ is the normalized distribution function of the asperity heights and Z^* is the dimensionless separation of the contacting asperity with a flat surface outside the contacting region. A detailed derivation of this formula has been summarized in [41].

Similarly, the total contact force between the slider and the disk can be divided into two parts: the contact force due to elastic deformation of asperities and the contact force due to plastic deformation of asperities [41],[44]. This can be expressed as:

$$F_C = R\eta A\sigma\left\{\frac{4}{3}\left(\frac{\sigma}{R}\right)^{\frac{1}{2}} E\int_{h^*-y_s^*}^{h^*-y_s^*+\omega_c^*}(\omega^*)^{3/2}\phi^*(u^*)du^* + \pi KH\int_{h^*-y_s^*+\omega_c^*}^{\infty}(2\omega^*-\omega_c^*)\phi^*(u^*)du^*\right\} \quad (4.2)$$

Here E, K, H and ω_c are the elastic modulus, the hardness coefficient, the hardness of the softer material and the critical interference at which the plastic deformation starts. A detailed derivation of this formula has also been summarized in [41]. The values of the various HDI parameters used in this investigation have been listed in Table 4.1.

4.3 The Effect of Slider-Disk Topographies

The air bearing slider and the suspension used in this investigation are shown in Figure 4.1

and Figure 4.2, respectively. In order to investigate the effect of slider and disk surface topographies we divided the surface features into three different categories:

(a) Roughness – Surface features with wavelengths up to a few μm.

(b) Waviness – Surface features with wavelength of the order of a few μm to a few mm.

(c) Large wavelength features like disk run-out – Surface features with wavelengths greater than a few mm's.

The roughness and the waviness wavelength domains are further sub-divided into smaller wavelength regimes as shown in Figure 4.3. Different wavelength regimes are investigated separately to gain a better understanding of their effect on the slider vibrations and stability. In order to study the effect of roughness we have used a statistical approach. In this approach the heights of the asperities are assumed to be randomly distributed with a Gaussian density function. The parameters of this Gaussian density function are based on the experimental slider and disk surface measurements. The effect of waviness on slider dynamics is evaluated using an experimentally measured disk profile. These measurements of the disk profile are done using an LDV. And finally the effect of large wavelength disk features is evaluated by studying the effect of various circumferential disk modes on the slider dynamics.

4.4 The Effect of Roughness

In order to study the adhesion and contact forces between two rough surfaces, researchers often consider a smooth surface and a rough surface with equivalent surface roughness parameters [41],[42]. The validity of this assumption has been investigated by several researchers in the past. This assumption simplifies the analysis considerably and thus we also follow the same approach in our investigation. The measured radius of curvature (R) and

standard deviation of asperity heights (σ) values of the combined slider-disk surface are listed in Table 4.2 for several rough (old) and smooth (recent) slider-disk samples. The asperity density is assumed to be 10 $(\mu m)^{-2}$.

We observe that for rough surfaces the σ is large (2-5 nm) and the R is small (1-5 μm), where as for smooth surfaces the σ is small (0.25-1 nm) and the R is large (5- 10 μm). In order to investigate the effect of surface roughness on slider vibrations and HDI stability, simulations are carried out for several combinations of R and σ, where R is varied from 0.5 μm to 25 μm and σ is varied from 0.1 nm to 10 nm. Five cases as listed in Table 4.3 corresponding to different values of disk velocities at the slider location are investigated in this study. The slider's skew is same in all the cases. In this investigation the domain $R \in \{1\mu m - 5\mu m\}$, $\sigma \in \{2nm - 5nm\}$ is defined as a rough surface and the domain $R \in \{5\mu m - 10\mu m\}$, $\sigma \in \{0.25nm - 1nm\}$ is defined as a smooth surface.

Figure 4.4 and Figure 4.5 shows the plots of the magnitude of contact and adhesion force, respectively, for several values of R and σ. The grey regions are the regions where the stiffness becomes negative resulting in slider-disk crash and consequent HDI failure. From Figure 4.4 (a), (b) and (c) we observe that the magnitude of the adhesion force is similar or slightly higher for a rough surface than a smooth surface. Whereas from Figure 4.4 (d) and (e) we observe that the magnitude of the adhesion force is higher for a smooth surface than a rough surface. Similarly from Figure 4.5 (a), (b), (c) and (d) we observe that the magnitude of the contact force is higher for a rough surface than a smooth surface. Whereas from Figure 4.5 (e) we observe that the magnitude of the contact force is higher for smooth surface than for rough surfaces.

In order to understand these results there is a need to study the mechanical spacing between the slider and the disk for the five cases. Figure 4.6 shows the plots of the minimum mechanical spacing between the slider and the disk, slider pitch and slider roll angles as a function of R and σ for cases 1 and 5. We observe that the minimum mechanical spacing between the slider and the disk is much smaller for smooth surfaces in case 5 compared to case 1. Even for some part of the rough domain the minimum mechanical spacing between the slider and the disk is smaller for smooth surfaces in case 5 compared to case 1. We also observe that the pitch and roll angles are much smaller for case 5 as compared to case 1 for both smooth as well as rough surfaces. This suggests that the overall mechanical spacing between the slider and the disk is smaller for case 5 compared to case 1 for both rough and smooth surfaces. This is represented more clearly in Figure 4.7.

From Figure 4.7 we observe that for case 5 the contact area is large for both rough and smooth surfaces. This is the reason contact force is high for both the rough and smooth surfaces in case 5. But for case 1 the contact area is large only for the rough surface whereas for the smooth surface the contact area is negligible. This is the reason the contact force is large for the rough surface and almost negligible for the smooth surface. From Figure 4.7 we also observe that for case 5 the area of the top surface in close proximity (but not in contact) with the flat surface is higher for the smooth surface than the rough surface. And since adhesion forces are directly proportional to the area of one surface in close proximity to the other surface, the adhesion forces are higher for the smooth surface compared to the rough surface. But for case 1 the area of top surface in close proximity (but not in contact) with the flat surface is higher for the rough surface than the smooth surface. Thus in this case the

adhesion forces are slightly higher for the rough surface compared to the smooth surface.

These results suggest that the slider-disk surface roughness significantly affects the magnitude of the adhesion and contact forces and thus the stability of the HDI. From these results we can conclude that for low flying sliders the slider/disk surface should not be very rough as the magnitude of the contact forces increases and at the same time it should not be very smooth as the magnitude of the adhesion forces increases. This suggest that for maximum stability of the HDI we need some surface roughness and these optimal surface roughness values can be easily calculated using the tool developed here. In addition we also found that if the HDI is stable the roughness does not contribute much to the slider vibration.

4.5 The Effect of Waviness

In order to investigate the effect of disk waviness on slider dynamics and stability the disk topography is experimentally measured using an LDV. This data is mathematically altered to remove the large wavelength disk feature. The amplitude and the wavelength range of the disk features used in this investigation are shown in Figure 4.3. The disk velocity at the slider location is 10 m/s. Numerical simulations are carried out and the resulting slider response along the three translational and the three rotational degrees of freedom has been plotted in Figure 4.8. We found that disk features with wavelengths larger than a few μm do not significantly affect the magnitude of the adhesion forces.

We also found the amplitude of slider vibrations is a strong function of the wavelength and the disk velocity at the slider location. For example if we look at the amplitude of slider

vibration in the off-track direction we observe that the amplitude of the vibrations is large for 0.56 mm, 0.91 mm and 1.39 mm wavelengths. The corresponding frequencies are 7.17 KHz, 10.95 KHz and 17.72 KHz. These are the first three coupled sway and torsion modes of the HSA. A similar observation is made for slider vibration along the other five degrees of freedom.

These results indicate that disk waviness excites certain frequencies of the HSA and result in large slider vibrations along the three translational and the three rotational degrees of freedom. One way of reducing the FHM and the TMR is by selectively burnishing the wavelengths that can excite the critical modes of the HSA.

4.6 The Effect of Large Wavelength Disk Features

In order to study the effect of large wavelength disk features we numerically calculated slider vibrations due to several disk circumferential modes. The effect of disk circumferential mode number and the amplitude of the disk mode are investigated. Figure 4.9 shows the plot of the slider vibration as a function of the amplitude of the disk (0,1) mode. Figure 4.10 shows the plots of the slider vibration as a function of the disk circumferential mode number. We find that the slider can easily follow these large wavelength disk features and hence their contribution to the amplitude of the slider vibration is negligible along all six degrees of freedom. We also find that these features have negligible effect on the magnitude of the adhesion or the contact forces and hence they do not affect the stability of the HDI.

4.7 Conclusions

In this chapter we presented the effect of the slider-disk surface topographies on the slider

vibrations and stability. The small wavelength slider-disk surface features – with wavelength less than a few μm – significantly affect the magnitude of the adhesion and the contact forces. Very smooth and very rough surfaces are undesirable because they increase the magnitude of the adhesion forces and the contact forces, respectively. Our results indicated that for maximum HDI stability the slider and the disk surfaces should not be extremely smooth, but instead some amount of roughness is necessary.

Intermediate wavelength slider-disk surface features – with wavelengths more than a few μm but less than a few mm – excite some HSA modes and thus result in an increase in the amplitude of the slider vibration along all 6 degrees of freedom. Our results indicate that by selectively burnishing the wavelengths that can excite the critical modes of the HSA the slider vibrations can be reduced. The large wavelength disk features – with wavelengths more than a few mm – does not significantly affect the slider vibrations as the slider can easily follow these features. Figure 4.11 summarizes all these results in a single chart. It shows the plot of the wavelength and the amplitude range of the disk features that affect the vibration and the stability of the slider at the HDI.

4.8 Tables

Table 4.1: Values of the various HDI parameters

Poisson's Ratio for Disk	0.20
Poisson's Ratio for Slider	0.21
Elastic Modulus for Disk	100 GPa
Elastic Modulus for Slider	450 GPa
Combined Elastic Modulus	85.29 GPa
Hardness of Softer Material (i.e. Slider)	2.5 GPa
Energy of Adhesion	0.09 N/m

Table 4.2: Roughness parameters for combined slider-disk surface

σ (nm)	5.20	3.40	2.92	2.43	1.99	1.62	1.25	0.81	0.74	0.65	0.33	0.25
R (μm)	1.10	1.66	4.28	4.73	3.28	3.33	5.45	5.65	5.22	6.38	9.69	10.11
	Rough			→		Intermediate			→			Smooth

Table 4.3: The simulations are carried out for the following values of disk velocities at the slider location

Case 1	20 m/s
Case 2	15 m/s
Case 3	10 m/s
Case 4	5 m/s
Case 5	2 m/s

4.9 Figures

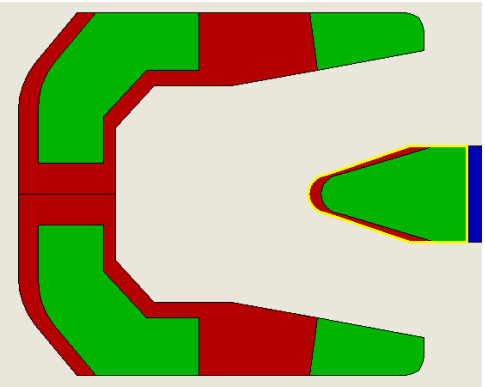

Figure 4.1: Pico slider design used in HDI simulations. The suspension pre load is 1.5 gm. The crown and camber are 25.4 nm and 2.5 nm, respectively.

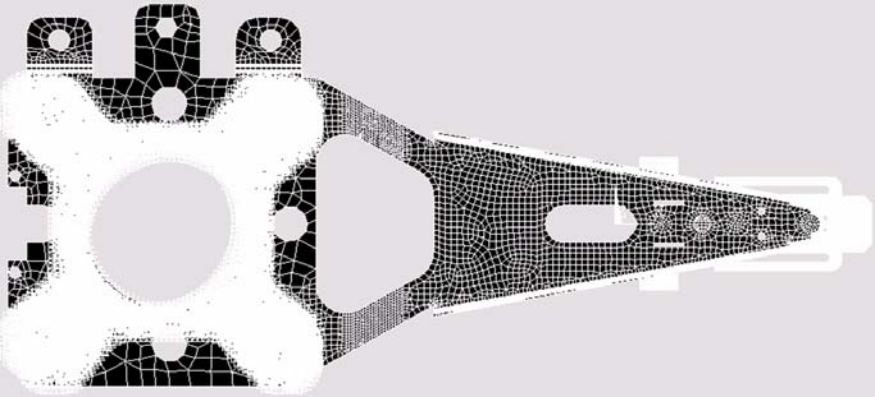

Figure 4.2: Finite element model of the suspension

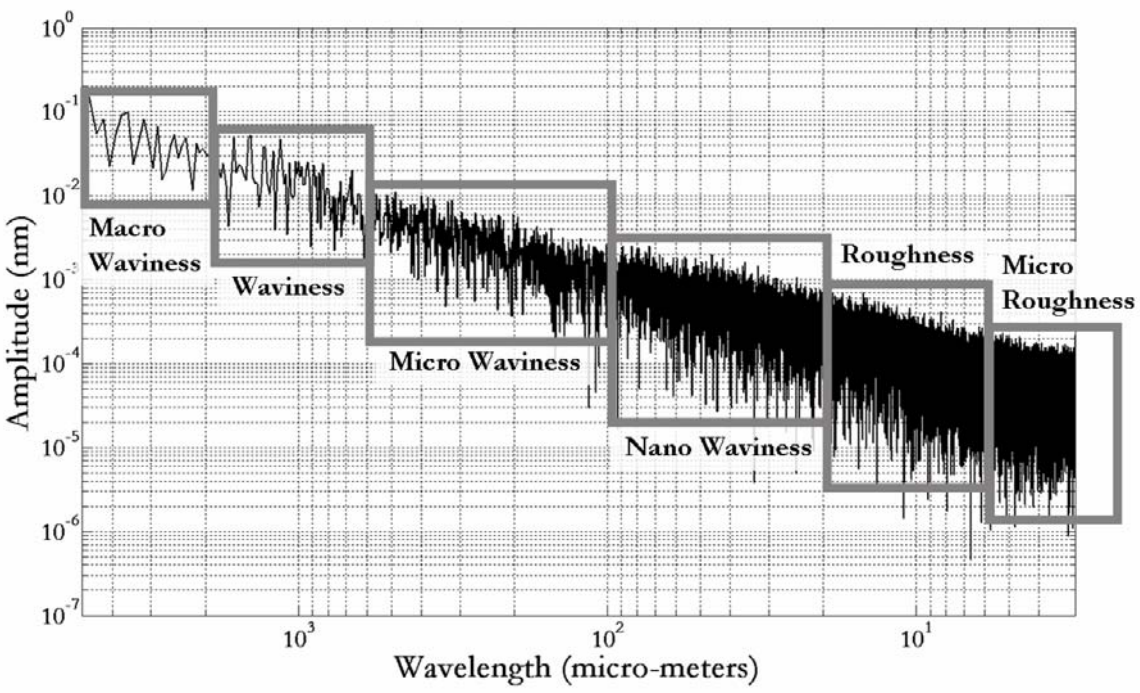

Figure 4.3: The amplitude and wavelength range of features on the disk surface.

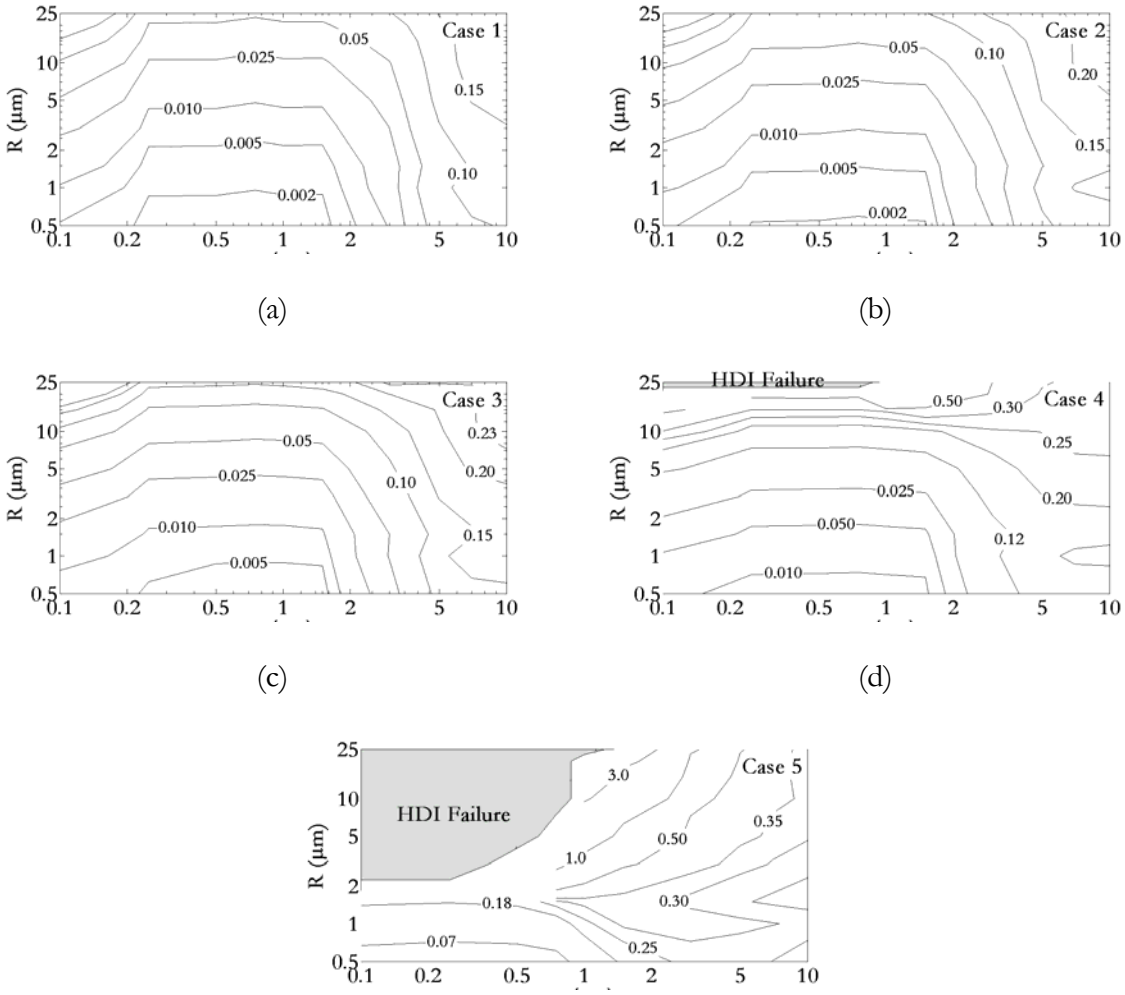

Figure 4.4: The magnitude of the adhesion forces as a function of R and σ.

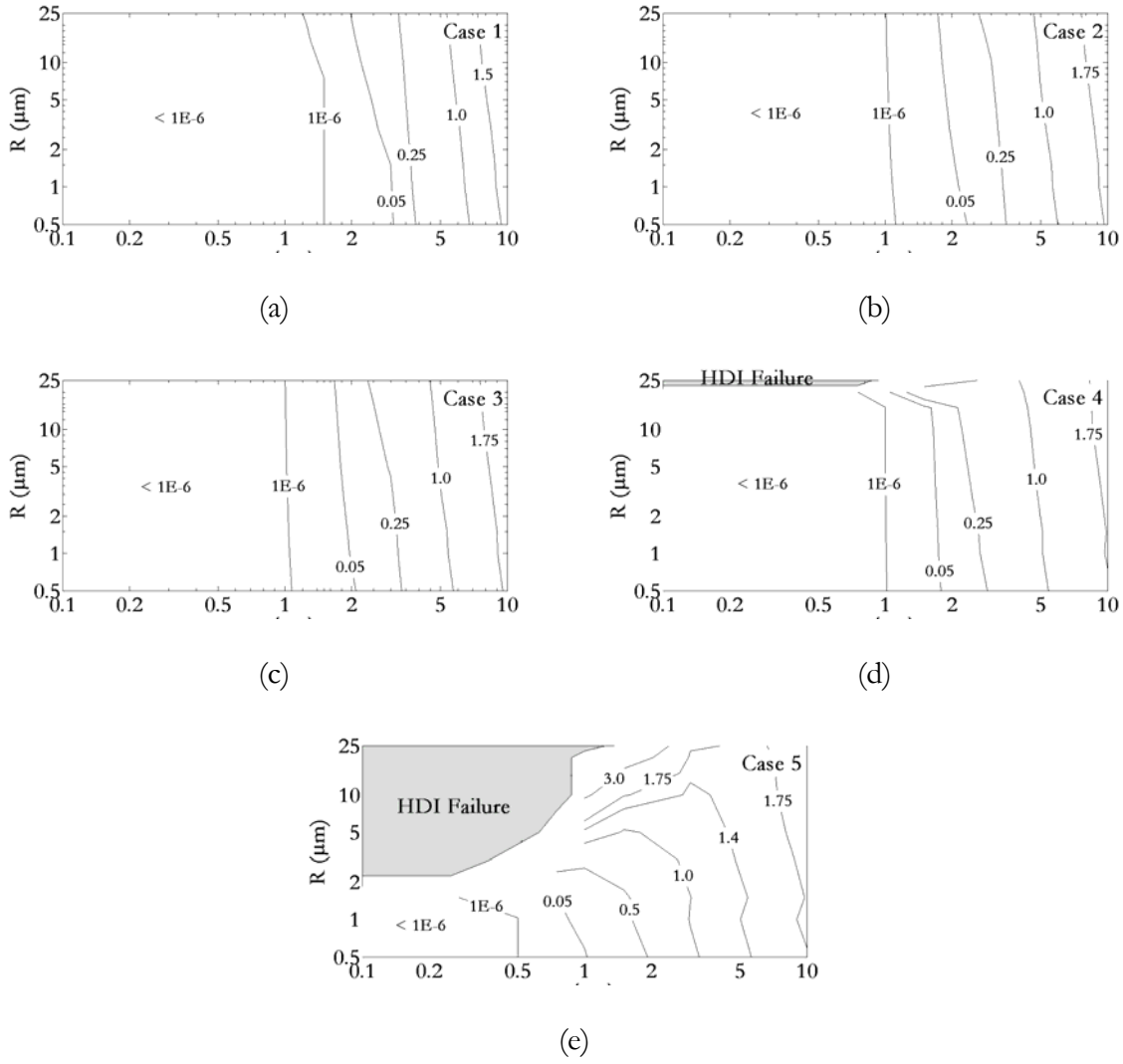

Figure 4.5: The magnitude of the contact forces as a function of R and σ.

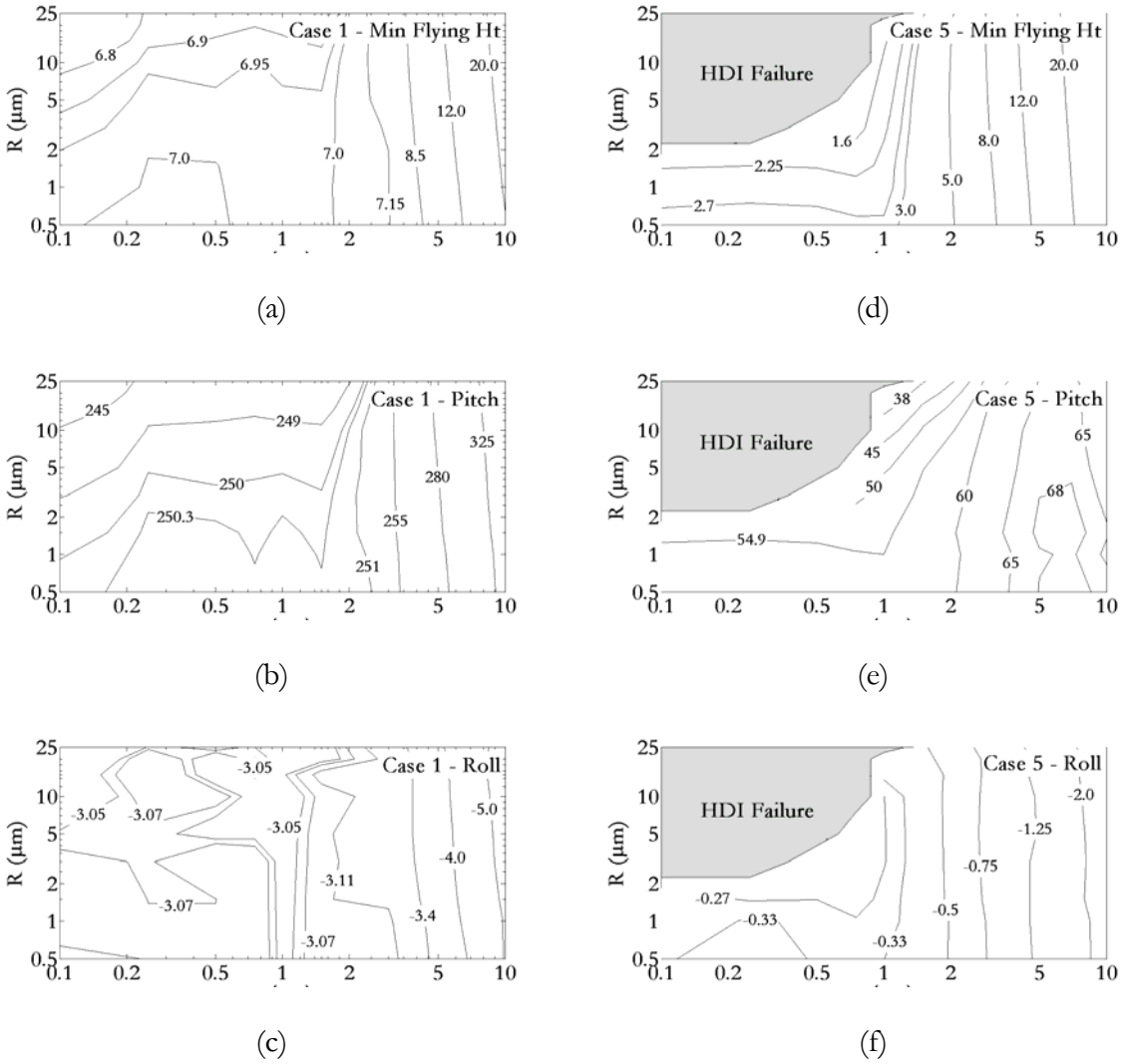

Figure 4.6: Plots (a), (b) and (c) shows the minimum mechanical spacing, pitch and roll for case 1 as a function of R and σ. Similarly, plots (d), (e) and (f) shows the minimum mechanical spacing, pitch and roll for case 5 as a function of R and σ.

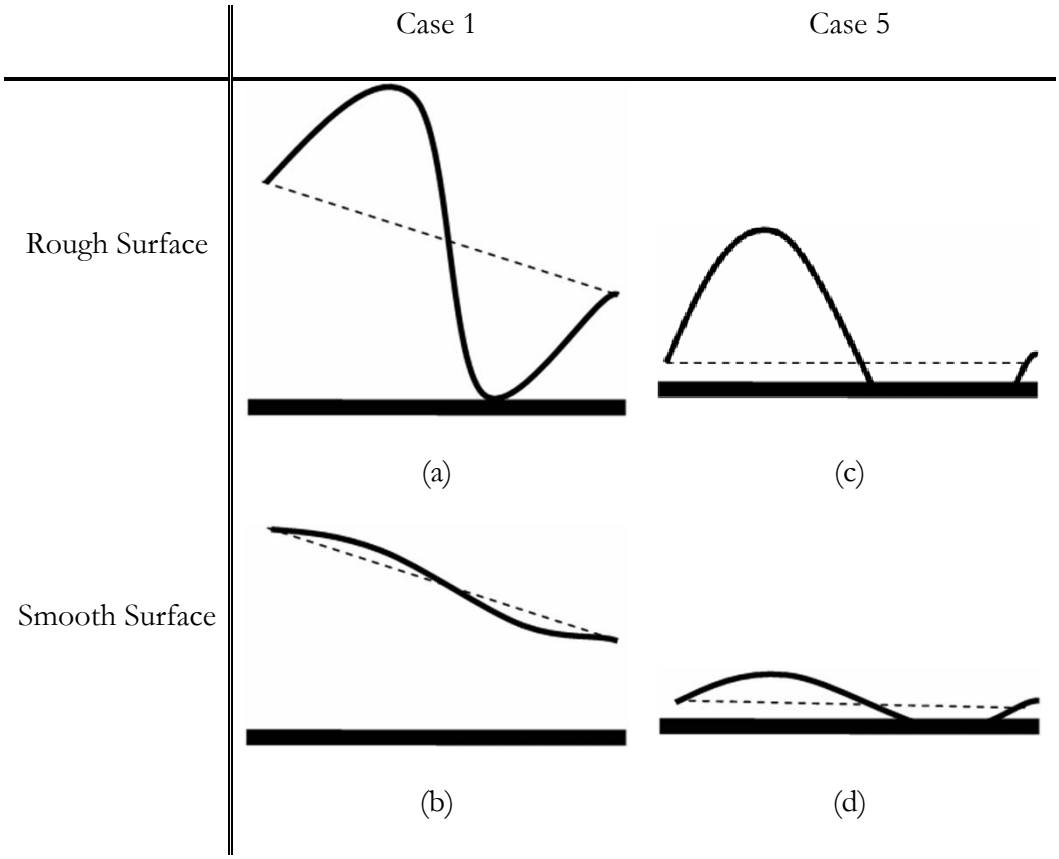

Figure 4.7: Diagrams (a) and (b) show a representation plot of the mechanical spacing between the slider and the disk for rough and smooth surfaces, respectively, for case 1. Diagrams (c) and (d) show a representation plot of the mechanical spacing between the slider and the disk for rough and smooth surfaces, respectively, for case 5.

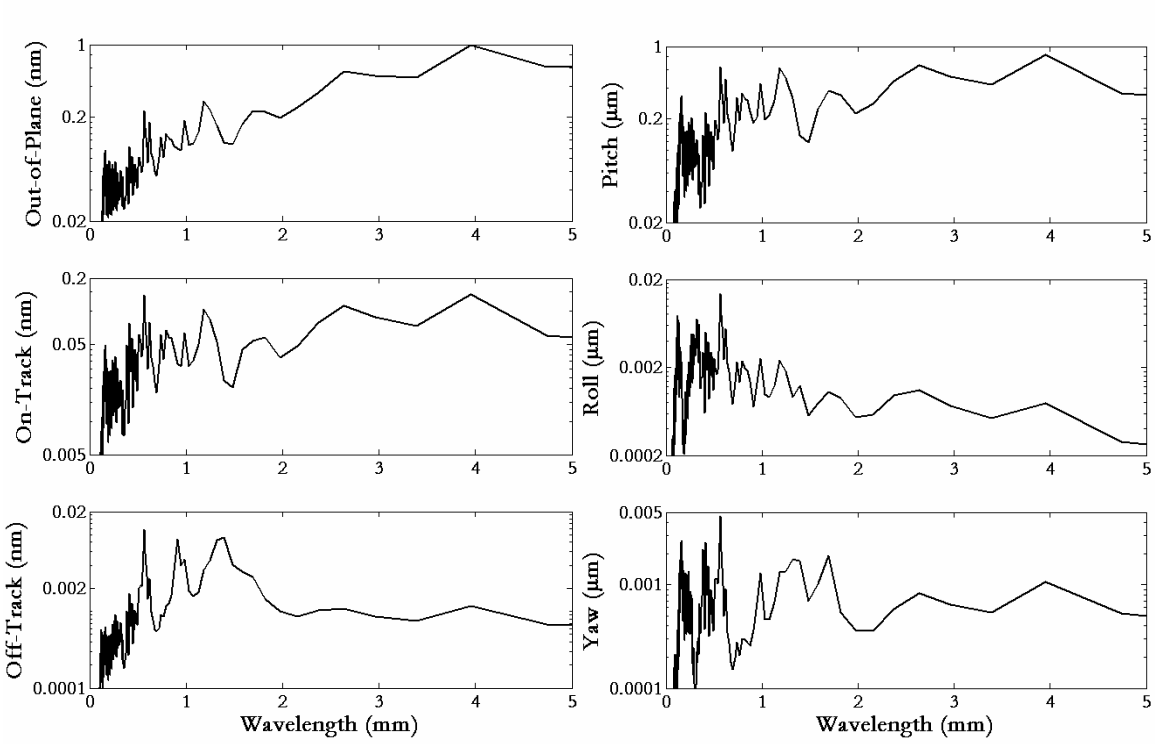

Figure 4.8: The slider's dynamics in the three translational and three rotational degrees of freedom as a function of the wavelength of the features on the disk surface.

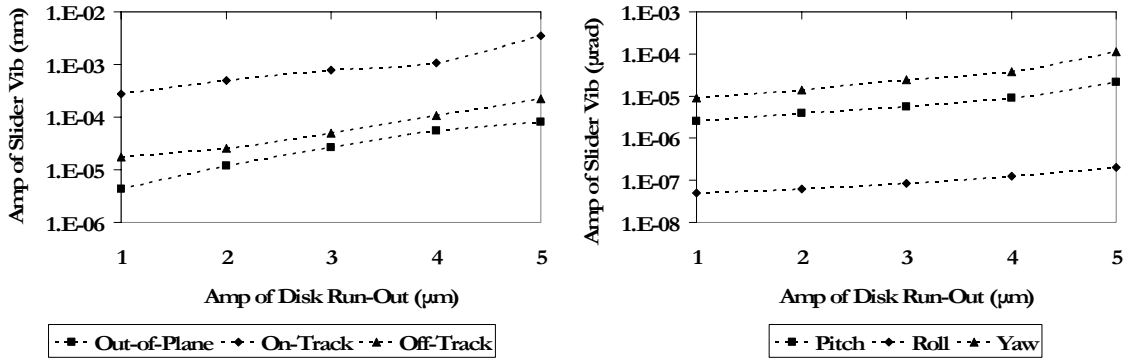

Figure 4.9: The slider's amplitude of vibration as a function of the amplitude of the disk (0,1) mode.

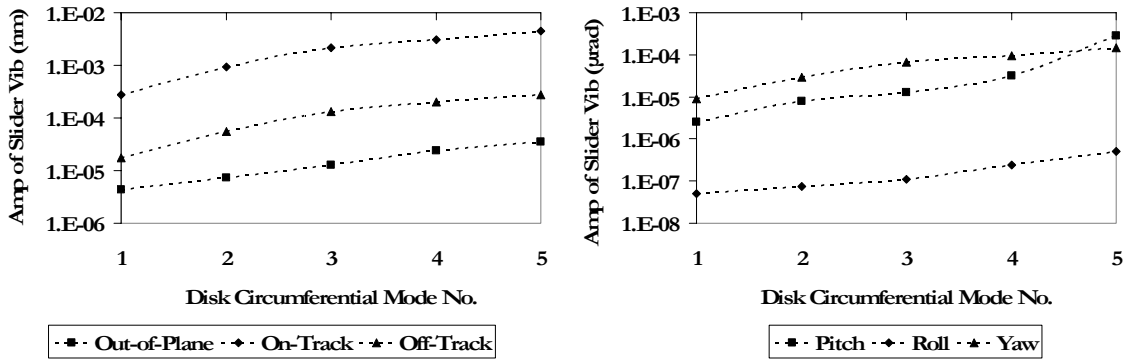

Figure 4.10: The slider's amplitude of vibration as a function of the circumferential disk mode. The amplitude of all the disk circumferential modes is 1μm.

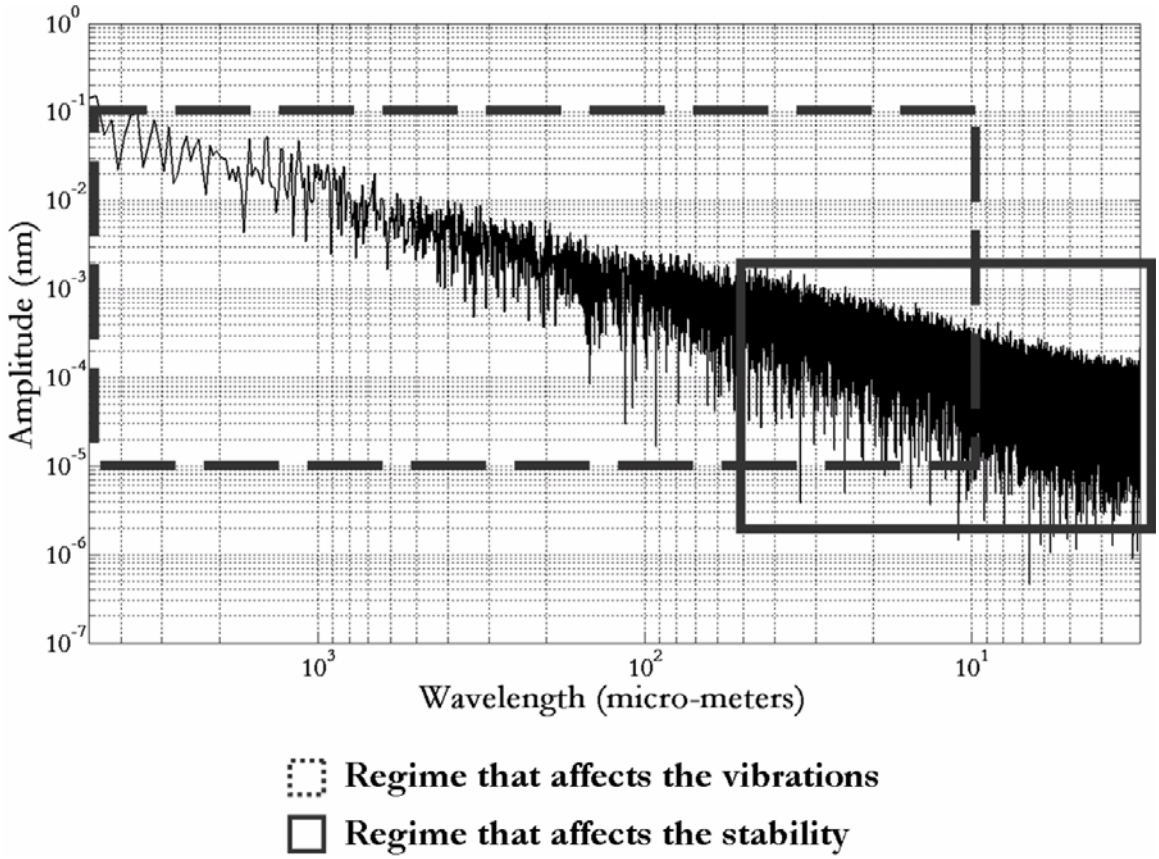

Figure 4.11: The amplitude and wavelength range of features on the disk surface that affect the vibrations and the stability of the slider at the HDI.

CHAPTER 5

AIR BEARING SLIDER'S VIBRATIONS DUE TO AIR FLOW TURBULENCE IN HARD DISK DRIVES

5.1 Introduction

Faster data access rates dictates faster disk rotation speeds which result in higher flow velocities and higher aerodynamic excitation of the HSA and the disk. This increases the slider in-plane vibrations (Figure 1.11) and hinders the recording density growth in the HDD. Thus this chapter focuses on slider vibrations due to air flow turbulence.

The flow-induced slider vibrations are calculated using the HDD model presented in chapter 2. The air flow data used to calculate the slider vibrations is computed by Kirpekar [33] using a commercial CFD software – CFD-ACE. These forces are then applied to a finite element model of the HSA to compute the flow-induced slider vibrations. This finite element model is also coupled with a finite volume solver which not only calculated the air bearing forces/moments acting on the slider, but also the contact/impact forces and the non-linear attractive forces like intermolecular, electrostatic and meniscus forces acting on a low flying sliders in the HDD.

This numerical solver can be used as a design tool to investigate the effects of disk RPM, slider radial position, flow mitigation devices, reverse spinning disks, suspension length, flow re-circulation channel and designs of several other mechanical components that alter the flow. Thus this tool can be used to evaluate and suggest optimal drive designs that minimize flow-induced slider vibrations.

The air flow calculations in hard disk drives require a large amount of computational resources and computing time – it usually takes 3-6 weeks for a single flow calculation on a 128 processor cluster. And still the error in these calculations can be as high as 20% due to a number of reasons, like the choice of commercial CFD software, grid discretizaton, time stepping, numerical dissipation and modeling assumptions like incompressibility, SGS model, boundary conditions etc. to name a few [33]. But finally all we need from the air flow calculations for predicting the off-track vibrations of the read-write head is the aerodynamic forcing on the HSA.

Thus the question arises: Is it really worth spending so much time and resources to calculate the air flow for all possible combinations of the disk RPM, the slider's radial position, and different designs of mechanical components when the errors in the air flow calculations are so high? And, is there a way to estimate the flow-induced forcing and hence the flow-induced slider vibrations as a function of disk RPM and slider radial position without actually computing the air flow for all possible combinations. In this chapter we make an attempt to answer this question. Scaling laws are proposed to estimate the slider vibrations as a function of the disk RPM and the slider's radial position.

5.2 The Model for Computing Flow-Induced Slider Vibrations

The hard disk drive model used to calculate the slider vibrations due to air flow is divided into two parts. The first part is the air flow model that calculates the air flow and thus the resulting aerodynamic forcing on the HSA. And the second part is the HDD model – presented in chapter 2 – which calculates the slider vibrations due to these aerodynamic

forces. Of course, the assumption here is that the flow affects the structural vibrations (i.e. the HSA vibrations), but the structural vibrations do not affect the flow. This assumption is reasonable because the flow-induced structural vibrations are of the order of a few nanometers. The Air flow model is described below.

Kirpekar used large eddy simulation (LES) to simulate the airflow in a 3.5 inch form factor hard disk drive model shown in Figure 5.1 [31],[32][33]. This hard disk drive model has a single disk with a single e-block arm, but two base-plates, two suspensions and two sliders. We will refer to them as the top and bottom slider, top and bottom suspension etc. in this chapter. A commercial CFD code (CFD-ACE) is used for flow calculations. The incompressible Navier-Stokes equation (5.1) with the algebraic dynamic large eddy simulation model is solved with this code using the SIMPLEC method (semi-implicit method for pressure linked equations – consistent).

$$\frac{\partial u}{\partial t} + u.\nabla u = -\frac{1}{\rho}\nabla p + \nu\nabla^2 u \qquad (5.1)$$
$$\nabla.u = 0$$

Here u, p, ϱ and ν are the velocity, pressure, density and the kinematic viscosity, respectively. In order to obtain faster convergence of the numerical solutions, all flow simulations are started from a steady k-ε solution. A detailed description of the algebraic dynamic large eddy simulation model can be found in [45] and the SIMPLEC method is discussed in detail in [46].

All the base-deck and top cover surfaces are modeled as rigid walls with no slip, while the disks are modeled as rigid rotating walls with no slip. All structural interfaces are rigidly

joined and the base of the e-block arm is assumed to be fixed. All fluid-structure interfaces are coupled for pressure and shear stress. A detailed discussion of the flow calculations can be found in [33].

Five sets of simulations are done at several disk RPM and slider radial positions as summarized in Table 5.1. The HSA makes an angle θ with the Y-axis as shown in Figure 5.1. This angle θ is 32^0, 45^0 and 57^0 for the ID, MD and OD radial positions, respectively. The corresponding slider radial positions will be referred to as R_{ID}, R_{MD} and R_{OD}, respectively. These simulations are done on a 128 processor cluster and each simulation took about 3-6 weeks for completion. The aerodynamic forces/moments on the HSA are computed for each of the five cases at 51 locations along the length of the HSA that include (a) 1 location each on the top and the bottom slider, (b) 15 locations each on the top and the bottom suspension and baseplate, and (c) 19 locations on the e-block arm. These forces/moments are then applied at the same locations in the finite element HSA model for the second part of the calculations. The second part of the calculations is carried out using the hard disk drive model which calculates the slider's displacements due to aerodynamic forces. This model is described in chapter 2.

5.3 Scaling by the Disk RPM

The force due to the impinging air flow on the HSA can be expressed as:

$$Force = \frac{1}{2} C_D \rho U^2 A \tag{5.2}$$

Here C_D and ϱ are the drag coefficient and the density of the medium (i.e. air in this case). U and A are the velocity of the impinging flow and the area of the HSA exposed to the flow.

Kirpekar has shown that the flow is highly turbulent for 3.5 inch form factor hard disk drives [31],[32]. Thus for turbulent flows C_D can be expressed as a function of the Reynolds number (Re) and hence the velocity of the impinging flow (U) as follows:

$$C_D \propto (\mathrm{Re})^{-1/5} \propto (U)^{-1/5} \tag{5.3}$$

Substituting the above expression for C_D into equation (5.2), we get

$$Force \propto U^{-1/5} U^2 \propto U^{9/5} \tag{5.4}$$

Since the disk RPM is the only variable in this case and the radial position is constant, we get

$$Force \propto (RPM)^{9/5} \tag{5.5}$$

This shows that if all variables other than the disk RPM are unchanged then the force due to the air flow scales as $RPM^{9/5}$.

The displacements of the slider due to the aerodynamic force are of the order of a few nanometers. Thus the structural response will be linear for such small displacements. So the slider displacements should also follow the same scaling law,

$$Displacement \propto (RPM)^{9/5} \tag{5.6}$$

Of course, several simplifying assumptions have been made while deriving this scaling law. Thus it is important to validate this relation between the slider displacement and the disk RPM. Three numerical simulations (C1, C2 and C3) are used to do so. As mentioned earlier, our hard disk drive model has one disk, one e-block arm and two head gimbal assemblies

(HGA). In all three simulations, the radial position of the slider is fixed at the middle diameter (MD), while the disk RPM is changed from 5400 to 7200 to 10000.

Aerodynamic forces/moments are calculated at several locations along the HSA and are applied to the finite element model of the HSA in the head-disk interface model. A representative plot of the air flow-induced forces acting along the out-of-plane, the on-track and the off-track directions for the top slider are shown in Figure 5.3. We found that on the slider – and at all other locations where the aerodynamic forces are computed – the amplitudes of the force along all three directions increase as the disk RPM increases. This is obvious from equation (5.5).

The theoretical derivation as summarized above states that the time series and the frequency spectra of the flow-induced force should scale as a function of the disk RPM. The quantity we are most interested in is the square root of the second moment of the time series, i.e. the standard deviation (SD). This is because SD is directly related to the vibrations of the slider, which is what we want to estimate. It can be easily proved that the SD should also scale in the same way as the time series. Thus the SD has been used to check the validity of the scaling law in this chapter.

Figure 5.4 shows plots of the normalized and the scaled SD for the aerodynamic force along the out-of-plane, on-track and off-track direction for the top and the bottom slider. The normalized SD is calculated by dividing the SD by $(2*7200*R_{MD})^{9/5}$ which is a constant for the three cases C1, C2 and C3. Similarly, the scaled SD is calculated by dividing the SD by $(2*\ RPM*R_{MD})^{9/5}$, which is different for the three cases C1, C2 and C3 since the disk RPM is

different for each case. We observe that the normalized SD increases with the disk RPM along the three directions and the range of variation, as defined below, is quite large. But after scaling there is a significant reduction in the range of variation along the three directions. The percentage reduction in the range of variation of the aerodynamic force on the top and the bottom slider as defined by the equation below is listed in Table 5.2.

$$Range(SD) = Max(SD) - Min(SD) \tag{5.7}$$

$$\%\,reduction = \frac{Range\,(Normalized\ SD) - Range\,(Scaled\ SD)}{Range\,(Normalized\ SD)} \times 100$$

The results in Table 5.2 show that the scaling law holds reasonably well for the aerodynamic forces acting on the slider. A similar analysis carried out for the aerodynamic forces acting on the base-plate, the suspension and the e-block arm also satisfies the scaling law.

Similarly, in order to validate equation (5.6), slider displacements due to the aerodynamic forces are calculated. Figure 5.5 shows plots of the slider displacement in the out-of-plane, on-track and off-track directions for the top slider. As expected the amplitudes of the slider vibrations increase with the disk RPM. The normalized and the scaled SD of the slider displacements in the out-of-plane, on-track and off-track directions are shown in Figure 5.6. The normalized and scaled SD are calculated in the same way as described before. We observe that the range of variation of the normalized SD of slider displacement is large, but after scaling there is a significant reduction in the range of variation. The percentage reductions in the range of variation of the SD of the slider's displacements along the three directions for the top and bottom slider are listed in Table 5.3.

These results show that the scaling law holds reasonably well for the slider's displacements

due to the aerodynamic forces along the out-of-plane, on-track and off-track directions. But still the range of variation does not reduce to zero after scaling. This is mainly due to two reasons: first, as mentioned earlier the CFD data used for this validation is not free from errors, and second, a fairly simple relationship is used to relate C_D to the Reynolds number (Re), as given by equation (5.3). Nonetheless, a similar experimental study carried out by Tadepalli and Anandan [47] also found that the slider's displacements along the out-of-plane and off-track directions measured using an LDV satisfy this scaling law.

5.4 Scaling by the Slider's Radial Position

The force due to the impinging air flow on the HSA is given by equation (5.2). Using the same analysis as presented in the last section, the force can be expressed as a function of the velocity of the flow by the equation

$$Force \propto U^{-1/5} U^{2} \propto U^{9/5} \tag{5.8}$$

Here U is the velocity of the impinging flow. Since the slider's radial position is the only variable in this case and the disk RPM is constant, we get

$$Force \propto (Radius)^{9/5} \tag{5.9}$$

This shows that if all variables other than the slider's radial position are unchanged then the force due to the air flow scales as $Radius^{9/5}$.

But in this case the on-track and the off-track directions change as the slider moves from ID to OD. Thus the correct scaling law for this case should be

$$Force \propto (Radius)^{9/5} f(\theta) \tag{5.10}$$

Here $f(\theta)$ is a function that compensates for the change in the on-track and off-track directions as the slider moves from ID to OD. And θ is the angle that the actuator makes

with the global Y-axis as shown in Figure 5.1. This function f(θ) can be easily computed for any choice of global coordinates and hence the explicit formulation has been omitted in this chapter.

The displacements of the slider due to the aerodynamic force are of the order of a few nanometers. Thus the structural response will be linear for such small displacements. So the slider's displacements should also follow the same scaling law,

$$Displacement \propto (Radius)^{9/5} f(\theta) \tag{5.11}$$

Here again several simplifying assumptions have been made while deriving the scaling law. Thus is it important to validate this relation between the slider's displacement and the slider's radial position. Three numerical simulations (C4, C2 and C5) are used to do so. As mentioned earlier, our hard disk drive model has one disk, one e-block arm and two head gimbal assemblies (HGA). The disk RPM is kept constant at 7200 for these simulations, while the slider's radial position is changed from ID to MD to OD.

Aerodynamic forces/moments are calculated at several locations along the HSA and are applied to the finite element model of the HSA in the head-disk interface model. A representative plot of the air flow-induced forces acting along the out-of-plane, the on-track and the off-track directions for the top slider is shown in Figure 5.7. We observe that on the slider – and at all other locations where the aerodynamic forces are computed – the amplitudes of the force along the three directions increase as the slider moves from ID to OD. This is obvious from the equation (5.10).

As detailed in the last section, the SD of the flow-induced forces is used to validate the scaling law as given by the equation (5.10). Figure 5.8 shows plots of the normalized and the scaled SD for the aerodynamic forces along the out-of-plane, on-track and off-track directions for the top and the bottom sliders. The normalized SD is calculated by dividing the SD by $(2*7200*R_{MD})^{9/5}$, which is a constant for the three cases C4, C2 and C5. Similarly, the scaled SD is calculated by dividing the SD by $(2*7200*R)^{9/5}$, which is different for the three cases C4, C2 and C5 since the slider's radial position is different for each case. We observe that the normalized SD increases along the out-of-plane, on-track and off-track directions as the slider moves from ID to OD, and the range of variation is quite large. But after scaling there is a significant reduction in the range of variation along the three directions. The percentage reduction in the range of variation of the aerodynamic force acting on the top and the bottom sliders as defined by the equation (5.7) is listed in Table 5.4.

The results in Table 5.4 show that the scaling law holds reasonably well for the aerodynamic forces acting on the slider. A similar analysis carried out for the aerodynamic forces acting on the base-plate, the suspension and the e-block arm also satisfies the scaling law given by the equation (5.10).

Similarly, in order to validate equation (5.11), slider displacements due to the aerodynamic forces are calculated. Figure 5.9 shows plots of the slider's displacements in the out-of-plane, on-track and off-track directions for top slider. As expected the amplitudes of the slider's vibrations increase as the slider moves from ID to OD. The normalized and the scaled SD of the slider's displacements in the out-of-plane, on-track and off-track directions are plotted

in Figure 5.10. The normalized and scaled SD calculations are the same as described above. We observe that the range of variation of the normalized SD of slider displacement is large, but after scaling there is a significant reduction in the range of variation. The percentage reductions in the range of variation of the SD of the slider's displacements along the three directions for the top and bottom slider are listed in Table 5.5.

This shows that the scaling law holds reasonably well for the slider's displacements due to the aerodynamic forces along the out-of-plane, on-track and off-track directions. Hear again the range of variation does not reduce to zero after scaling. And, as mentioned before, the uncertainty in the CFD data and a fairly simple model for the variation of C_D with the Reynolds number (Re) are the two main sources of error. It should be noted that in the presence of mechanical components that alter the flow on the disk pack, such as blocking plates, upstream and downstream spoilers etc., this scaling law will no longer be valid, especially at the outer diameter (OD).

5.5 Conclusions

In order to compute the flow-induced slider vibrations, all we need are the aerodynamic forces acting on the HSA. But the air flow calculations – using CFD packages – for all possible combinations of the disk RPM and the slider's radial position can be computationally very expensive. Thus an alternative strategy is suggested in this chapter. Two scaling laws are derived to predict the amplitudes of the aerodynamic forces on the HSA and hence the resulting slider vibrations as a function of the disk RPM and the slider's radial position. And these laws are validated using the numerical computations.

Further, if the experimentally measured slider vibrations data is available along the out-of-plane, on-track and off-track directions for a particular disk RPM and slider radial position, then using these scaling laws the slider's vibrations can be predicted at all other combinations of disk RPM and slider radial position with reasonable accuracy.

5.6 Tables

Table 5.1: The simulations are carried out for the following combinations of the disk RPM and the slider radial position

	Disk RPM	Slider radial Position
Case 1 (C1)	5400	Middle Diameter (MD)
Case 2 (C2)	7200	Middle Diameter (MD)
Case 3 (C3)	10000	Middle Diameter (MD)
Case 4 (C4)	7200	Inner Diameter (ID)
Case 5 (C5)	7200	Outer Diameter (OD)

Table 5.2: The percentage reduction in the range of variation of the standard deviation of the aerodynamic force acting on the slider

	Top Slider	Bottom Slider
Out-of-Plane	72.5	93.0
On-Track	85.6	88.7
Off-Track	87.0	84.0

Table 5.3: The percentage reduction in the range of variation of the standard deviation of the slider displacement

	Top Slider	Bottom Slider
Out-of-Plane	77.4	84.0
On-Track	88.4	91.1
Off-Track	81.4	76.5

Table 5.4: The percentage reduction in the range of variation of the standard deviation of the aerodynamic force acting on the slider

	Top Slider	Bottom Slider
Out-of-Plane	81.1	84.7
On-Track	85.7	86.6
Off-Track	86.3	87.1

Table 5.5: The percentage reduction in the range of variation of the standard deviation of the slider displacement

	Top Slider	Bottom Slider
Out-of-Plane	93.4	97.4
On-Track	87.9	86.0
Off-Track	87.9	88.9

5.7 Figures

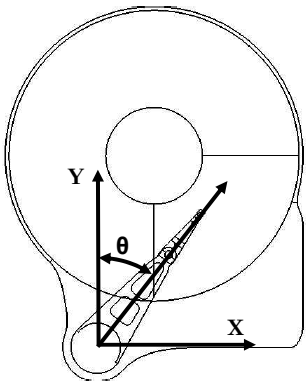

Figure 5.1: A hard disk drive model used for air flow simulations

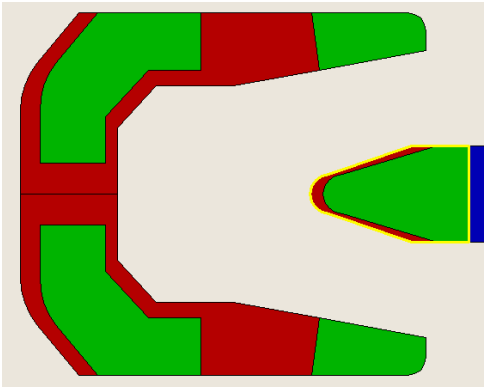

Figure 5.2: Pico slider design used in HDI simulations. The suspension pre load is 1.5 gm.

The crown and camber are 25.4 nm and 2.5 nm, respectively.

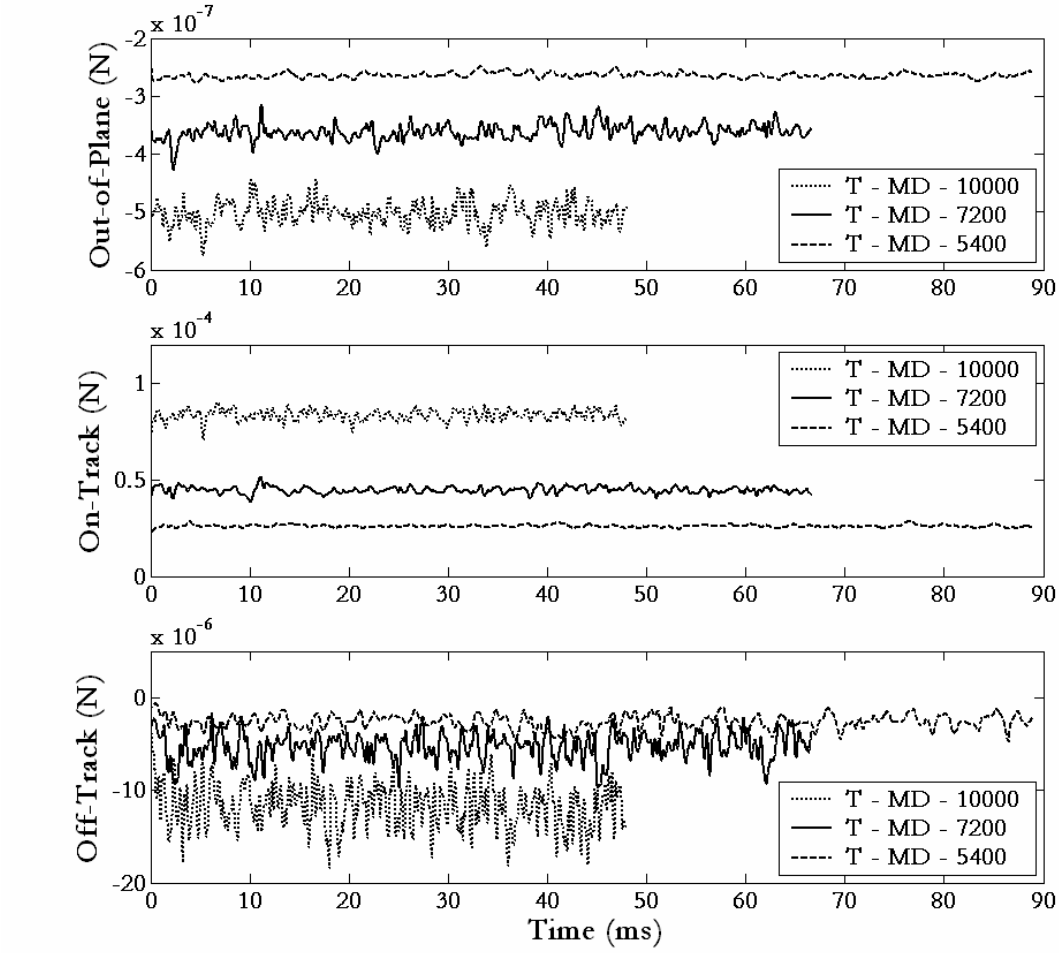

Figure 5.3: Aerodynamic forces acting on the top (T) slider at MD position for disk RPM of 5400, 7200 and 10000.

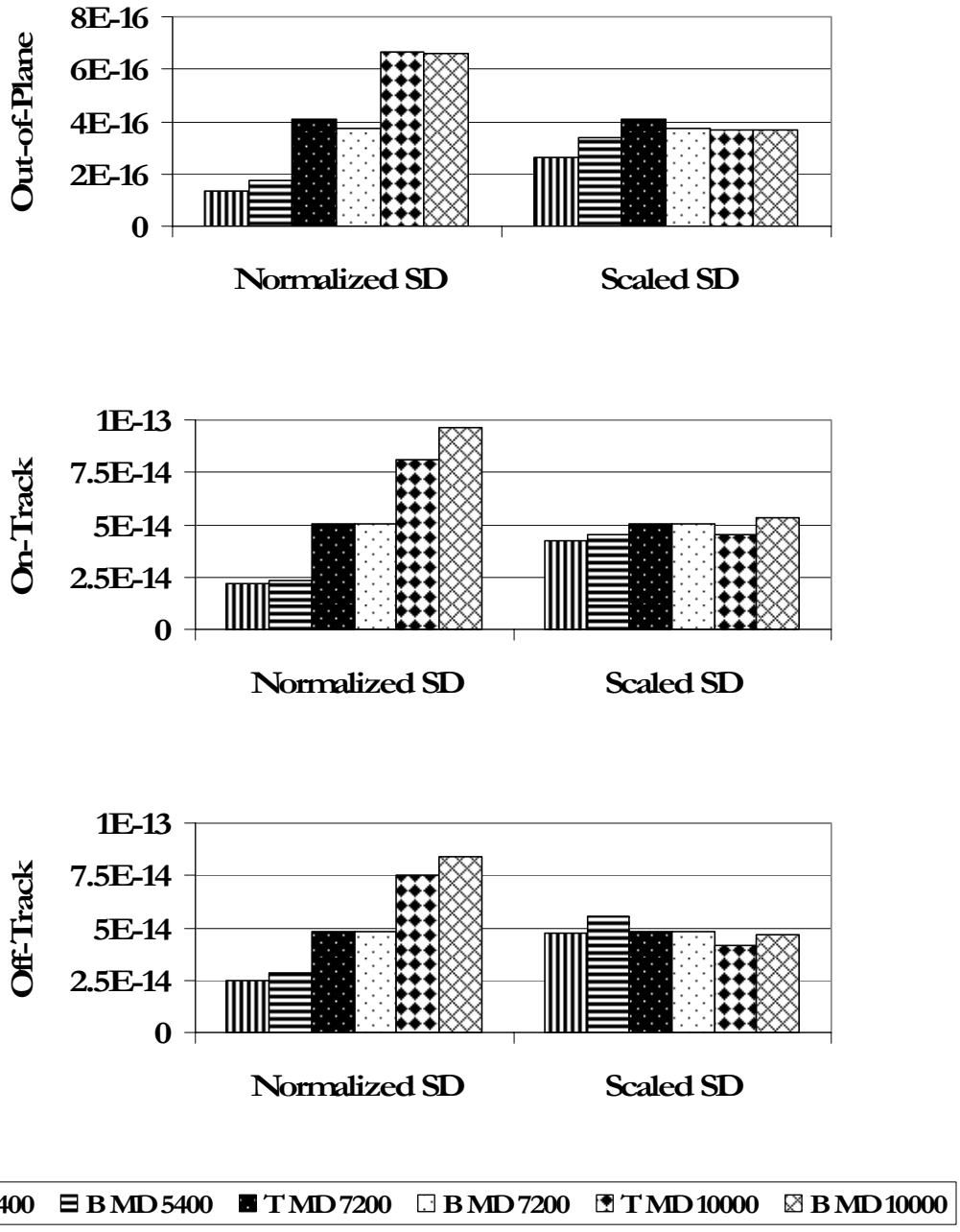

Figure 5.4: Normalized and scaled standard deviation of the aerodynamic forces acting on the top (T) and the bottom (B) slider at MD position for disk RPM of 5400, 7200 and 10000.

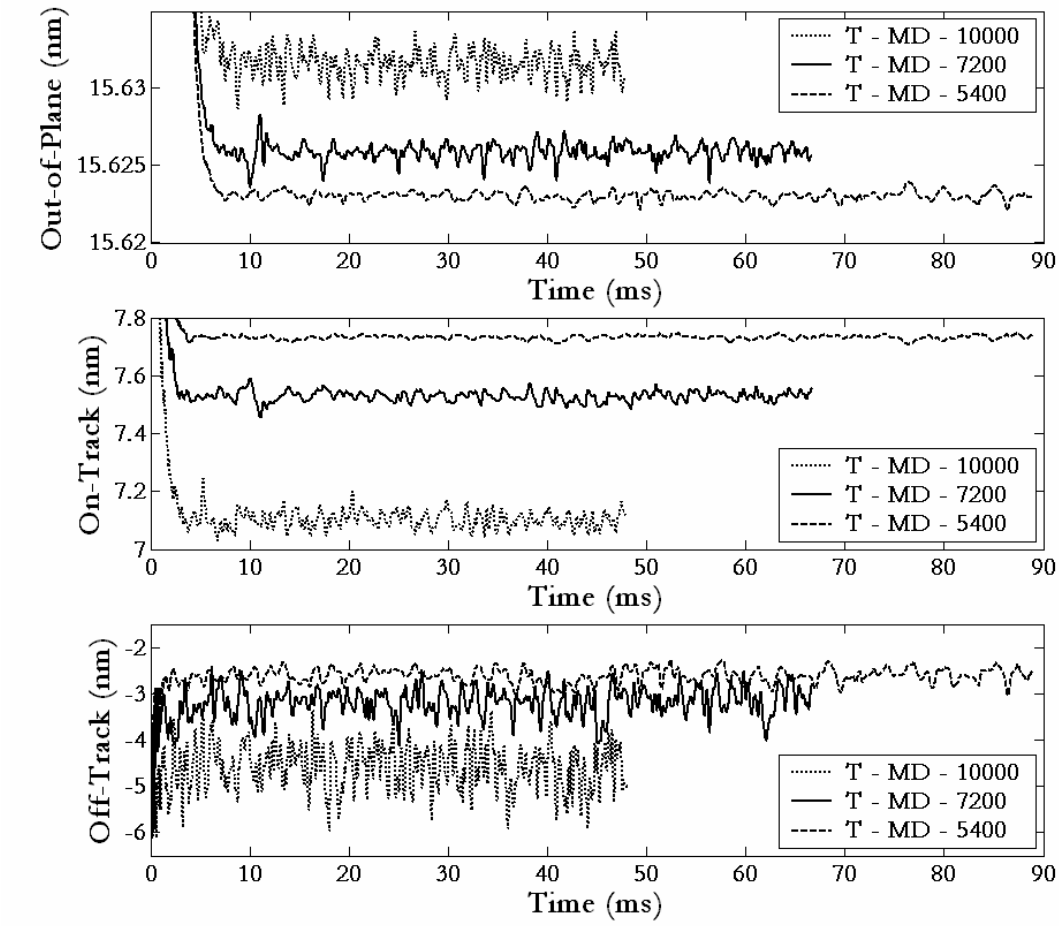

Figure 5.5: Displacements of the top (T) slider at the MD position for disk RPM of 5400, 7200 and 10000.

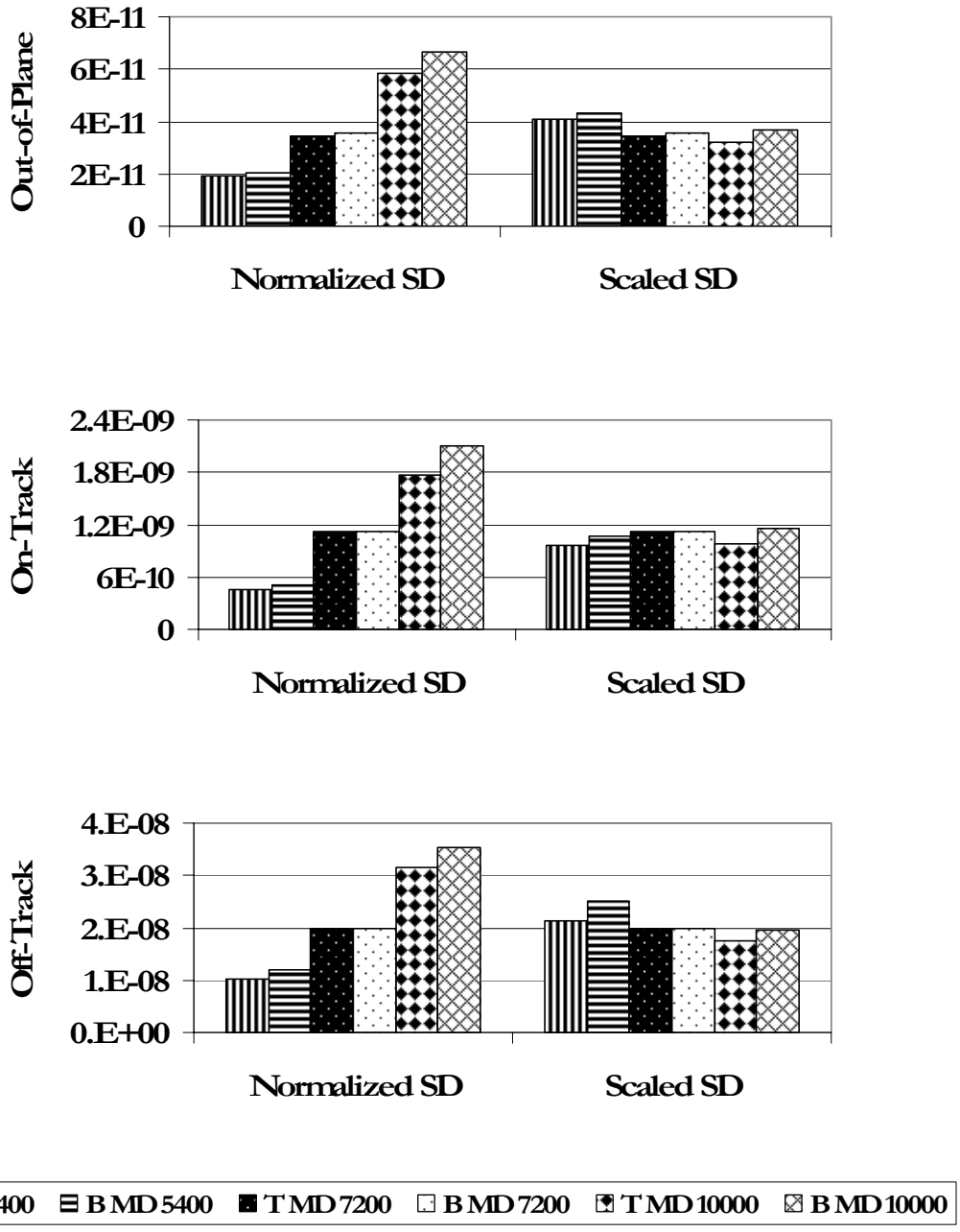

Figure 5.6: Normalized and scaled standard deviation of the displacements of the top (T) and the bottom (B) slider at MD position for disk RPM of 5400, 7200 and 10000.

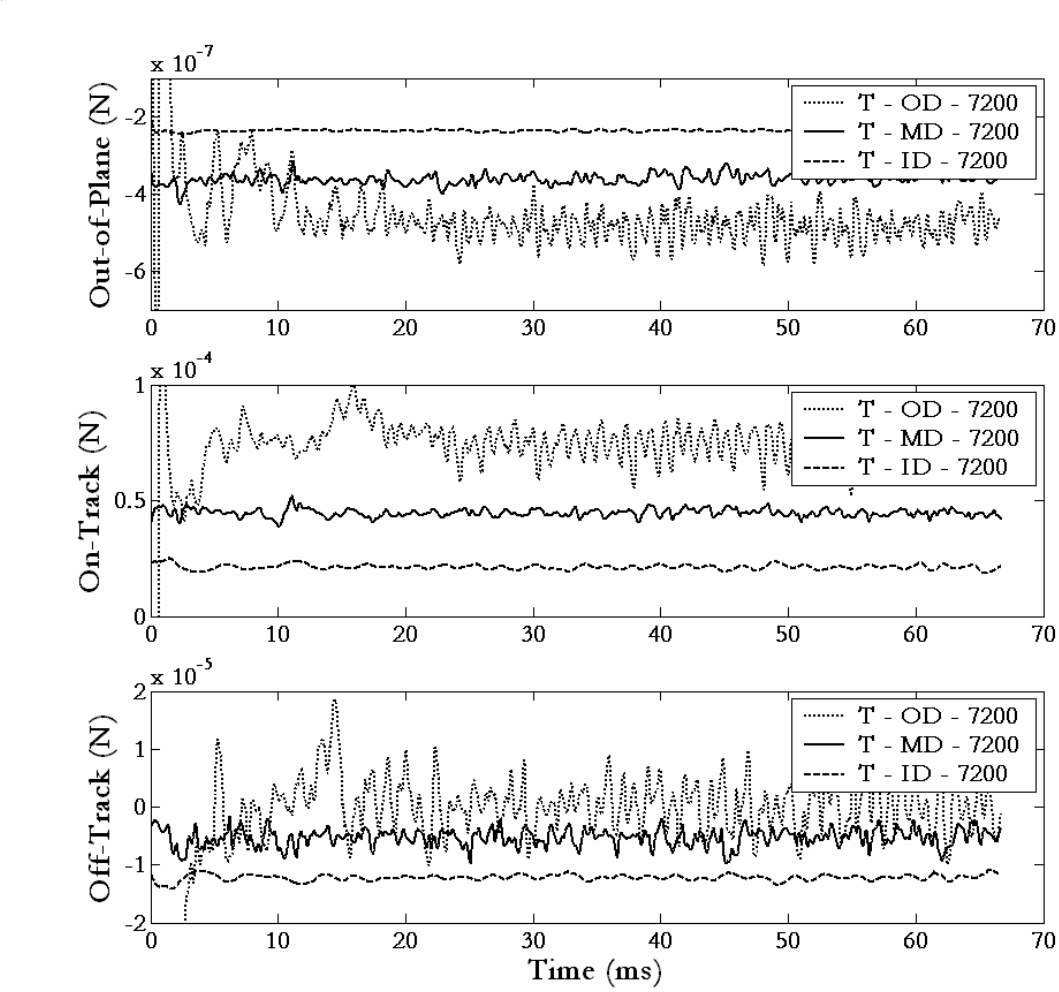

Figure 5.7: Aerodynamic forces acting on the top (T) slider at ID, MD and OD locations for disk RPM of 7200.

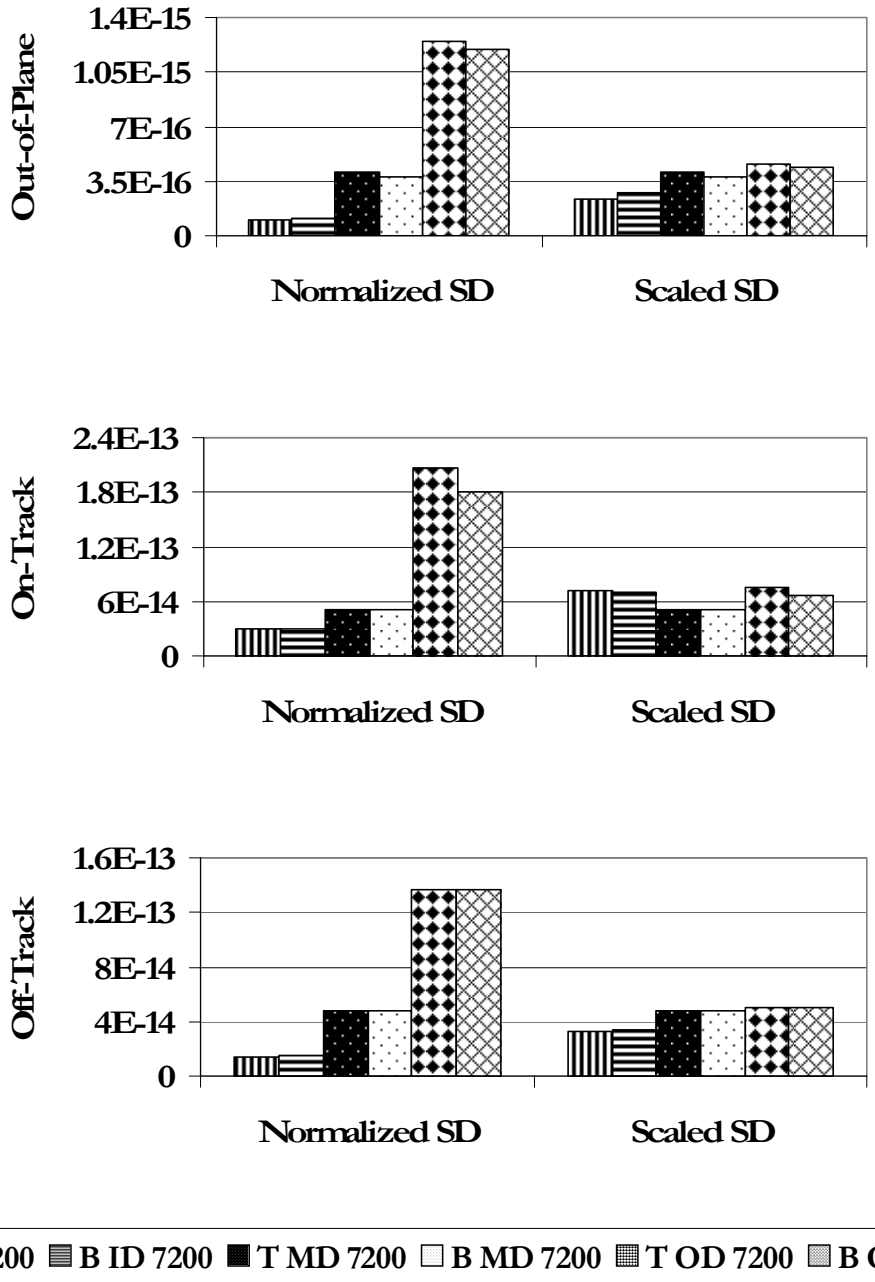

Figure 5.8: Normalized and scaled standard deviation of the aerodynamic forces acting on the top (T) and the bottom (B) slider at ID, MD and OD position for disk RPM of 7200.

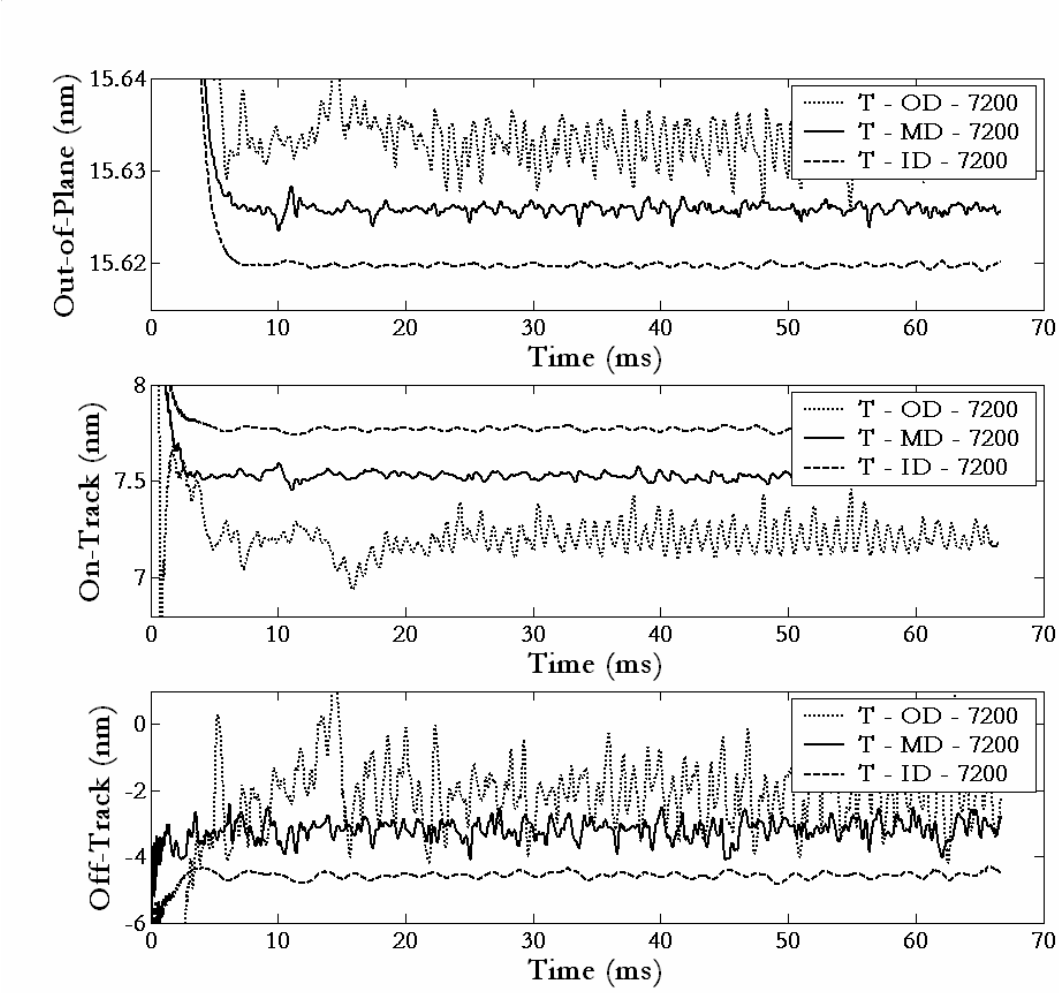

Figure 5.9: Displacements of the top (T) slider at the ID, MD and OD position for the disk RPM of 7200.

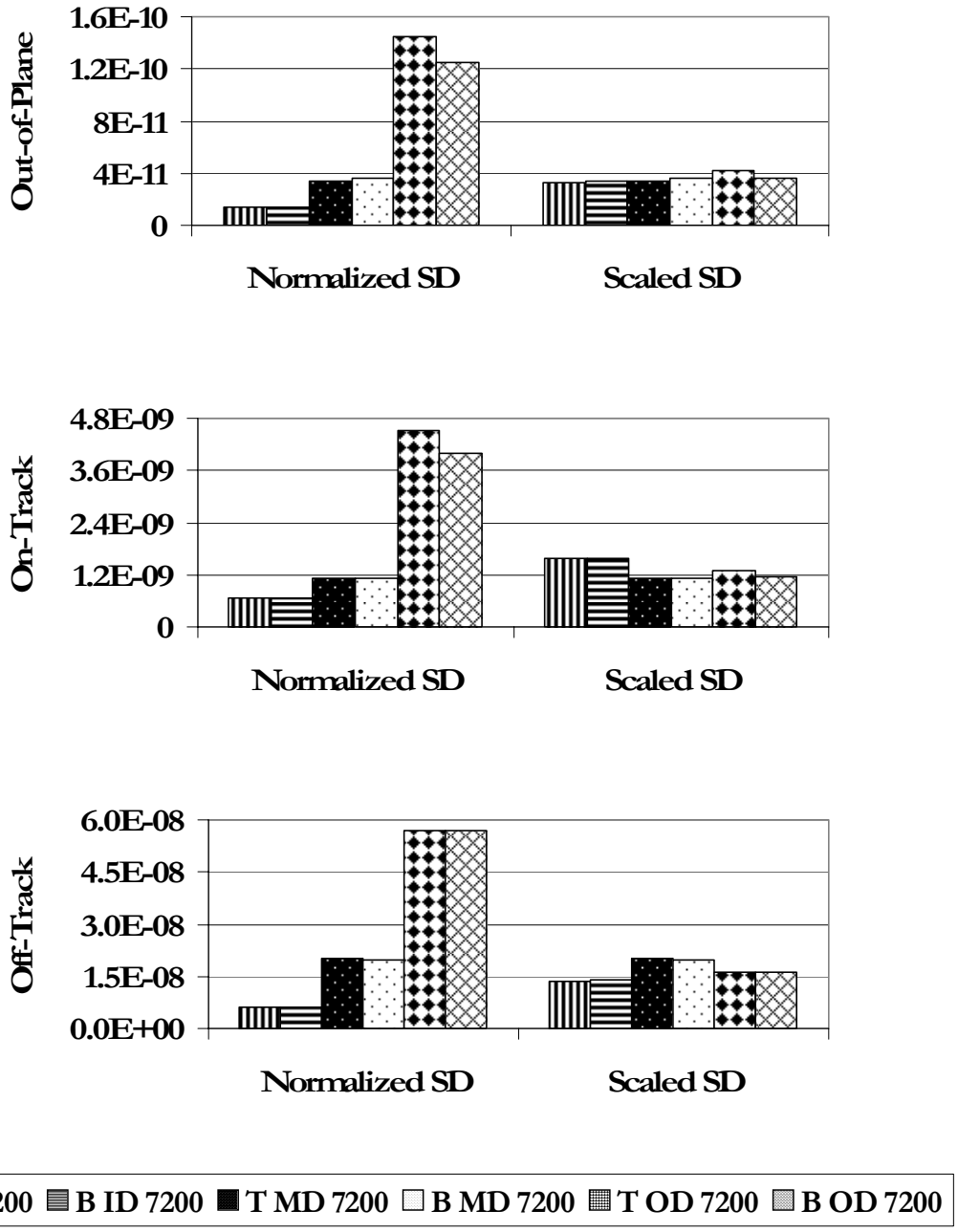

Figure 5.10: Normalized and scaled standard deviations of the displacements of the top (T) and the bottom (B) slider at ID, MD and OD position for disk RPM of 7200.

CHAPTER 6

STRATEGIES FOR REDUCING FLOW-INDUCED SLIDER VIBRATIONS IN HARD DISK DRIVES

6.1 Introduction

Faster data access rates dictates faster disk rotation speeds which result in higher flow velocities and higher aerodynamic excitation of the HSA and the disk. This increases the slider in-plane vibrations and hinders the recording density growth in the HDD. Thus in this chapter the effectives of a few commonly used flow mitigation devices like the blocking plate, upstream and downstream spoilers etc. is reported in terms of (a) the reduction in slider vibrations especially in the off-track direction and (b) the resulting penalty in terms of higher operating costs due to increased power consumption. Several other strategies like spinning the disks in reverse direction and reducing the suspension length in order to reduce the flow-induced slider vibrations are also presented in this chapter.

6.2 The Model for Computing Flow-Induced Slider Vibrations

As discussed in the previous chapter, the hard disk drive model used to calculate the slider vibrations due to air flow is divided into two parts. The first part is the air flow model – presented in chapter 5 – that calculates the air flow and thus the resulting aerodynamic forcing on the HSA. And the second part is the HDD model – presented in chapter 2 – which calculates the slider vibrations due to these aerodynamic forces.

In this chapter we discuss the effects of flow mitigation devices, reverse spinning disk, suspension length, disk RPM and slider's radial position. The three flow mitigation devices

investigated are a blocking plate, downstream spoiler and upstream spoiler, as shown in Figure 6.2. Five sets of air flow simulations are done for the configurations listed in Table 6.1. The air flow data is computed by Kirpekar [33] using a commercial CFD software – CFD-ACE. In these simulations the HSA makes an angle of 38^0 with the Y-axis as shown in Figure 6.1. The aerodynamic forces/moments on the HSA are computed for each of the five cases at 51 locations that include (a) 1 location each on the top and the bottom slider, (b) 15 locations each on the top and the bottom suspension and baseplate, and (c) 19 locations on the e-block arm and the actuator. These forces/moments are then applied at the same locations in the finite element HSA model for the second part of the calculations. The second part of the calculations is carried out using the HDI model which calculates the slider's displacements due to aerodynamic forces. This model is described in chapter 2.

6.3 The Effect of Flow Mitigation Devices

The air flow in the HDD in the presence of the flow mitigation devices was first investigated by Kirpekar et al. [48]. Based on their finding, three flow mitigation devices – the blocking plate (C2), the downstream spoiler (C3) and the upstream spoiler (C4) as shown in Figure 6.2 – are investigated in the study. The dimensions of the three flow mitigation devices are listed in Table 6.2. Air flow simulations are carried out for drives with these devices and compared with a generic case (C1). The air flow data for the four configurations – C1, C2, C3 and C4 – are computed by Kirpekar [33] using a commercial CFD software – CFD-ACE. In this chapter we present a brief summary identifying the key features of the flow that affect the amplitudes of the slider's in-plane and out-of-plane vibrations.

Figure 6.3 (a) and (b) show the standard deviation of the in-plane velocity fluctuation along

the upstream and downstream side of the E-block and the upper HGA. Figure 6.3 (c) and (d) show the same for the E-block and the lower HGA. Similarly, Figure 6.4 (a) and (b) show the standard deviation of the in-plane pressure fluctuation along the upstream and downstream sides of the E-block and the upper HGA. Figure 6.4 (c) and (d) show the same for the E-block and the lower HGA. The x-axis in all these plots is the length of the actuator in meters. It has been shown earlier that the form drag due to the pressure forces is 2 orders of magnitude higher than the viscous drag on the HSA [48]. This implies that the in-plane pressure fluctuation data along the length of the HSA is a good indicator of the resulting structural vibrations. In addition the velocity fluctuation near the HSA also changes the circulation and thus the forces acting on the HSA.

Flow results for C2 when compared with C1 (Figure 6.3 and Figure 6.4) indicate that the blocking plate reduces the mean velocity of the flow in a significant portion of the drive, especially in the outer diameter regions where the flow velocities are relatively large without the blocking plate. As a result the in-plane and the out-of-plane velocity fluctuations are reduced near the slider and the suspension. Moreover, the in-plane pressure fluctuations near the base-plate are also reduced significantly. However the trailing edge of the blocking plate acts as a source of vorticity shedding and results in an increased turbulence intensity of the flow approaching the e-block arm. This results in a slight increase in the in-plane and the out-of-plane velocity fluctuations near the e-block arm.

Flow results for C3 when compared with C1 (Figure 6.3 and Figure 6.4) indicate that the downstream spoiler blocks the flow downstream of the actuator and thus reduces the flow velocities in the outer diameter region of the entire drive. As a result the in-plane velocity

and pressure fluctuations are significantly reduced near the e-block arm. The out-of-plane velocity fluctuations are also reduced near the HSA. However the downstream spoiler acts as a source of vorticity shedding and also causes flow reversal in a significant portion of the drive. As a result the in-plane velocity and pressure fluctuations slightly increase near the slider and the suspension.

Flow results for C4 when compared with C1 (Figure 6.3 and Figure 6.4) indicate that the upstream spoiler acts as a source of vorticity shedding and results in an increased turbulence intensity of the flow approaching the HGA and the e-block arm. As a result the in-plane velocity and pressure fluctuations increase near the HGA and the actuator.

These aerodynamic forces are then applied to the finite element HSA model for the second part of the calculations in order to calculate the resulting slider vibrations. Figure 6.5 shows plots of the top slider's displacements in the out-of-plane, on-track and off-track directions about arbitrary mean displacements. The mean displacement values have been shifted in order to increase the clarity in the plots. Figure 6.6 plots the standard deviations and the peak-to-peak values of the top slider's displacements in the out-of-plane, on-track and off-track directions.

Figure 6.5 shows that the in-plane slider vibrations are reduced by about 50% with the blocking plate. This is because the blocking plate reduces the in-plane pressure fluctuations and hence the form drag near the slider and the suspension. Although the in-plane pressure fluctuations are slightly increased near the e-block, the effect of the resulting form drag on the e-block is much smaller on the in-plane slider vibrations. The in-plane slider vibrations

are not reduced significantly by the downstream spoiler. Although the downstream spoiler significantly reduces the form drag near the e-block arm and the actuator, but the form drag near the slider is increased slightly. With the upstream spoiler there is a significant increase (about 75%) in the in-plane slider vibrations. This is because of the increased turbulence intensity due to vortex shedding of the flow approaching the HGA and the e-block arm.

Table 6.3 lists the power consumed by the rotating disks for the four cases. We observe that the power consumption increases significantly with the use of the blocking plate. From these results we can conclude that the blocking plate significantly reduces the in-plane slider vibrations but the operating costs increases by about 18%. It should be noted that this analysis is carried out for only one position of the actuator. The results might change at other positions because the flow mitigation devices will result in different pressure fluctuations on the slider, suspension, base plate and the e-block arm. Moreover, subtle changes in the design of the mechanical components in the drive can change the flow around the HSA significantly. Under these conditions the effectiveness of the three flow mitigation devices we have investigated might change. Nonetheless, it is expected that these results will be useful for drive designers who strive to achieve optimal designs that minimize the slider vibrations with minimal increase in the operating costs.

6.4 The Effect of Reverse Spinning Disks

In order to reduce the flow-induced slider in-plane vibrations, the aerodynamic force must be reduced. Another way of reducing this force is by spinning the disks in the reverse (clockwise) direction [49]. This is because with reverse spinning the HSA is better aligned with the streamlines of the flow than with normal spinning. And this in turn reduces the

aerodynamic forces on the HSA.

In order to validate this claim, air flow simulations are carried in the hard disk drive model shown in Figure 6.1, but with the reversed direction of the rotation of the disks (C5). These flow results are then compared with the generic configuration (C1). We found a significant reduction in the magnitude of the aerodynamic forces acting on the slider, suspension, base plate and the e-block arm. Figure 6.7 is a representative plot of the aerodynamic forces acting on the HSA for cases C1 and C5. It shows the resultant forces acting on the HSA in the out-of-plane, on-track and off-track directions. We observe that the directions of the resultant forces in the on-track and the off-track directions are opposite for the two cases C1 and C5. This effect should be obvious because the flow impinges on the HSA from the opposite side when the direction of disk rotation changes. We also observe that the peak-to-peak values of the out-of-plane, on-track and off-track forces also reduce for reverse spinning disks. This validates our earlier hypothesis that for reverse spinning disks the magnitude of the aerodynamic force reduces.

These aerodynamic forces are then applied to the finite element HSA model for the second part of the calculations in order to calculate the resulting slider vibrations. Figure 6.8 shows the plots of the slider's displacements in the out-of-plane, on-track and off-track directions. Figure 6.9 shows the plots of the standard deviations and the peak-to-peak values of the slider's displacement in the out-of-plane, on-track and off-track directions. We observe that the in-plane and out-of-plane slider vibrations for the reverse spinning disks are about $1/3^{rd}$ of the corresponding values for the normal spinning disks. This is because the drag force is significantly reduced for the reverse spinning disks. Moreover, the power consumed by the

reverse spinning disk is significantly less than the power consumed by the normal spinning disks.

We also found that reduction in slider vibration is more for the HGA between two co-rotating disks and less for HGA's between the top-cover and disk pack or base-deck and disk pack. Moreover, the effect of reverse spinning disks becomes increasingly more significant as the spacing between the disks decreases and/or the thickness of the e-block arm increases. A similar experimental study carried out by Zeng and Hirano [49] also found that the slider's displacements along the out-of-plane and off-track directions, as measured using an LDV, decrease with reverse spinning disks.

6.5 The Effect of Suspension Length

The stiffness of the suspension is much less compared to the stiffness of the e-block arm. This implies that the slider's vibrations are more sensitive to the drag force acting on the suspension than on the e-block arm. Thus reducing the length of the suspension, while keeping the length of the entire actuator constant, should result in a reduction of slider vibrations. This is because the drag force on the suspension – which is flexible – will be reduced, while the drag force on the e-block arm – which is more rigid – will increase. This is similar to the case of the blocking plate as it also reduces the drag force on the suspension while the drag force on the e-block arm increases. For the blocking plate we found that the slider's vibrations are significantly reduced. Thus a reduction in the suspension length should also have a similar effect.

6.6 The Effect of Disk RPM and Slider Radial Position

As shown in chapter 5 the drag force can be expressed as a function of the disk RPM and slider radial position, as follows:

$$Force \propto (RPM)^{9/5}(Radius)^{9/5} \tag{6.1}$$

Thus another way of reducing the drag force and hence the slider vibrations is by reducing the disk RPM and/or by reducing the form factor of the drives. It should be noted that oftentimes such changes are not desirable for other concerns. This is because reducing the disk speed increases the latency (the time taken to rotate the target sector under the head) and thereby reducing the data access rate. Similarly reducing the form factor reduces the recordable area of each disk, which in turn decreases the overall data storage capacity of the drive.

6.7 Conclusions

The effect of several commonly used flow mitigation devices such as a blocking plate, upstream and downstream spoiler are investigated in this chapter. We found that the blocking plate reduces the drag force near the slider and the suspension and hence reduce the in-plane slider vibrations by about 50%. The downstream spoiler significantly reduces the drag force on the e-block arm, but also slightly increases the drag force near the slider and the suspension. Thus there is no significant reduction in in-plane slider vibrations with a downstream spoiler. The upstream spoiler on the other hand increases the in-plane slider vibrations by about 75%.

With reverse spinning disks the HSA is better aligned with the streamlines of the flow. This results in smaller drag forces on the HSA and hence smaller in-plane slider vibrations. The

effect of the suspension length, disk RPM and slider's radial position is also investigated. Reduction in the suspension length results in smaller in-plane slider vibrations. The slider vibrations also scale down with the disk RPM and the form factor of the drive.

6.8 Tables

Table 6.1: The simulations are carried out for the following drive configurations

	Description	Disk RPM
Case 1 (C1)	Generic Configuration (Figure 6.1)	10000 (Normal - counter clockwise)
Case 2 (C2)	Blocking Plate (Figure 6.2 a)	10000 (Normal - counter clockwise)
Case 3 (C3)	Downstream Spoiler (Figure 6.2 b)	10000 (Normal - counter clockwise)
Case 4 (C4)	Upstream Spoiler (Figure 6.2 c)	10000 (Normal - counter clockwise)
Case 5 (C5)	Reverse Spinning Disk	10000 (Reverse - clockwise)

Table 6.2: The dimensions of the three flow mitigation devices (From Kirpekar et al. [48])

All Configurations	Disk Diameter (mm)	76.2
	Disk to Disk Spacing (mm)	2.2
	Disk to Shroud Spacing (mm)	1.0
Blocking Plate (Figure 6.2 a)	Thickness (mm)	0.8
	Angular Dimension (Degrees)	180
	Radial Dimension (mm)	16.25
Downstream Spoiler (Figure 6.2 b)	Thickness (mm)	1.6
	Length (mm)	20.75
	Maximum Width (mm)	2.65
Upstream Spoiler (Figure 6.2 c)	Thickness (mm)	1.4
	Length (mm)	17.5
	Maximum Width (mm)	8.0

Table 6.3: Power consumed by the rotating disks (From Kirpekar et al. [48])

	Description	
Case 1 (C1)	Generic Configuration (Figure 6.1)	3.9W
Case 2 (C2)	Blocking Plate (Figure 6.2 a)	4.6W
Case 3 (C3)	Downstream Spoiler (Figure 6.2 b)	4.4W
Case 4 (C4)	Upstream Spoiler (Figure 6.2 c)	3.95W

6.9 Figures

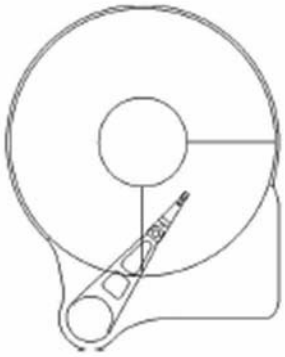

Figure 6.1: Generic hard disk drive model used for air flow simulations (C1) (From Kirpekar et al. [48])

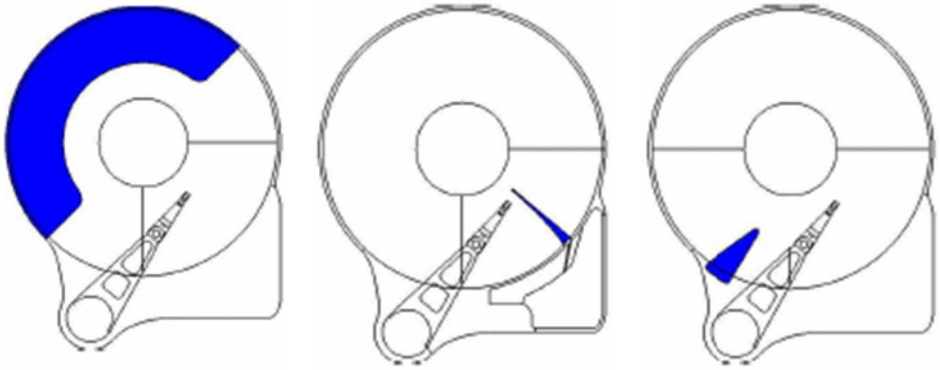

(a) (b) (c)

Figure 6.2: Three flow mitigations devices investigated in this study (a) blocking plate (C2), (b) downstream spoiler (C3) and (d) upstream spoiler (C4) (From Kirpekar et al. [48])

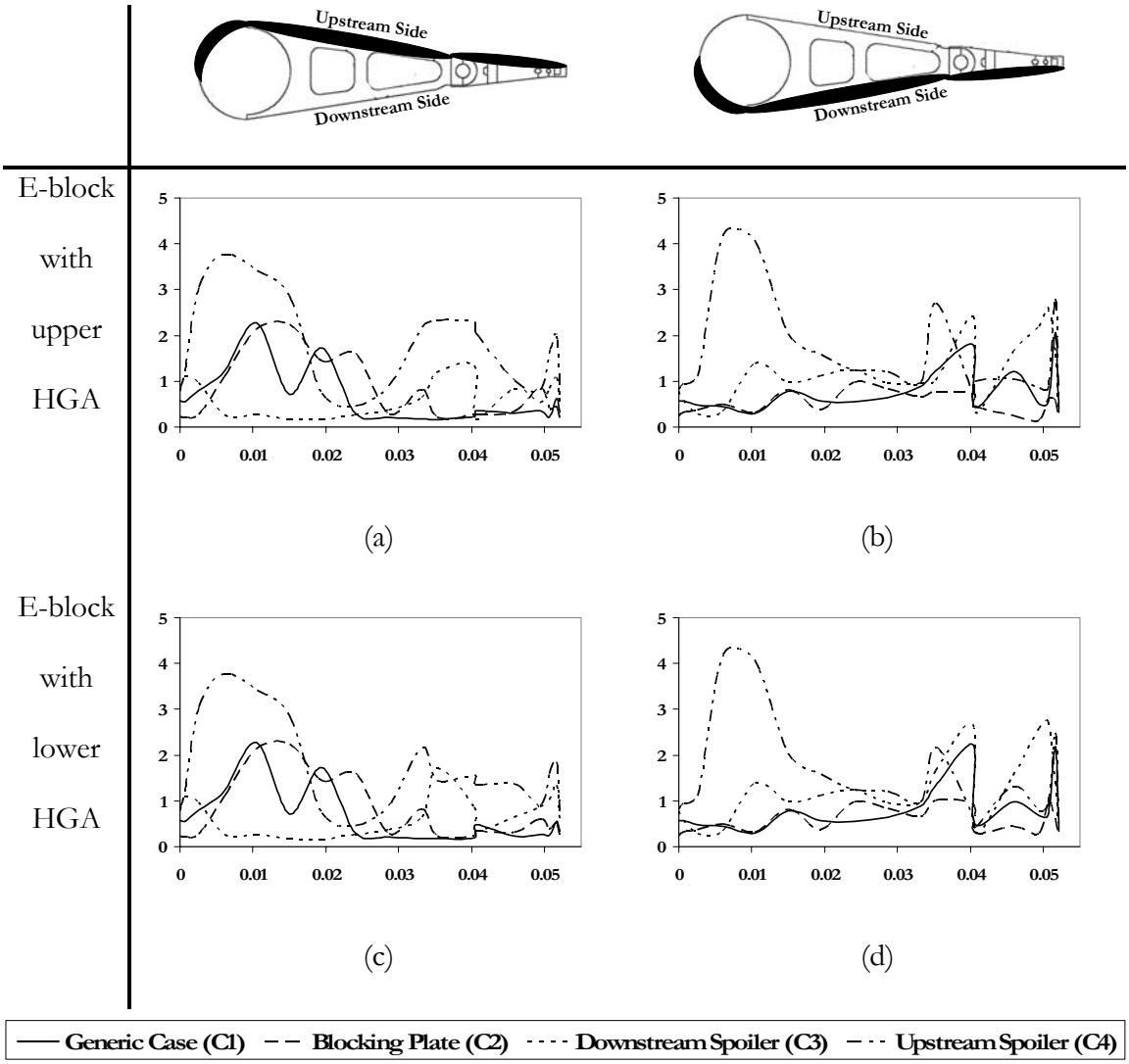

Figure 6.3: Standard deviation of the in-plane velocity fluctuations along the upstream (diagram (a)) and downstream side (diagram (b)) of the E-block and the upper HGA. Diagram (c) and (d) shows the same for the E-block and the lower HGA.

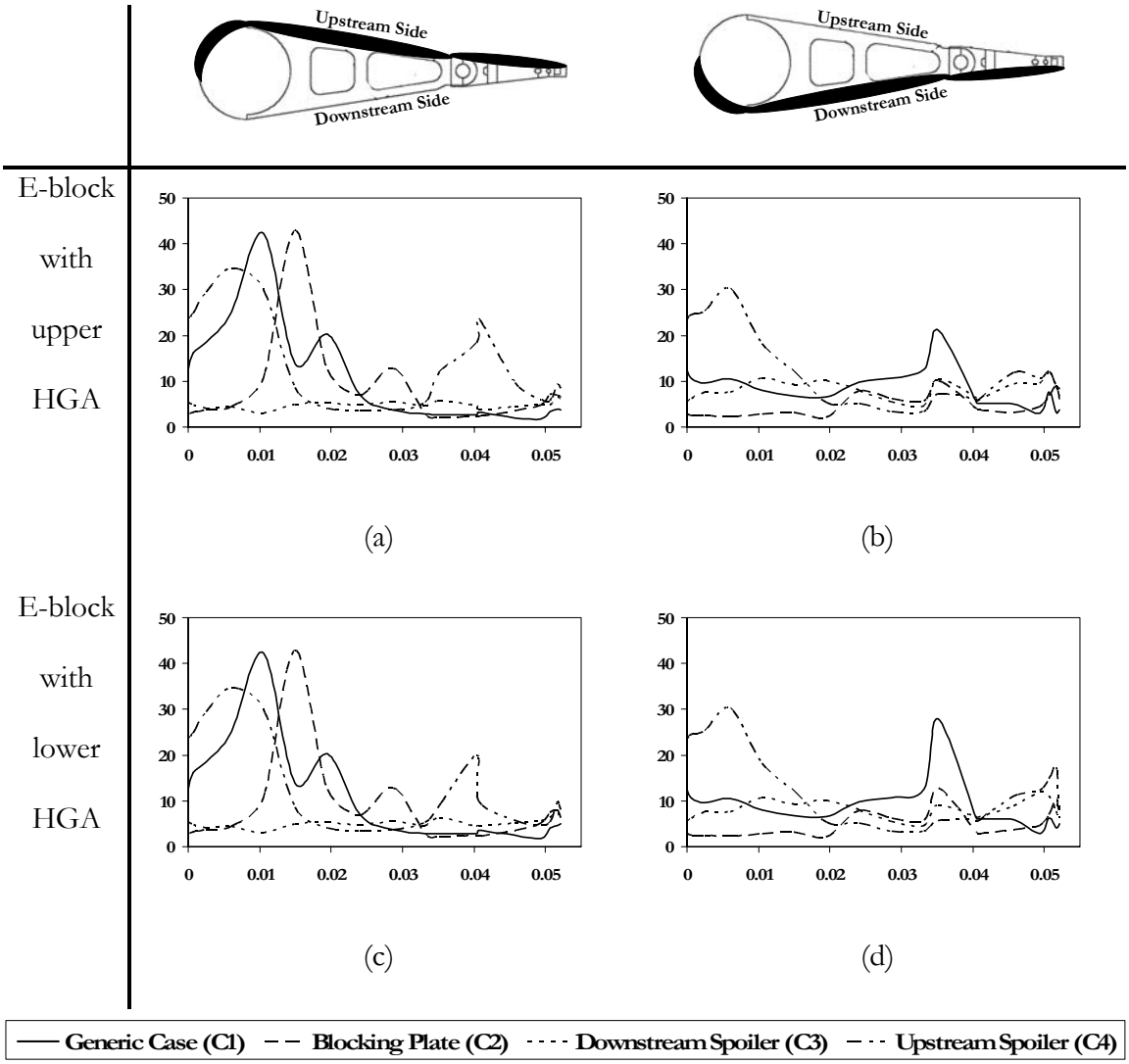

Figure 6.4: Standard deviation of the in-plane pressure fluctuations along the upstream (Diagram (a)) and downstream side (Diagram (b)) of the E-block and the upper HGA. Diagram (c) and (d) shows the same for the E-block and the lower HGA.

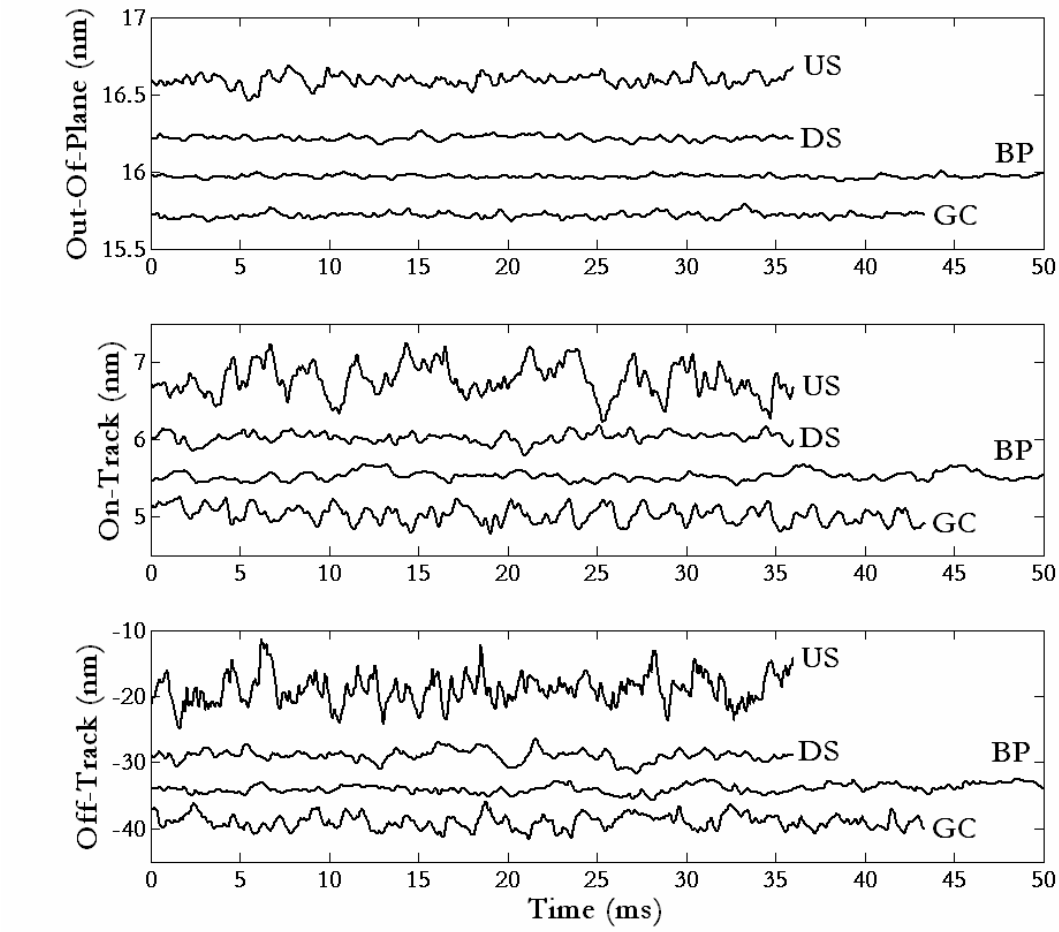

Figure 6.5: Top slider's displacements in the out-of-plane, on-track and off-track directions about arbitrary mean displacements for cases C1, C2, C3 and C4

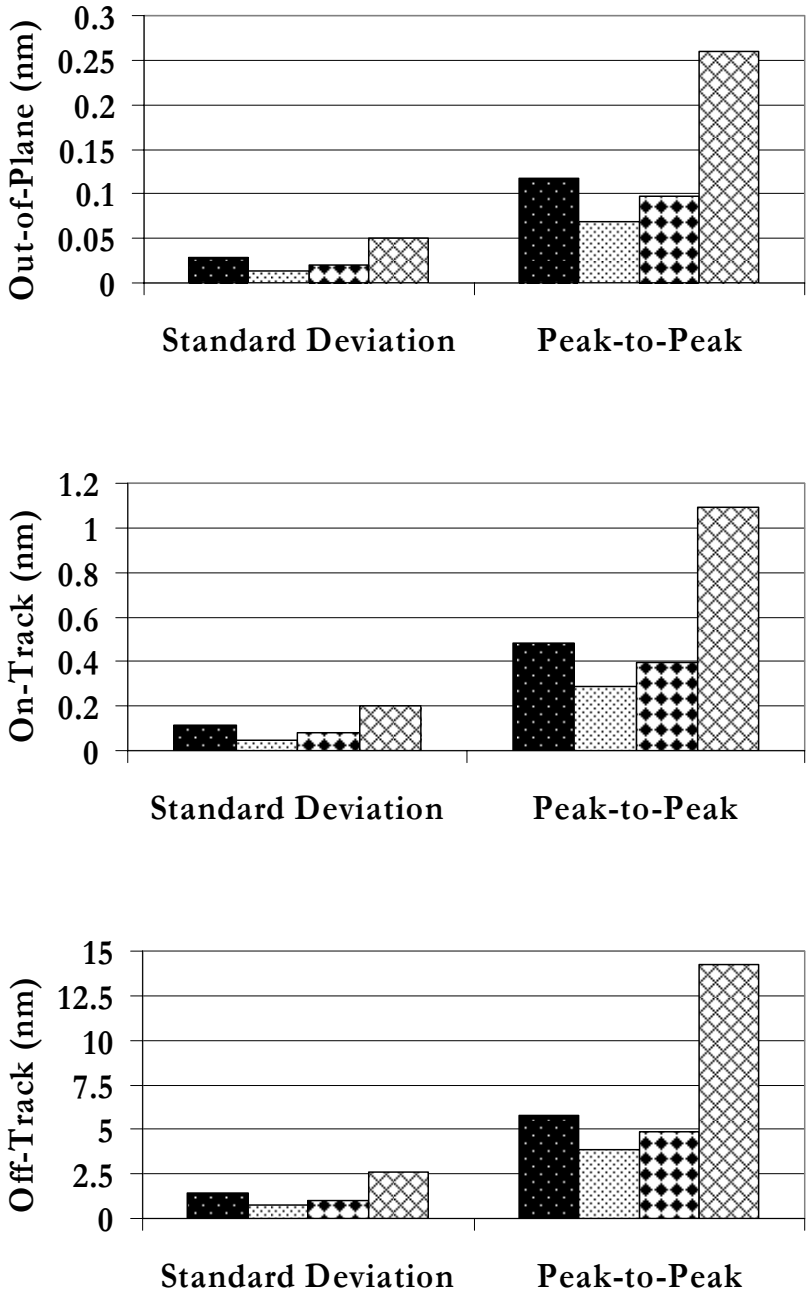

Figure 6.6: Standard deviations and peak-to-peak values of the top slider's displacements in the out-of-plane, on-track and off-track directions for cases C1, C2, C3 and C4

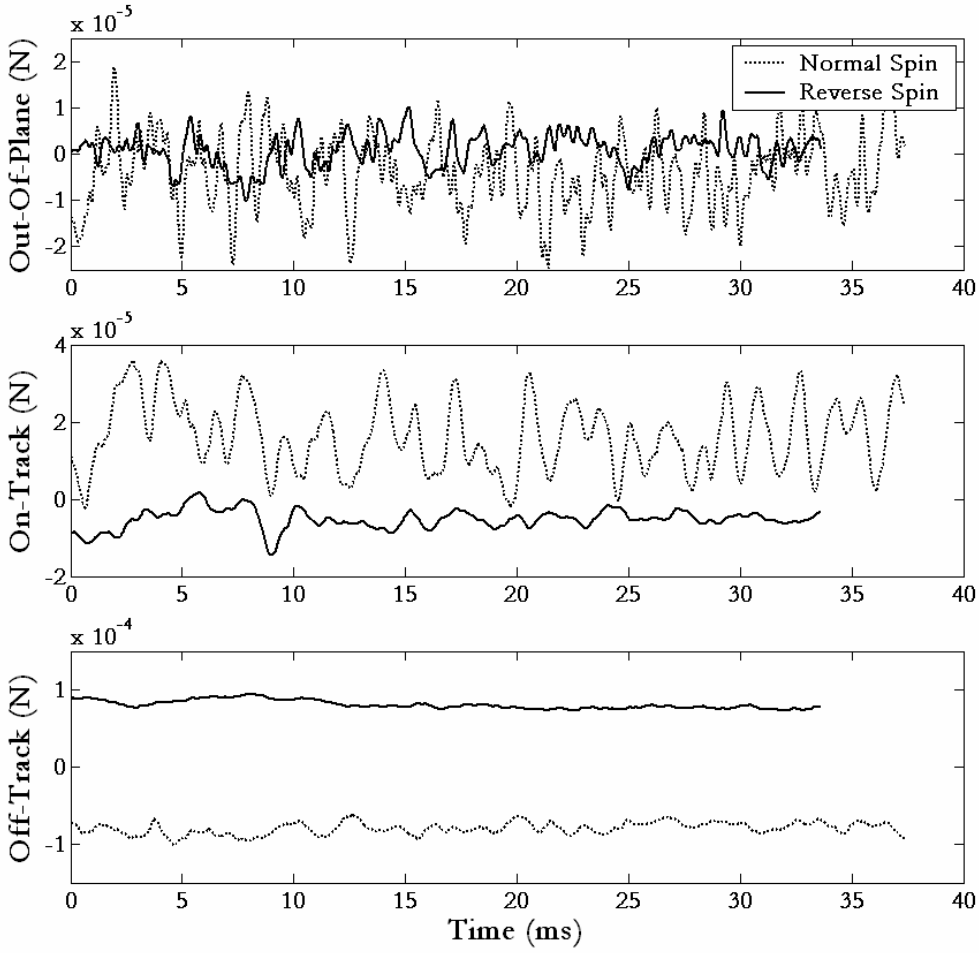

Figure 6.7: A representative plot of the aerodynamic forces acting on the bottom HSA for normal spinning (C1) and reverse spinning (C5) disks

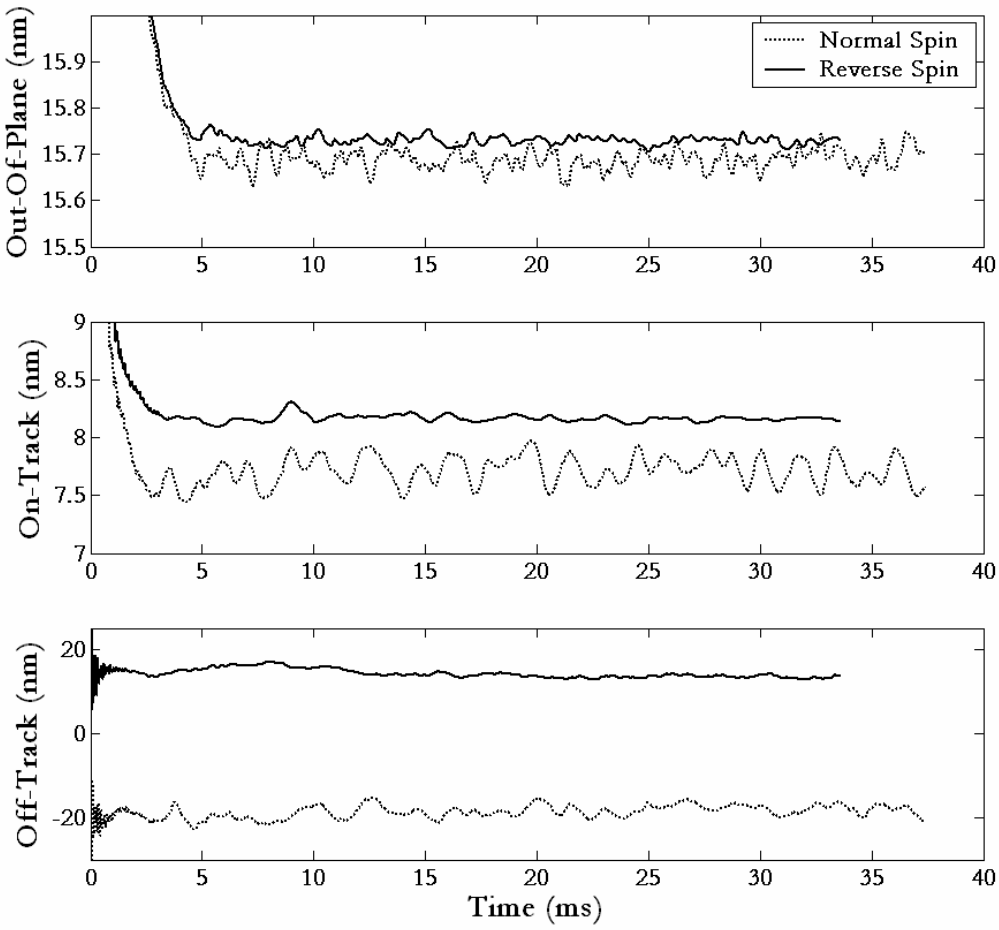

Figure 6.8: Bottom slider's displacements in the out-of-plane, on-track and off-track directions for normal spinning (C1) and reverse spinning (C5) disks

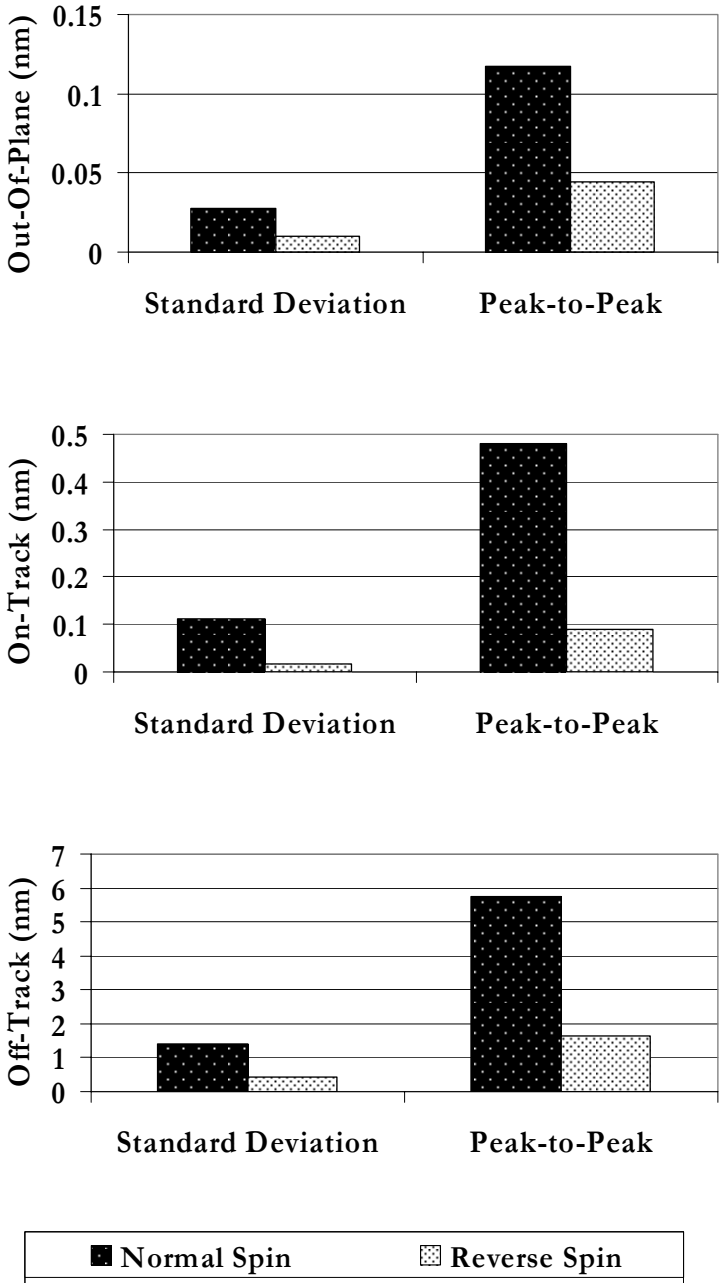

Figure 6.9: Standard deviations and peak-to-peak values of the bottom slider's displacements in the out-of-plane, on-track and off-track directions for normal spinning (C1) and reverse spinning (C5) disks

CHAPTER 7

AIR BEARING SLIDER DYNAMICS AND STABILITY ON BIT PATTERNED MEDIA – A PROMISING STRATEGY FOR ACHIEVING AN AREAL DENSITY OF 50 TBit/in^2 AND BEYOND

7.1 Introduction

Until recently the data storage capacity (measured in Gb/in^2) in hard disk drives has been increasing at a rate of 100% per annum. This astonishing growth rate has been made possible by scaling down the recorded bit size and thus increasing the bit density. Each bit is made up of many grains which act as independent magnetic elements, but under a strong external magnetic field the magnetization of the grains in each bit can be aligned such that the net magnetization of each bit is left or right for longitudinal media (and up or down for perpendicular media).

Recent studies [50],[51],[52] have shown that the transition noise due to irregular or jagged domain of each bit deteriorates the signal to noise ratio (SNR). The SNR can be improved if the magnetization transition from each bit is smooth. This can be achieved by reducing the size of each grain and having many grains in each bit. But the grain size cannot be reduced indefinitely due to the rapid approach of the superparamagnetic limit in the disk drives. This limit is reached when the magnetic energy (K_uV_g) is less than 40-60 times the thermal energy (K_BT), where K_u, V_g, K_B and T are the magnetic anisotropy constant, grain volume, Boltzmann constant and temperature. Under this condition the thermal energy alone can change the magnetization direction of the grain and the magnetization in the grains become thermally unstable. This restricts the minimum size of the thermally stable grain and thus the

maximum achievable recording density on the conventional media to about 0.5-1 Tbit/in^2 [50],[51].

Patterned media has been proposed as one way to overcome this limit on the recording density of the disk drives. By some estimates, patterned media has the potential of increasing the recording densities by two orders of magnitude – up to and beyond 50 Tbit/in^2 [50]. In patterned media each bit consists of a single grain or several exchange coupled grains rather than a collection of magnetically independent grains. Thus each bit has a perfectly distinct boundary and transition noise due to jagged edges is no longer a significant problem in patterned media. And since the bits in patterned media no longer have several grains, the bit density can be increased by two orders of magnitude without reducing the grain size below the one dictated by the superparamagnetic limit.

But one of the main obstacles to patterned media is achieving stable mechanical head-media spacing. The air bearing slider's flying characteristics will be quite different on a pattern media compared to a conventional media depending on the topography of the surface. And the total air bearing stiffness will be compromised as the pattern height increases and/or the percentage area of the total disk covered by the pattern structure decreases, resulting in head media impact and consequent failure. This motivates studying the dynamics of the air bearing slider on patterned media at a higher level of complexity of the mechanical model.

Small sectors of disks with discrete tracks or bit patterns are shown in Figure 7.1. For bit patterned media (BPM), X_{wl} and Y_{wl} are the pattern wavelengths in X and Y directions, respectively, and X_{lt} and Y_{lt} are the pattern lengths in the X and Y directions. Similarly for

discrete track media (DTM), the pattern wavelength and pattern length in Y direction are Y_{wl} and Y_{lt}. The fraction of the total area covered by the pattern is defined as the area ratio (AR) in this chapter. Thus for BPM and DTM the area ratio is $X_{lt}Y_{lt}/X_{wl}Y_{wl}$ and Y_{lt}/Y_{wl}, respectively. The ratios $X_{lt}/Y_{lt} = X_{wl}/Y_{wl}$ are fixed at 2.5 in this investigation. A dimensionless pattern height (PH) is defined as the actual pattern height divided by MFH_0, where MFH_0 is the minimum mechanical spacing between the slider and the conventional disk (i.e. one without patterned features).

7.2 Modeling Techniques

It has been estimated that for 1 Tbit/in^2 recording density, the pattern wavelength should be 25 nm and the feature size should be 18 nm in the down-track direction [51]. The wavelength of these features is much smaller than the air bearing slider's dimension. Several numerical techniques such as direct simulation, averaging and homogenization can be used to solve the generalized Reynolds equation (7.1) in order to study the effect of these features on the slider's stability.

$$\frac{\partial}{\partial X}\left(QPH^3\frac{\partial P}{\partial X}-\Lambda_x PH\right)+\frac{\partial}{\partial Y}\left(QPH^3\frac{\partial P}{\partial Y}-\Lambda_y PH\right)=0 \tag{7.1}$$

Here P and H are the dimensionless load pressure and spacing between the slider and the disk. Λ_x and Λ_y are the bearing numbers in the X and Y directions. Q is the flow factor assuming the Fukui and Kaneko correction [28],[29] and K_n is the Knudsen number.

Direct simulation technique is mathematically the simplest of the three techniques, but computationally the most expensive one. Using this technique requires an extremely fine grid so that even these small wavelength features are captured really well. The length and width of a pico slider are 1.25 mm and 1 mm, respectively. With 25 nm wavelength features in the

off-track and down-track directions, the wavenumber per slider length and width will be 50,000 and 40,000, respectively. This dictates that for direct simulations the number of nodes along the length and width of the slider should be 500,000 or more. As a result the total number of nodes per case will be ~ $(500{,}000)^2$ and air bearing calculations for such a huge system will take weeks on office computers. Thus alternative mathematical techniques such as averaging and homogenization have been explored for air bearing calculations.

The averaging technique was first proposed by Mitsuya et al. [53] for air bearing calculations. Later Mitsuya et al. [54] derived a simplified averaged Reynolds equation using the Fukui and Kaneko correction model. According to this model the average film thickness for a longitudinal pattern can be expressed as $\tilde{H}^m = \overline{H^m}\ \forall m \in \{1,2,3\}$, where $\bar{(\,)}$ denotes the arithmetic averaging. Similarly, the average film thickness for a transverse pattern can be expressed as $\tilde{H}^m = \overline{\overline{H^m}}$, where $\overline{\overline{H^1}} = \overline{H^{-2}}/\overline{H^{-3}},\ \overline{\overline{H^2}} = 1/\overline{H^{-2}}, and\ \overline{\overline{H^3}} = 1/\overline{H^{-3}}$. Thus for a rough surface with a combination of longitudinal and transverse patterns, the mixed averaged film thickness can be expressed as

$$\tilde{H}_i^m = \alpha_i \overline{H_i^m} + (1-\alpha_i)\overline{\overline{H_i^m}}\ \forall m \in \{1,2,3\} and\ i \in \{X,Y\} \tag{7.2}$$

Here the coefficient α_i is the mixing ratio of the longitudinal and transverse patterns. Thus α_i = 1 for a longitudinal pattern and α_i = 0 for a transverse pattern.

Using these values of the mixed averaged film thickness, one can express the averaged Reynolds equation with the Fukui and Kaneko correction as

$$\frac{\partial}{\partial X}\left(\tilde{Q}_x \tilde{H}_x^3 \overline{P}\frac{\partial \overline{P}}{\partial X} - \Lambda_x \overline{P}\tilde{H}_x\right) + \frac{\partial}{\partial Y}\left(\tilde{Q}_y \tilde{H}_y^3 \overline{P}\frac{\partial \overline{P}}{\partial X} - \Lambda_y \overline{P}\tilde{H}_y\right) = 0 \tag{7.3}$$

Here $\overline{P}\ and\ \tilde{H}^m$ are the averaged dimensionless load pressure and mixed averaged spacing

between the head and the disk. $\tilde{Q}_x$ *and* $\tilde{Q}_y$ are the averaged flow factor in the X and Y directions assuming the Fukui and Kaneko correction [28],[29]. Here $\alpha_x = 1$ and $\alpha_y = 0$ for a longitudinal pattern and $\alpha_x = 0$ and $\alpha_y = 1$ for a transverse pattern. For a patterned surface with a combination of longitudinal and transverse patterns the values of α_x and α_y can be selected based on table 2 in [53].

The advantage of using an averaging technique is that the number of nodes required for solving the Reynolds equation can be as few as $(300)^2$ compared to $(500{,}000)^2$ nodes required with the direct simulation technique. This represents a huge savings in the computational cost. Mitsuya et al. [53] also compared the solution of the averaged Reynolds equation over patterned surfaces – longitudinal, transverse and checkerboard features – with experiments, and they found very good agreements.

More recently Jai et al. [55] proposed an alternate way of modeling slider dynamics over a patterned disk using a homogenization technique based on a multi-scale approach. Using this technique the air bearing problem is divided into two parts: (a) the global problem, which is very similar to the Reynolds equation that relates the mechanical spacing between the slider and the disk to the pressure distribution between them, and (b) a local problem, which solves for the periodic functions ω and χ used in the global problem.

In order to derive the homogenized Reynolds equation we divided the mechanical spacing (H) between the slider and the disk into two parts as follows

$$H(X,Y) = H_0(X,Y) + H_1\left(\frac{X}{\gamma}, \frac{Y}{\gamma}\right) \tag{7.4}$$

Here H_0 accounts for the mechanical spacing due to the air bearing shape - crown, camber, twist, roll, pitch etc., and H_1 accounts for the mechanical spacing due to the pattern shape and the dimensionless pattern wavelength is assumed to be γ. As it is defined, the function H_1 is a periodic function.

The pressure distribution between the slider and the disk can be expressed as a function of X, Y, ξ_x and ξ_y

$$P(X,Y) = P_0(X,Y) + \gamma P_1(X,Y,\xi_x,\xi_y) + \gamma^2 P_2(X,Y,\xi_x,\xi_y) + \ldots \tag{7.5}$$

where $\xi = (\xi_x,\xi_y) = (X/\gamma, Y/\gamma)$ and P_1, P_2 etc. are periodic functions of the variables ξ_x, ξ_y. Substitution of equation (7.5) into equation (7.1) gives, after some mathematical manipulations as detailed in [55],[56], a global problem and a local problem. The global problem is similar to the Reynolds equation and is expressed as

$$\frac{\partial}{\partial X}\left(\hat{Q}_{xx}\frac{\partial P_0}{\partial X} + \hat{Q}_{xy}\frac{\partial P_0}{\partial Y} - \hat{\Lambda}_x P_0\right) + \frac{\partial}{\partial Y}\left(\hat{Q}_{yx}\frac{\partial P_0}{\partial X} + \hat{Q}_{yy}\frac{\partial P_0}{\partial Y} - \hat{\Lambda}_y P_0\right) = 0 \tag{7.6}$$

where the matrix $\hat{Q}$ is given by

$$\hat{Q} = \begin{bmatrix} \int_\Theta QPH^3\left(\frac{\partial \omega_1}{\partial \xi_1}+1\right)d\xi & \int_\Theta QPH^3\left(\frac{\partial \omega_2}{\partial \xi_1}\right)d\xi \\ \int_\Theta QPH^3\left(\frac{\partial \omega_1}{\partial \xi_2}\right)d\xi & \int_\Theta QPH^3\left(\frac{\partial \omega_2}{\partial \xi_2}+1\right)d\xi \end{bmatrix} \tag{7.7}$$

And the vector $\hat{\Lambda}$ is given by

$$\hat{\Lambda} = \begin{bmatrix} \int_\Theta \left(\Lambda_x\left(H + QPH^3\left(\frac{\partial \chi_1}{\partial \xi_1}\right)\right) + \Lambda_y\left(QPH^3\left(\frac{\partial \chi_2}{\partial \xi_1}\right)\right)\right)d\xi \\ \int_\Theta \left(\Lambda_x\left(QPH^3\left(\frac{\partial \chi_1}{\partial \xi_2}\right)\right) + \Lambda_y\left(H + QPH^3\left(\frac{\partial \chi_2}{\partial \xi_2}\right)\right)\right)d\xi \end{bmatrix} \tag{7.8}$$

Here Q is the flow factor assuming the Fukui and Kaneko correction [28],[29] and the integration domain Θ is a unit cell $(\xi_x,\xi_y) = [0,1]X[0,1]$ that includes one entire pattern feature. The functions ω_1, ω_2, χ_1 and χ_2 are 1-periodic solutions of the following local

problems defined on the unit cell Θ

$$\frac{\partial}{\partial\xi_1}\left(Q_0P_0H^3\left(\frac{\partial\omega_1}{\partial\xi_1}+1\right)\right)+\frac{\partial}{\partial\xi_2}\left(Q_0P_0H^3\left(\frac{\partial\omega_1}{\partial\xi_2}\right)\right)=0$$
$$\frac{\partial}{\partial\xi_1}\left(Q_0P_0H^3\left(\frac{\partial\omega_2}{\partial\xi_1}\right)\right)+\frac{\partial}{\partial\xi_2}\left(Q_0P_0H^3\left(\frac{\partial\omega_2}{\partial\xi_2}+1\right)\right)=0 \tag{7.9}$$

and,

$$\frac{\partial}{\partial\xi_1}\left(Q_0P_0H^3\left(\frac{\partial\chi_1}{\partial\xi_1}\right)+H\right)+\frac{\partial}{\partial\xi_2}\left(Q_0P_0H^3\left(\frac{\partial\chi_1}{\partial\xi_2}\right)\right)=0$$
$$\frac{\partial}{\partial\xi_1}\left(Q_0P_0H^3\left(\frac{\partial\chi_2}{\partial\xi_1}\right)\right)+\frac{\partial}{\partial\xi_2}\left(Q_0P_0H^3\left(\frac{\partial\chi_2}{\partial\xi_2}\right)+H\right)=0 \tag{7.10}$$

Here Q_0 is a function of P_0 and H.

In order to solve the homogenized Reynolds equation, we need no more than $(300)^2$ nodes, but homogenized solutions are computationally more expensive than the averaged solutions. This is because the local problem has to be solved at each of the $(300)^2$ nodes, although the size of the local problem is much smaller than the global problem as $(10)^2$ nodes are more than sufficient for the local problem. More recently Buscaglia and Jai [56],[57] have proposed a way to significantly reduce the computational cost by approximating the solution of the local problem using a Taylor series expansion. For this study we computed the exact solution of the local problem at each node instead of using such an approximate solution.

One should also observe that for one-dimensional pattern shapes – such as with only longitudinal or transverse patterns – there exists an analytic solution of the local problem. For example with longitudinal patterns – such as over a discrete track media – $\hat{Q}_{xy}=\hat{Q}_{yx}=\omega_1=\chi_1=0$. Using this in equations (7.9) and (7.10) we reduce the matrix $\hat{Q}$ to

$$\hat{Q} = \begin{bmatrix} \tilde{Q}_0 P_0 \overline{H^3} & 0 \\ 0 & \tilde{Q}_0 P_0 \dfrac{1}{\overline{H^{-3}}} \end{bmatrix} \tag{7.11}$$

and the vector $\hat{\Lambda}$ reduces to

$$\hat{\Lambda} = \begin{bmatrix} \Lambda_x \overline{H} \\ \Lambda_y \overline{H^{-2}} \Big/ \overline{H^{-3}} \end{bmatrix} \tag{7.12}$$

Thus the homogenized Reynolds equation for longitudinal pattern is obtained by substituting equations (7.11) and (7.12) into equation (7.6). It is interesting to observe that two equations – averaged (equation (7.3)) and homogenized (equation (7.6)) are similar over a longitudinal pattern. A similar calculation for a transverse pattern also indicates that the two equations are similar. Thus it is only for mixed patterns – with both transverse and longitudinal features – that the two models differ. But still we found that for mixed patterns like checkerboard patterns, the numerical results calculated using averaged and homogenized equations are extremely close, which is in agreement with a similar investigation carried out by Jai et al. [56].

Mitsuya et al. [53] also compared the numerical solution of the averaged Reynolds equation with the experimental results of the slider's flying characteristics over longitudinal, transverse and mixed pattern features on the disk. The two results are in good agreement and this indicates that the Reynolds equation with averaging or homogenization is still an acceptable way to model the slider's dynamics over patterned media. These comparisons are reported for values of PH < 0.5. More recently, Talke et al. [58] have demonstrated that Reynolds equation is valid over discrete track media (DTM) even for PH > 0.5.

In our investigation the numerical solutions are carried out using both the averaging and

homogenization techniques to study a slider's flying characteristics over DTM and bit patterned media (BPM). Both the averaged and the homogenized Reynolds equations are solved using Patankar's finite volume technique [30]. Detailed discussions on other numerical schemes that can be used to solve the homogenized Reynolds equation can be found in [56],[59],[60]. An algorithm for homogenization of the transient Reynolds equation can be found in [61].

We found that the two solutions – averaged and homogenized – are extremely close for both DTM and BPM when the pattern wavelength is much smaller than the dimension of the slider and PH < 1.0. However at higher pattern heights the solutions obtained using the two techniques begin to differ slightly over BPM. The results presented in this chapter are calculated using the homogenization technique because we believe that the homogenization technique is more accurate in the way the two-dimensional patterns – with any shape and alignment – are included in the model. Nonetheless, for BPM with small pattern heights the use of the averaging technique could sometimes be preferable because the solutions of the averaged Reynolds equation are computationally less expensive than the solutions of the homogenized Reynolds equation. A more detailed comparison of the direct simulation, averaging and the homogenization technique can be found in [62],[63].

The hard disk drive model is the same as the one described in chapter 2. It consists of a finite element HSA and disk model together with the air bearing model described by the homogenized Reynolds equation. In addition it also includes the Lennard-Jones potential model, a parallel plate capacitance model and the elastic-plastic model to calculate the intermolecular forces, electrostatic forces and contact forces at the HDI.

7.3 Slider's Flying Characteristics without Considering the Effect of the Intermolecular Forces

The minimum mechanical spacing between the slider shown in Figure 7.2 and the conventional disk is 2.99 nm (MFH_0). The displacements along the other 5 degrees of freedom are shown in Table 7.1. At this state the total Z force – air bearing – acting on the slider is 0.525 gm which is balanced by the suspension pre load. If this slider is flown on a patterned media at a mechanical spacing of 2.99 nm from the top of the patterned surface the total air bearing force acting on the slider will be reduced (assuming that the change in the pitch and the roll angle is very small). This is because at the grooves the mechanical spacing between the slider and the disk is larger and thus the air bearing pressure – which is inversely proportional to the mechanical spacing – is reduced. This causes the mechanical spacing between the slider and the disk to reduce until the total air bearing force is sufficient to balance the suspension pre-load and the intermolecular force. Using this understanding we should expect the drop in mechanical spacing between the slider and the disk to be large when the area ratio is small and/or when the pattern height is large.

Figure 7.3 shows the plots of the minimum flying height from the top of the patterned surface (MFH_{Top}) as a function of area ratio (AR) for several values of the non-dimensional pattern heights (PH). The effect of intermolecular forces is not considered in this case and hence the non-dimensional pattern height is the pattern height divided by the minimum mechanical spacing between the slider and the disk on a conventional media w/o including the effect of the intermolecular forces (MFH_0). We observe that for large area ratios – $AR \approx 1^-$ – the MFH_{Top} is the same irrespective of the pattern height. This is because for large area

ratios the percentage of the total area covered by the grooves is small and thus the reduction in the air bearing pressure and hence the mechanical spacing between the slider and the disk is small. We also observes that for small area ratios – AR ≈ 0^+ – the drop in the mechanical spacing is large because in this case almost the entire suspension pre-load is supported by the air bearing pressure from the grooves. It is interesting to note that at AR ≈ 0^+, MFH_{Top} is approximately MFH_0*(1 – PH).

Also the drop in the minimum mechanical spacing at AR ≈ 0^+ is MFH_0*PH. Thus we see that for small pattern heights the drop in the minimum mechanical spacing is small as the area ratio changes from 1 to 0. But as the pattern height increases the drop in the mechanical spacing becomes significant. And for PH = 1 and AR = 0^+, the MFH_{Top} reduces to zero and the slider comes in contact with the pattern features. This is considered to be a HDI failure in this investigation. We also observe that for higher pattern heights the slider comes in contact with the pattern features even at larger area ratios and this results in HDI failure. Thus there is a maximum pattern height corresponding to each area ratio, beyond which the HDI will fail.

Figure 7.4 is based on the same results as in Figure 7.3 but shows the plots of the minimum flying height from the mean of the patterned surface (MFH_{Mean}) as a function of the area ratio (AR) for several values of the non-dimensional pattern heights (PH). We find that for small values of the pattern heights the deviation of MFH_{Mean} from MFH_0 is small. But as the pattern height increases the MFH_{Mean} is greater than MFH_0 especially for area ratios between 0.1 and 0.9. Here we should point out that for small pattern heights (PH < 0.25) the deviation from MFH_0 can be positive or negative, but for higher pattern heights the

deviation is always positive. For this particular slider design it so happens that the deviations from MFH_0 are positive for small pattern heights.

The results in Figs 3 and 4 ignore the effect of the intermolecular forces at the HDI. These results are useful in understanding the basics of the slider dynamics on the patterned media. But the slider dynamics is quite different when the effect of these forces is taken into consideration at the HDI.

7.4 Slider's Flying Characteristics Considering the Effect of the Intermolecular Forces

Figure 7.5 shows the plots of the minimum flying height from the top of the patterned surface (MFH_{Top}) as a function of area ratio (AR) for two values of the non-dimensional pattern heights (PH). The effect of intermolecular forces is considered in this case and hence the non-dimensional pattern height is the pattern height divided by the minimum mechanical spacing between the slider and the disk on a conventional media including the effect of the intermolecular forces (MFH_0).

In this case we observe three equilibrium points for each value of AR and PH instead of just one equilibrium that is observed in the previous case where the effect of intermolecular forces is ignored. In order to understand the stability of these three equilibrium points we calculated the eigenvalues of the linearized system matrix. We found that for two of these three equilibrium points – corresponding to the maximum and minimum values of MFH_{Top} – all eigenvalues have negative real part. This implies that these two equilibriums are stable. However the middle equilibrium point has one or more eigenvalues with positive real part,

and hence it is an unstable equilibrium point. The stable and unstable equilibrium points are shown in Figure 7.5.

An equilibrium point is considered unstable if the slider moves away from the equilibrium as a result of small disturbances. Thus experimentally an unstable equilibrium is never attainable. Moreover the second stable equilibrium is extremely close to the pattern features (< 0.3 nm). This equilibrium point is also experimentally unattainable because the peak-to-peak surface roughness is more than 0.3 nm even for the super smooth patterned disks expected to be used in future hard disk drives. And thus at such small mechanical spacing the slider is considered to be in contact with the disk.

Figure 7.6 shows the plots of the minimum flying height from the top of the patterned surface (MFH_{Top}) as a function of area ratio (AR) for several values of the non-dimensional pattern heights (PH). The effect of intermolecular forces is included in this case. We observe that for large area ratios – AR $\approx 1^-$ – the MFH_{Top} is the same irrespective of the pattern height. This is because for large area ratios the percentage of the total area covered by the grooves is small and thus the reduction in air bearing pressure and hence the reduction in the mechanical spacing between the slider and the disk is small. We also observes that for small area ratios – AR $\approx 0^+$ – the drop in the mechanical spacing is large because in this case almost the entire suspension pre-load and the intermolecular force is supported by the air bearing pressure from the grooves. It is interesting to note that at AR $\approx 0^+$ the value of MFH_{Top} is less than $MFH_0*(1 - PH)$. This is because the intermolecular forces are attractive and they reduce the mechanical spacing between the slider and the disk. The magnitude of these forces is inversely proportional to the mechanical spacing so the reduction in

mechanical spacing is large for low flying sliders. As a result the slider comes in contact with the pattern features at PH < 1 when the AR ≈ 0^+.

Here also we see that for small pattern heights the drop in the minimum mechanical spacing is small as the area ratio changes from 1 to 0. But as the pattern height increases the drop in the mechanical spacing becomes significant. For PH = 0.82 and AR = 0^+, the MFH_{Top} reduces to zero approximately (or more precisely the lowest equilibrium value) and the slider comes in contact with the pattern features. This is considered as a HDI failure in this investigation. We also observe that for higher pattern heights the slider comes in contact with the pattern features even at larger area ratios, and this results in HDI failure. Thus, here again, there is a maximum pattern height corresponding to each area ratio, beyond which the HDI fails.

So far we have only looked at the effect of patterned disk on the slider's vertical displacement. The effect of pattern features on the sliders other five degrees of freedom – on-track displacement, down-track displacement, pitch, roll and yaw – are plotted in Figure 7.7. We should note that the mean value of the slider's displacement on the conventional media in all these five degrees of freedom is the one corresponding to AR = 1. We observe that for large area ratios (≈1^-) or small ratios (≈0^+) the change in the mean values of the five degrees of freedom from the corresponding value on the conventional disk is insignificant. We also observe that relatively larger changes occur for area ratios between 0.1 and 0.9. Similarly, for small pattern heights the changes in the mean values of the five degrees of freedom from the corresponding values on the conventional disk are insignificant and the changes are relatively larger for higher pattern heights. Nonetheless, we observe that if PH <

1 the changes in the mean values of the sliders displacements along the on-track, down-track, pitch, roll and yaw directions are very small.

7.5 Fixed Attitude Air Bearing Stiffness

The minimum mechanical spacing between the slider shown in Figure 7.2 and the conventional disk is 2.63 nm (MFH_0) when the effect of intermolecular forces is taken into consideration. The displacements along the other 5 degrees of freedom are shown in Table 7.1. At this state the total Z force – air bearing and intermolecular force – acting on the slider is 0.525 gm which is balanced by the suspension pre load. Figure 7.8 shows the plot of the total Z force on the same slider flying over patterned media as a function of area ratio and pattern height. For this plot the minimum mechanical spacing between the slider and the top of the patterned surface is maintained constant at 2.63 nm and the displacements along all other 5 degrees of freedom are also maintained at the fixed values listed in Table 7.1 for all area ratios and pattern heights. We found that as the pattern height increases and/or as the area ratio decreases the total force in the Z direction reduces. This is because at the grooves the mechanical spacing between the slider and the disk is larger and thus the air bearing force – which is inversely proportional to the mechanical spacing – is smaller. As a result the total Z force decreases.

The stability of the slider at the HDI depends on the stiffnesses along the 6 directions – 3 translational (Z, off-track and down-track) and 3 rotational (pitch, roll and yaw). But since the off-track, down-track and yaw stiffnesses are not affected as much as the Z, pitch and roll stiffness, we will focus on the change in the Z, pitch and roll stiffnesses on a patterned media. Figure 7.9 shows plots of the Z, pitch and roll stiffnesses as functions of the area

ratio and the pattern height. We observe that as the percentage area of the grooves increases and/or as the groove depth increases the Z, pitch and roll stiffnesses decrease, resulting in a less stable HDI.

These calculations indicate that for a desired flying attitude (height, pitch and roll angles) the Z, pitch and roll stiffnesses are maximum on a conventional media, and they decrease on a patterned media as the area ratio decreases and/or as the pattern height increases. They also imply that if the grooves of the patterned media are filled, with something such as a bonded lubricant or DLC overcoat, then geometrically the HDI on a patterned media will be similar to the HDI on a conventional media. This will increase the Z, pitch and roll stiffnesses and improve the dynamic stability of the HDI.

7.6 Air Bearing Stiffness for Slider Flying on a Patterned Media

In the last section we evaluated the change in the Z, pitch and roll stiffnesses while maintaining the flying attitude between the slider and the top of the disk constant. That analysis informed us about the change in the stiffness values over patterned media. But in reality when the slider is flying over a patterned media its minimum mechanical spacing from the top of the patterned surface will change from the value for conventional media as shown in Figure 7.6.

Figure 7.10 shows the HDI stiffness chart as a function of the area ratio and the pattern height. We observe that for large values of the area ratio and small pattern heights the Z, pitch and roll stiffnesses on a patterned media are within ±5% of the Z, pitch and roll stiffnesses on a conventional media. This region is indicated by '$STIFF(Z,P,R)_{PM} \approx$

STIFF(Z,P,R)$_{CM}$' in the HDI stiffness chart. This is because within this region if the area ratio and/or the pattern height changes the mechanical spacing between the slider and the disk also changes to maintain the same Z force and the same Z, pitch and roll stiffnesses.

For small values of the area ratio and large pattern heights the mechanical spacing between the slider and the disk reduces drastically as shown in Figure 7.5. At such low spacing the magnitude of the intermolecular force is very strong and this causes the total stiffness in one or more directions to become negative. This may result in an unstable HDI. This region is indicated by '*STIFF(Z,P,R)$_{PM}$ < 0*' in the HDI stiffness chart.

The region between '*STIFF(Z,P,R)$_{PM}$ ≈ STIFF(Z,P,R)$_{CM}$*' and '*STIFF(Z,P,R)$_{PM}$ < 0*' in the HDI stiffness chart is the transition region where the Z, pitch and roll stiffnesses drastically reduce. This is the region where the effect of intermolecular force becomes increasingly significant due to the reduction in the mechanical spacing between the slider and the disk.

These calculations indicate that the mechanical spacing between the slider and the disk reduces as the area ratio decreases and/or the pattern height increases. As a result the magnitude of the intermolecular forces increase which causes the stiffness in one or more directions to become negative. This may result in an HDI failure. These results also implies that a planarized patterned media will help maintain high Z, pitch and roll stiffnesses and improve the dynamic stability of the HDI.

7.7 Conclusions

In this chapter we presented a study of the slider's flying characteristics on patterned media.

Both the averaged and homogenized Reynolds equations are used to model the relationship between the mechanical spacing and the pressure at the HDI. We found that the averaged and homogenized Reynolds equations are good approximations of the flow, especially for small pattern heights. We found that the slider's vertical displacements change significantly over patterned media, but the changes in the other five degrees of freedom – down-track and off-track displacements and the pitch, roll and yaw angles – are small. In order to comment on the stability of the HDI over patterned media total stiffness is calculated along all six degrees of freedom. We found that the Z, pitch and roll stiffnesses reduce when the slider is flying over a patterned media as compared to when it is flying over a conventional media. This reduces the stability of the HDI and may also result in HDI failure. Our calculations indicate that if the HDI on a patterned media is planarized to make it topographically similar to the HDI on a conventional media then the stability of the HDI can be restored to the same level as that on a conventional media. The planarization can be done by filling the grooves with bonded lubricant or DLC overcoat.

7.8 Tables

Table 7.1: The slider's steady displacements on a conventional media with and without considering the effect of the intermolecular forces (IMF)

	w/o IMF	w/ IMF
Min Flying Ht (MFH_0) (nm)	2.99	2.63
Down-Track (nm)	33.34	33.68
Off-Track (nm)	3.24	3.31
Pitch (μrad)	215.69	216.54
Roll (μrad)	-7.09	-7.14
Yaw (μrad)	-0.59	-0.56

7.9 Figures

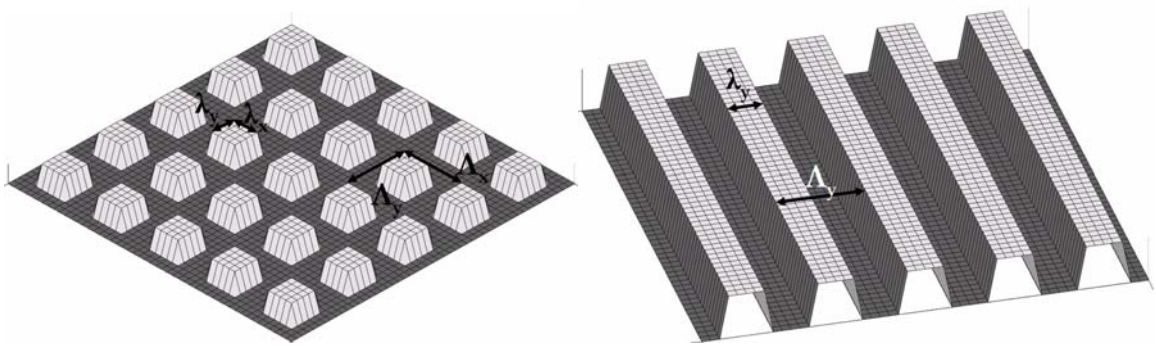

Figure 7.1: (a) Bit Patterned Media and (b) Discrete Track Media

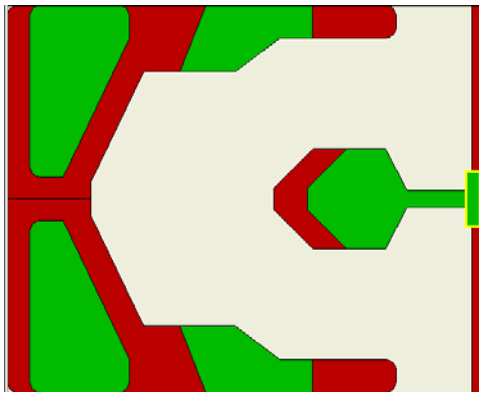

Figure 7.2: Femto slider design used in this investigation. The suspension pre load is 0.525 gm. The crown and camber are 18 nm and 2.5 nm, respectively.

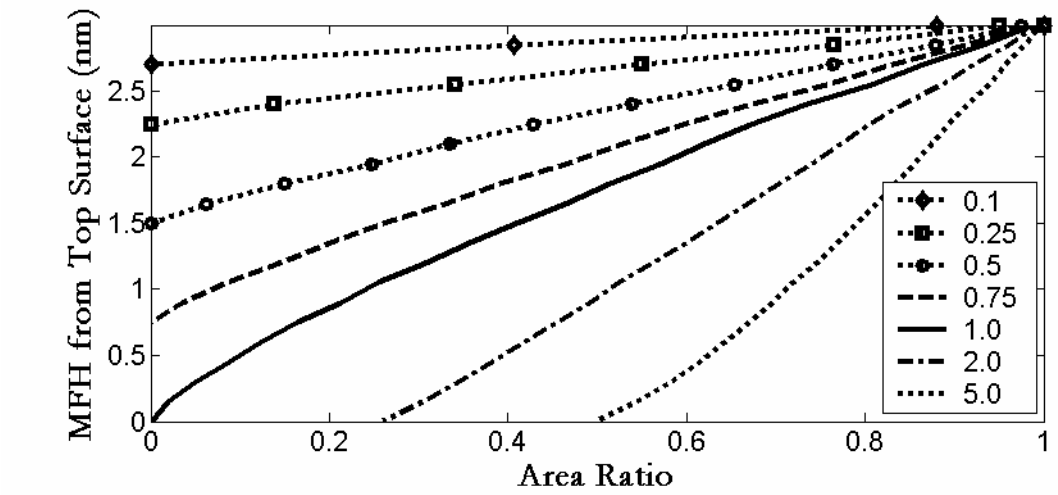

Figure 7.3: Minimum mechanical spacing of the slider measured from the top surface of the patterned media without including the effect of intermolecular forces.

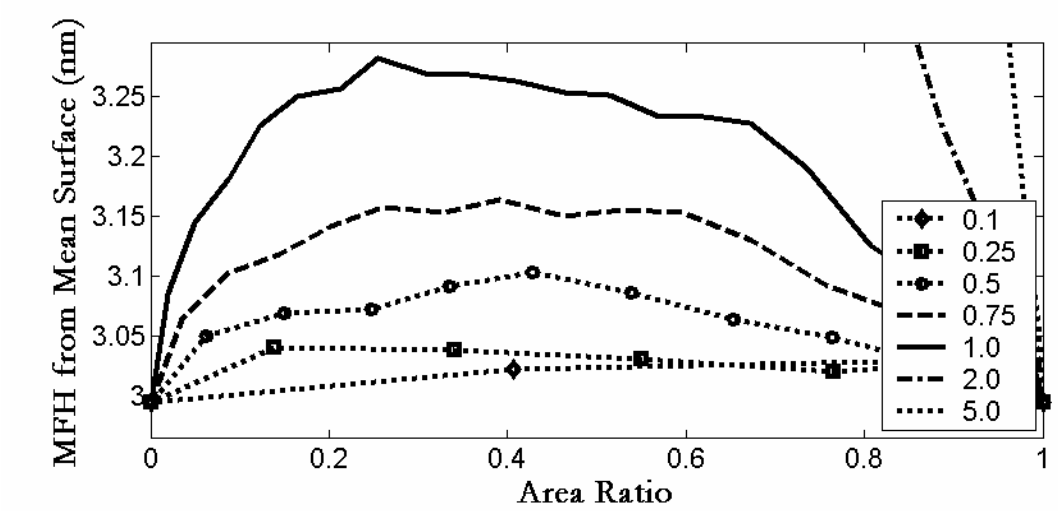

Figure 7.4: Minimum mechanical spacing of the slider measured from the mean surface of the patterned media without including the effect of intermolecular forces.

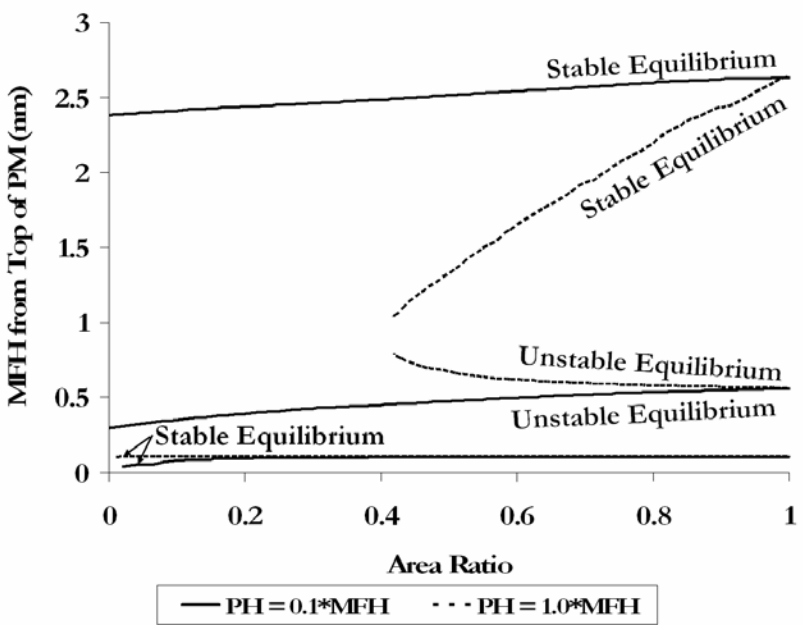

Figure 7.5: Minimum mechanical spacing of the slider measured from the top surface of the patterned media considering the effect of the intermolecular forces.

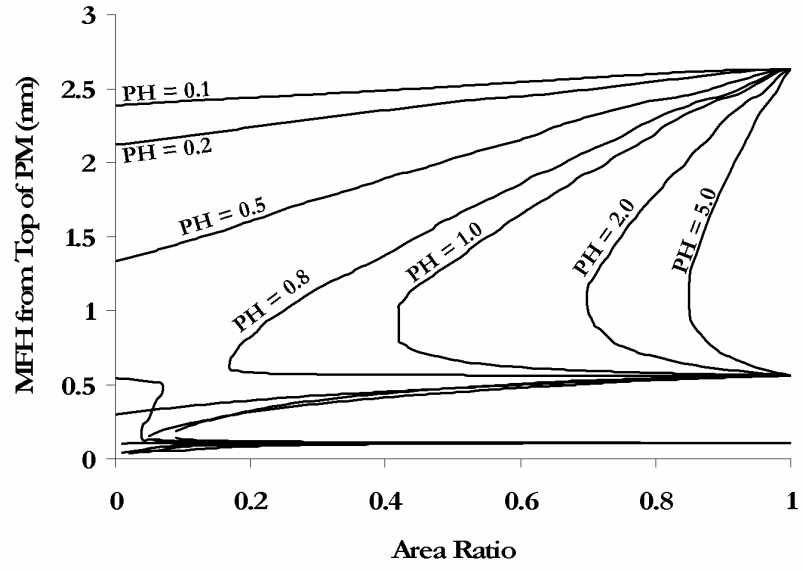

Figure 7.6: Minimum mechanical spacing of the slider measured from the top surface of the patterned media considering the effect of the intermolecular forces.

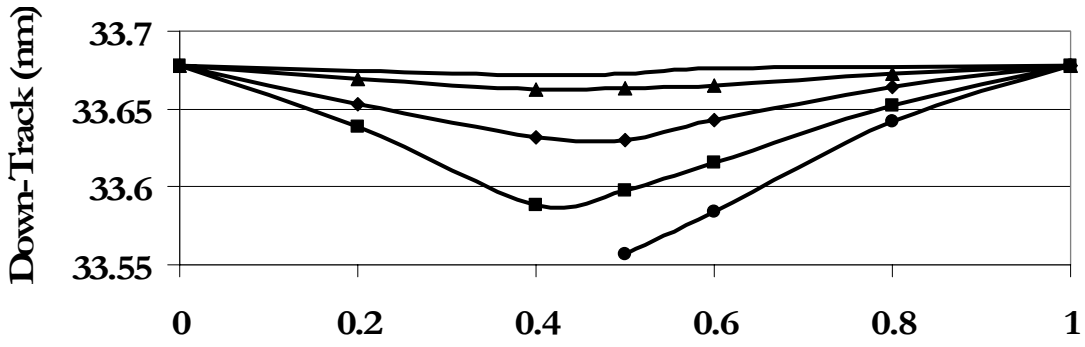
Down-Track (nm)
33.7
33.65
33.6
33.55
0
0.2
0.4
0.6
0.8
1

(a)

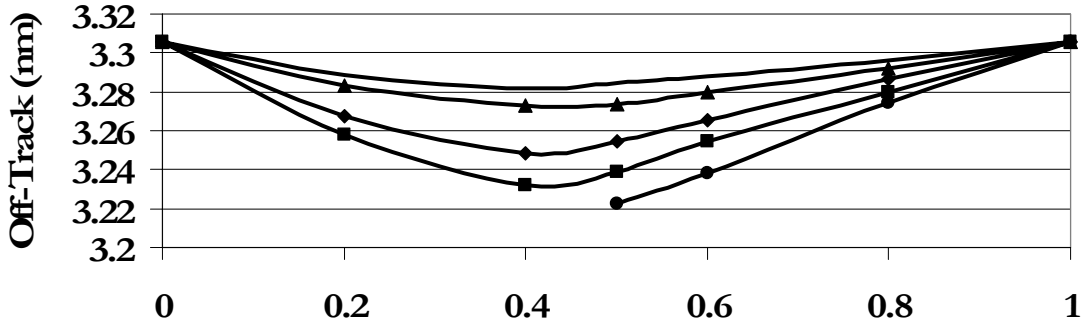
Off-Track (nm)
3.32
3.3
3.28
3.26
3.24
3.22
3.2
0
0.2
0.4
0.6
0.8
1

(b)

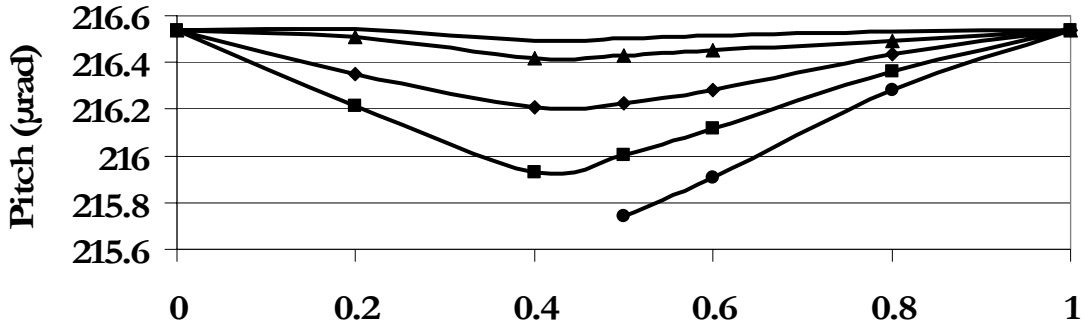
Pitch (μrad)
216.6
216.4
216.2
216
215.8
215.6
0
0.2
0.4
0.6
0.8
1

(c)

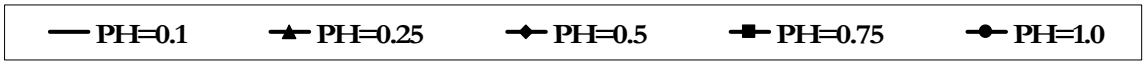
PH=0.1
PH=0.25
PH=0.5
PH=0.75
PH=1.0

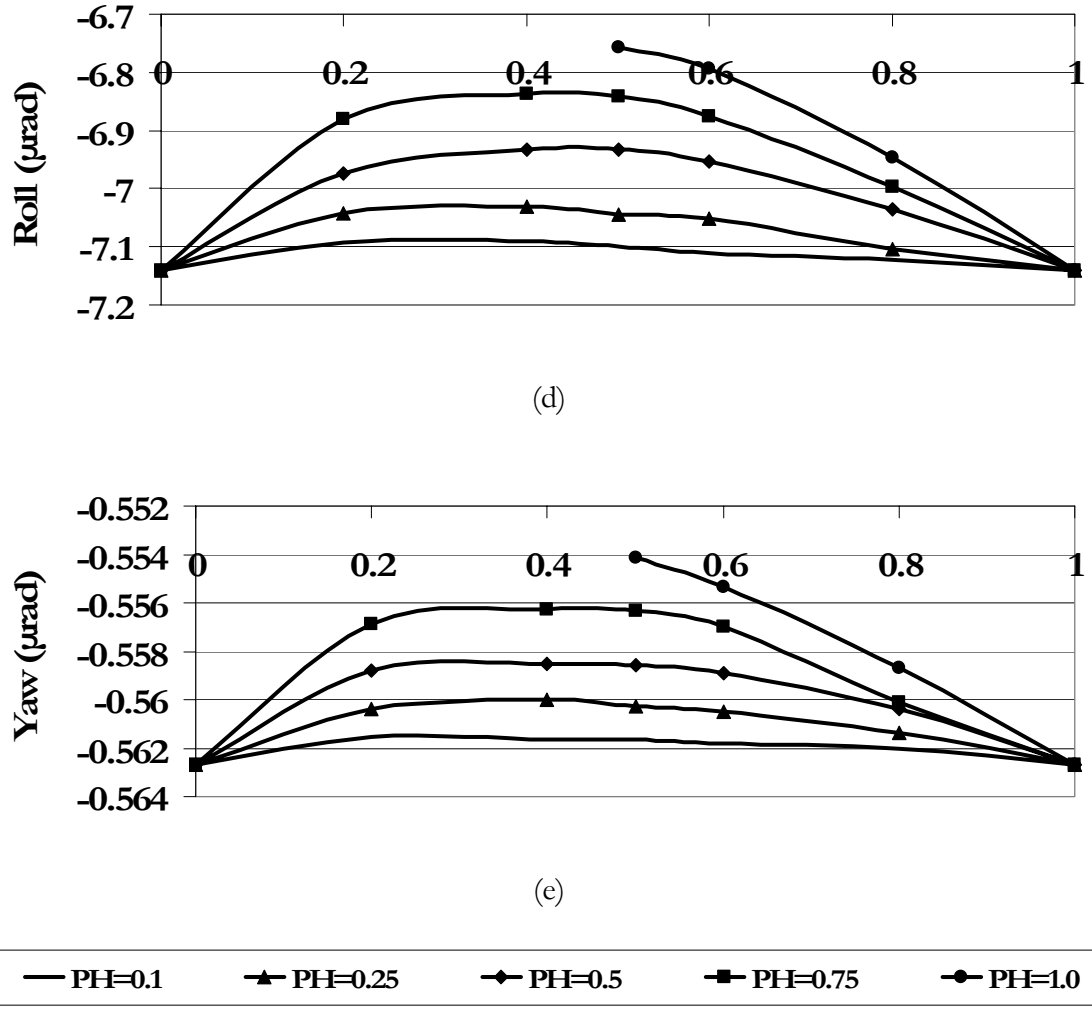

Figure 7.7: Slide's displacements in the (a) down-track, (b) off-track, (c) pitch, (d) roll, and (e) yaw direction as a function of area ratio for several values of the pattern height

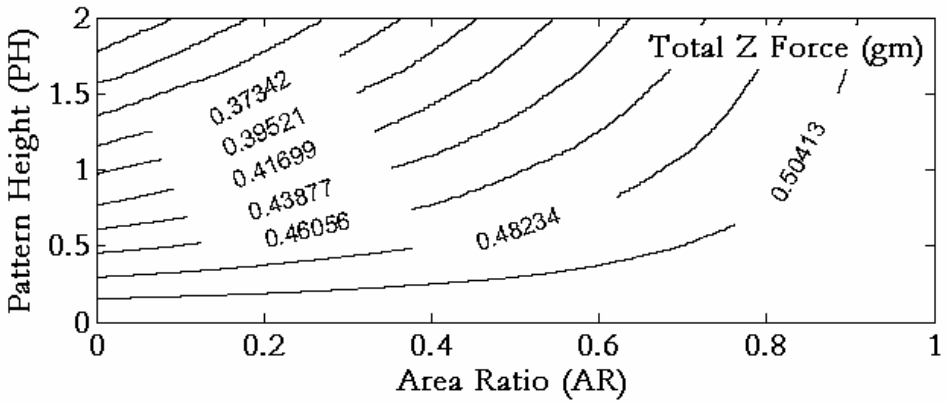

Figure 7.8: Total Z force as a function of the area ratio and the pattern height.

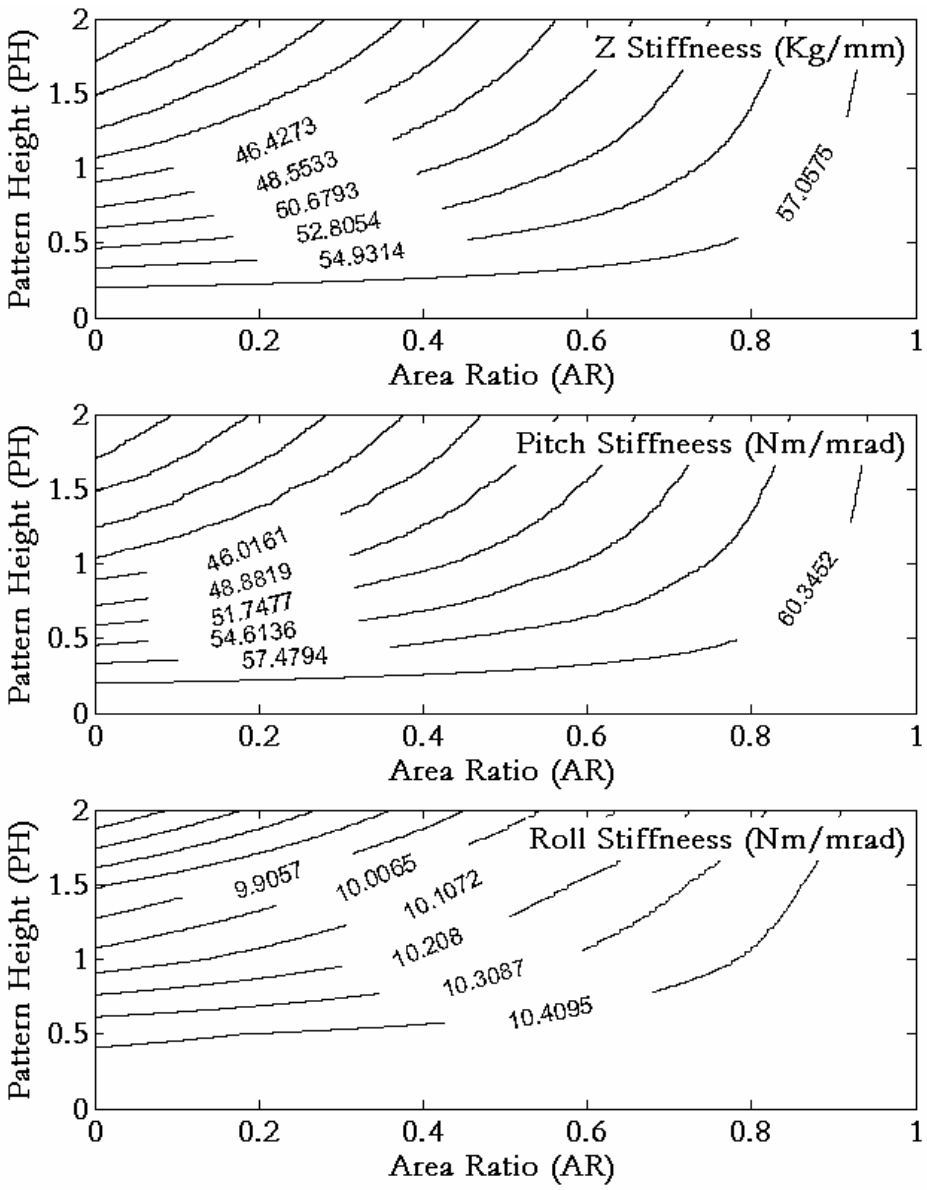

Figure 7.9: Z, pitch and roll stiffness as a function of the area ratio and the pattern height.

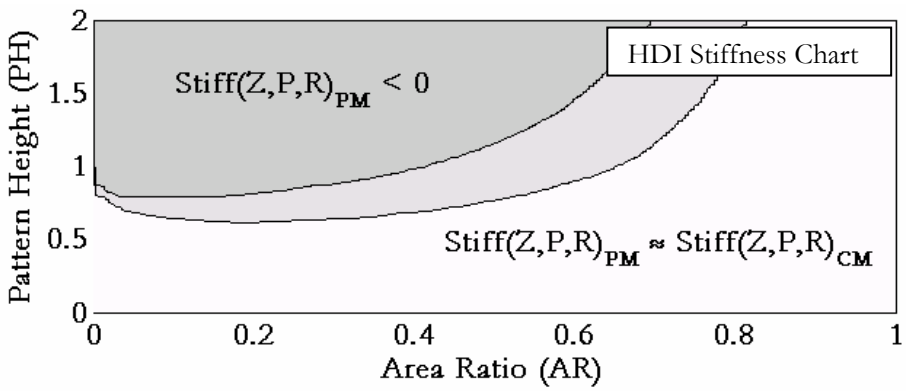

Figure 7.10: The HDI stiffness chart

CHAPTER 8

SUMMARY AND CONCLUSIONS

The disk drive industry is continuously trying to achieve higher data storage densities, faster data transfer rates, and higher reliability at lower cost. With a new areal storage density goal of 3 Tbit/in^2, the demand for a higher areal recording density can only be achieved by increasing the number of bits per track and the number of tracks per inch. This in turn requires smaller track width and smaller magnetic spacing and a reduction in the slider vibrations. But as the magnetic spacing between the slider and the disk reduces to less than 10 nm, the slider and disk will be either in intermittent or continuous contact and additional forces like intermolecular, electrostatic, contact and friction force will also act on the slider increasing its vibrations. Similarly, the demand for higher data transfer rates requires faster disk rotation speeds. But faster disk rotation speeds results in greater flow velocities and higher levels of aerodynamic forcing of the slider. This results in further excitation of the structural modes of the HSA and the disks, increasing the slider vibrations.

With elevated excitation due to windage, shock, contact, friction, electrostatic and intermolecular forces and tighter limits for slider vibrations – smaller variations in slider positioning pose a potential threat of HDI failures. Thus the dynamics and the stability of the air bearing slider is investigated in this dissertation.

The research presented in this dissertation addresses three objectives. The first objective is to develop a HDD model which can reliably predict the dynamics of sub 5 nm flying sliders. The second objective is to study the effect of intermolecular, electrostatic, contact and

aerodynamic forces on slider dynamics and propose strategies not only for reducing the slider vibrations but also for enhancing the stability of the HDI. The third objective is to evaluate the sliders flying characteristics over patterned media and propose optimal patterned media topography for maximum HDI stability.

In order to predict the slider dynamics, researchers in the past have used a simple model consisting of a slider and an air bearing model, while completely ignoring the dynamics of the HSA and the disk. Slider in-plane vibration due to aerodynamic forcing of the HSA and the disk can be 10 nm or more, but such effects were not considered by the previous models. Thus the system dynamics predicted by previous models is significantly different from the actual system response (measured experimentally) during slider-disk contact/impact, aerodynamic forcing, shocks, track seek, load-unload etc.

Thus, a new simulation program was proposed in chapter 2 which attempt to reliably predict the system dynamics by including the HSA and the disk model for the first time. Model order reduction technique is used to include the HSA and the disk models. Several metrics are developed to measure the accuracy of the reduced model. The Iterative IRS comes out as the best technique to obtain reduced HSA and disk models with highly accurate dynamic characteristics for the first few modes. The increase in the computation cost is also negligible. At the end of the chapter 2, the application of the reduced HSA models, computed using the Iterative IRS technique, is illustrated for dynamic simulations in hard disk drives.

The model is then used to investigate the slider dynamics and stability due to intermolecular

and electrostatic forces acting on the slider and the aerodynamic forces acting on the HSA and the disk. The effect of intermolecular and electrostatic forces on the slider's 6 degrees of freedom (DOF) and the interaction of the length scale of the slider-disk topographies with the slider vibrations and stability is investigated for the first time in this dissertation.

The air bearing slider's dynamics and stability in the presence of intermolecular and electrostatic forces for perfectly smooth HDI are reported in chapter 3. These forces are attractive in nature and inversely proportional to the mechanical spacing between the slider and the disk. As a result the lower the mechanical spacing between the slider and the disk, the higher is the magnitude of these forces. The reduction in the spacing can be as high as 10% or more of the mechanical spacing between the slider and the disk for reasonable values of Hamaker constant (A) and potential difference (V). But the change in the other 5 degrees of freedom, i.e. the off-track and the on-track displacement and the pitch, roll and yaw angle is relatively small, assuming the reduced flying height does not lead to more slider disk contact.

At very low mechanical spacing, the magnitude of these forces is very large and the total stiffness between the slider and the disk becomes negative. At this point the air bearing is no longer able to support the slider and this result in slider-disk contact and consequent failure. A flying height diagram is used to analyze the stability of the HDI. It is observed that high flying sliders can withstand higher potential difference between the slider and the disk before the air bearing breaks down. High pitch sliders are also more stable in the presence of intermolecular and electrostatic forces. At the end of chapter 3 the simulation results are compared with previously published experiments giving strong validation of the HDD

model.

In chapter 4 the effect of the slider-disk surface topography is also considered. The small wavelength slider-disk surface features – with wavelength less than a few μm – significantly affect the magnitude of the intermolecular forces and the contact forces. On one hand the magnitude of the contact forces increases on very rough surfaces, and on the other hand the magnitude of intermolecular surface increases on very smooth surfaces. This indicates that for maximum HDI stability slider and disk surfaces should not be extremely smooth, but instead some amount of roughness is necessary.

Intermediate wavelength slider-disk surface features – with wavelength more than a few μm but less than a few mm – excite some HSA modes and thus result in an increase in the amplitude of the slider vibration along all 6 degrees of freedom. Thus the slider vibrations can be reduced by selectively burnishing the wavelengths that can excite the critical modes of the HSA. Further, the large wavelength disk features – with wavelength more than a few mm – does not significantly effect the slider vibrations as the slider can easily follow these features.

Next the effect of air flow on slider vibrations is investigated in chapter's 5 and 6. First ever numerical investigation of slider vibrations due to aerodynamic forcing of the HSA and the disk considering the effect of the HDI forces is presented in these chapters. Oftentimes, there is a need to quickly estimate the slider vibrations for a range of disk RPM and slider radial position, from a single set of slider vibrations data for a particular disk RPM and slider radial position. But in order to compute the flow-induced slider vibrations, aerodynamic

forces acting on the HSA are required. And the air flow calculations using CFD packages for all possible combinations of the disk RPM and the slider's radial position can be computationally very expensive. Thus an alternative strategy is suggested in chapter 5. Two scaling laws are derived to predict the amplitudes of the aerodynamic forces on the HSA and hence the resulting slider vibrations as a function of the disk RPM and the slider's radial position. These laws are validated using the numerical computations.

The aerodynamic forces excite structural model of the HSA and the disk inducing a significant amount of slider vibrations. Thus the effects of several flow mitigation devices, smaller suspensions and reverse spinning disks on flow-induced slider vibrations are investigated in chapter 6. The flow mitigation devices considered in this dissertation are blocking plate, upstream and downstream spoiler. The blocking plate reduces the drag force near the slider and the suspension and thus the in-plane slider vibrations by about 50%. The downstream spoiler significantly reduces the drag force on the e-block arm, but also slightly increases the drag force near the slider and the suspension. Thus there is no significant reduction in in-plane slider vibrations with a downstream spoiler. The upstream spoiler on the other hand increases the in-plane slider vibrations by about 75%.

It is observed that for reverse spinning disks the HSA is better aligned with the streamlines of the flow. This results in smaller drag forces on the HSA and hence smaller in-plane slider vibrations. The effect of the suspension length, disk RPM and slider's radial position is also investigated. A reduction in suspension length results in a smaller in-plane slider vibrations. Further, at lower disk RPM and for small form factor drives, the slider off-track vibrations decreases.

But even if all targets for reduced mechanical spacing and tighter limits on slider vibrations are met, it will be difficult to achieve the areal recording density goal of 3 Tbit/in^2 with the current technology. This is because of the rapid approach of the superparamagnetic limit in the disk drives. This limit is reached when the magnetic energy (K_uV_g) is less than 40-60 times the thermal energy (K_BT), where K_u, V_g, K_B and T are the magnetic anisotropy constant, grain volume, Boltzmann constant and temperature. Under this condition the thermal energy alone can change the magnetization direction of the grain and the magnetization in the grains become thermally unstable. This restricts the minimum size of the thermally stable grain and thus the maximum achievable recording density on the conventional media to about 0.5-1 Tbit/in^2.

Patterned media has been proposed as an alternative to overcome this limit on the recording density. By some estimates, patterned media has the potential of increasing the recording densities by two orders of magnitude – up to and beyond 50 Tbit/in^2. But one of the main obstacles to patterned media is achieving stable mechanical head-media spacing. The air bearing slider's flying characteristics will be quite different on a pattern media compared to a conventional media depending on the topography of the surface. And the total air bearing stiffness will be compromised as the pattern height increases and/or the percentage area of the total disk covered by the pattern structure decreases, resulting in head media impact and consequent failure.

Thus in the chapter 7 slider's flying characteristics over pattern media is analyzed. Both the averaged and homogenized Reynolds equations are used to model the relationship between

the mechanical spacing and the pressure at the HDI. Both the averaged and the homogenized Reynolds equations are good approximations of the flow, especially for small pattern heights. It is observed that the slider's vertical displacements change significantly over patterned media, but the changes in the other five degrees of freedom – down-track and off-track displacements and the pitch, roll and yaw angles – are small.

In order to comment on the stability of the HDI over patterned media total stiffness is calculated along all six degrees of freedom. The vertical, pitch and roll stiffnesses reduce when the slider is flying over a patterned media as compared to when it is flying over a conventional media. This reduces the stability of the HDI and may also result in HDI failure. The analysis indicates that if the HDI on a patterned media is planarized so it is topographically similar to the HDI on a conventional media then the stability of the HDI can be restored to the same level as that on a conventional media. This can be done by filling the grooves with bonded lubricant or DLC overcoat.

REFERENCES

[1] Wikipedia, Hard Disk, URL: http://en.wikipedia.org/wiki/Hard_disk, online accessed 10th April, 2007.

[2] IBM Website, IBM 350 disk storage unit, URL: From: http://www-03.ibm.com/ibm/history/exhibits/storage/storage_350.html, online accessed 10th April, 2007.

[3] Seagate Technologies Website, URL: http://www.seagate.com/www/en-us/about/branding/product_photos/enterprise/, online accessed 10th April, 2007.

[4] Hitachi GST Website, URL: http://www.hitachigst.com/hdd/hddpdf/tech/hdd_technology2003.pdf, online accessed 10th April, 2007.

[5] INSIC Website, URL: http://www.insic.org/ehdr.htm, online accessed 10th April, 2007.

[6] J.N. Israelachvili, Intermolecular and surface forces, San Diego: Academic Press, 1992.

[7] V. Ponnaganti, "Dynamics of Head-Disk Interaction in Magnetic Recording", Ph.D. Dissertation, Department of Applied Mechanics, Stanford University, 1986.

[8] S. Lu, "Numerical Simulation of Slider Air Bearing", Ph.D. Dissertation, Department of Mechanical Engineering, University of California – Berkeley, 1997.

[9] R.J. Guyan, "Reduction of Stiffness and Mass Matrices", American Institute of Aeronautics and Astronautics Journal, 1965, vol. 3(2), pg. 380.

[10] B. Irons, "Structural Eigenvalue Problems: Elimination of Unwanted Variables", American Institute of Aeronautics and Astronautics Journal, 1965, vol. 3(5), pg. 961-962.

[11] Z.Q. Qu, "Model Order Reduction Techniques: With Applications in Finite Element Analysis", Springer, 2004.

[12] R.D. Henshell and J.H. Ong, "Automatic Masters for Eigenvalue Economization", Earthquake Engineering and Structural Dynamics, 1975, vol. 3, pg. 375-383.

[13] J. O'Callahan, "A Procedure for an Improved Reduced System (IRS) Model", Proceedings of 7th International Modal Analysis Conference, 1989, pg. 17-21.

[14] J.H. Gordis, "An Analysis of Improved Reduced System (IRS) Model Reduction Procedure", Proceedings of 10th International Modal Analysis Conference, 1992, pg. 471-479.

[15] M.I. Friswell, S.D. Garvey and J.E.T. Penny, "Model Reduction Using Dynamic and Iterated IRS Techniques", Journal of Sound and Vibration, 1995, vol. 186(2), pg. 311-323.

[16] M.I. Friswell, S.D. Garvey and J.E.T. Penny, "The Convergence of the Iterated IRS Method", Journal of Sound and Vibration, 1998, vol. 211(1), pg. 123-132.

[17] J. O'Callahan, P. Avitabile and R. Riemer, "System Equivalent Reduction Expansion Process (SEREP)", Proceedings of 7th International Modal Analysis Conference, 1989, pg. 29-37.

[18] M.I. Friswell, J.E.T. Penny, and S.D. Garvey, "Using Linear Model Reduction to Investigate the Dynamics of Structures with Local Non-Linearities", Mechanical Systems and Signal Processing, 1995, vol. 9(3), pg. 317-328.

[19] M.I. Friswell, J.E.T. Penny, and S.D. Garvey, "The Application of IRS and Balanced Relization Methods to Obtain educed Models of Structures with Local Non-Linearities", Journal of Sound and Vibration, 1996, vol. 196(4), pg. 453-468.

[20] R.L. Kidder, "Reduction of Structural Frequency Equations", American Institute

of Aeronautics and Astronautics Journal, 1973, vol. 11(6), pg. 892.

[21] C.A. Miller, "Dynamic Reduction of Structural Models", ASCE Journal of the Structural Division, 1980, vol. 106(10), pg. 2097-2108.

[22] O. Reynolds, "On Certain Dimensional Properties of the Matter in the Gaseous State", Philosophical Transactions of the Royal Society of London, 1879, vol. 170, pg. 727-845.

[23] G.E. Karniadakis and A. Beskok, Micro Flows – Fundamental and Simulation, Springer-Verlag, 2002.

[24] A. Burgdorfer, "The Influence of the Molecular Mean Free Path on the Performance of Hydrodynamic Gas Lubricated Bearings", ASME Journal of Basic Engineering, 1959, vol. 81, pg. 94-100.

[25] Y.T. Hsia and G.A. Domoto, "An Experimental Investigation of Molecular Rarefaction Effects in Gas Lubricated Bearings in Ultra-Low Clearances", Journal of Lubrication Technology – Transactions of ASME, 1983, vol. 105(1), pg. 120-130.

[26] Y. Mitsuya, "Modifed Reynolds Equation for Ultra-Thin Film Gas Lubrication Using 1.5-Order Slip Flow Models and Considering Surface Accommodation Coefficients", Journal of Tribology – Transactions of ASME, 1993, vol. 115(2), pg. 289-294.

[27] L. Wu and D.B. Bogy, "New First and Second Order Slip Models for Compressible Reynolds Equation", Journal of Tribology – Transactions of ASME, 2003, vol. 125(3), pg. 558-561.

[28] S. Fukui and R. Kaneko, "Analysis of Ultra-Thin Gas Film Lubrication Based on Linearized Boltzmann-Equation .1. Derivation of a Generalized Lubrication

Equation Including Thermal Creep Flow", Journal of Tribology-Transactions of the ASME, 1988, vol 110(2), pg. 253-262.

[29] S. Fukui and R. Kaneko, "A Database for Interpolation of Poiseuille Flow-Rates for High Knudsen Number Lubrication Problems", Journal of Tribology-Transactions of the ASME, 1990, vol 112(1), pg. 78-83.

[30] S.V. Patankar, "Numerical Heat Transfer and Fluid Flow", Taylor & Francis, Springer, 1980.

[31] S. Kirpekar, and D.B. Bogy, "Computation of Turbulence Induced vibrations in Hard Disk Drives", CML Technical Report.

[32] S. Kirpekar, and D.B. Bogy, "A Comparison of Large Eddy Simulation Models for Numerical Simulation of Air Flow in Hard Disk Drives", CML Technical Report.

[33] S. Kirpekar, "Computing Turbulence Induced Vibrations in Hard Disk Drives", PhD Thesis, Department of Mechanical Engineering, University of California at Berkeley, Spring 2006.

[34] Lin Wu, D.B. Bogy, "Effect of the Intermolecular Forces on the Flying Attitude of Sub-5 nm Flying Height Air Bearing Sliders in Hard Disk Drives", Journal of Tribology-Transactions of the ASME, 2002, vol 124(3), pg. 562-567.

[35] B.H. Thornton, D.B. Bogy, "Head-Disk Interface Dynamic Instability due to Intermolecular Forces", IEEE Transactions on Magnetics, 2003, vol 39(5), pg. 2420-2422.

[36] B. H. Thornton, and D. B. Bogy, "Non-Linear Aspects of Air Bearing Modeling and Dynamic Spacing Modulation in Sub 5 nm Air Bearings for Hard Disk Drives", IEEE Transaction on Magnetics, 2003, vol 39, pg. 722-728.

[37] J.D. Kiely and Y.T. Hsia, "Tribocharging of the Magnetic Hard Disk Drive Head-

Disk Interface", Journal of Applied Physics, 2002, vol 91(7), pg. 4631-4636.

[38] Z. Feng, C. Shih, V. Gubbi and F. Poon, "A Study of Tribo-Charge/Emission at the Head-Disk Interface," Journal of Applied Physics, 1999, vol 85(8), pg. 5615-5617.

[39] R.J.A. van den Oetelaar, L. Xu, D.F. Ogletree, M. Salmeron, H. Tang and J. Gui, "Tribocharging Phenomena In Hard Disk Amorphous Carbon Coating With And Without Perfluoropolyether Lubricants", Journal of Applied Physics, vol 89(7), pg. 3993-3998.

[40] D. Song, D. Schnur and Z. Boutaghou, "Mechanism of Discharge at the Head Disk Interface", no CC-07, 9th InterMAG conference, 2004.

[41] W.R. Chang, I. Etsion and D.B. Bogy, "An Elastic-Plastic Model for the Contact of Rough Surfaces", Journal of Tribology-Transactions of the ASME, 1987, vol 109, pg. 257-263.

[42] L. Kogut and I. Etsion, "Adhesion in Elastic-Plastic Spherical Microcontacts", Journal of Colloid and Interface Science, 2003, vol 261, pg. 372-378.

[43] H.M. Stanley, I. Etsion and D.B. Bogy, "Adhesion of Contacting Rough Surfaces in the Presence of Sub-Boundary Lubrication", Journal of Tribology-Transactions of the ASME, 1990, vol 112, pg. 98-104.

[44] J.A. Greenwood and J.B.P. Williamson, "Contact of Nominally Flat Surfaces", Proceedings of the Royal Society of London Series A – Mathematical and Physical Sciences, 1966, vol 295(1442), pg. 300-319.

[45] M. Germano, U. Piomelli, P. Moin, and W. H. Cabot, "A Dynamic Sub-Grid Scale Eddy Viscosity Model", Physics of Fluids A – Fluid Dynamics, 1991, vol 3(7), pg. 1760-1765.

[46] J. P. Vandoormaal and G. D. Raithby, "Enhancements of the Simple Method Incompressible Fluid Flows", Numerical Heat Transfer, 1984, vol 7(2), pg. 147-163.

[47] S. Tadepalli and P. Anandan, "Flow Induced Vibrations of Head Suspension Assemblies in Hard Drives", Asia Pacific Magnetic Recording Conference, Singapore, 2002, pg. AP3-01 - AP3-02.

[48] S. Kirpekar and D.B. Bogy, "A Study on the Efficacy of Flow Mitigation Devices in Hard Disk Drives", IEEE Transactions On Magnetics, 2006, vol 42(6), pg. 1716-1729.

[49] Q. Zeng and T. Hirano, "Some Experimental Observations of Disk Drives with Reverse Spinning Disks", ASME Information Storage and Processing Systems Conference, 2005, Santa Clara, CA, June 28-29.

[50] R.L. White, R.M.H. New and R.F.W. Pease, "Patterned Media: A Viable Route to 50 Gbit/in(2) and up for Magnetic Recording?", IEEE Transactions on Magnetics, 1997, vol 33(1), pg. 950-995.

[51] Z.Z. Brandic, E.A. Dobisz, T.W. Wu and T.R. Albrecht, "Patterned Magnetic Media: Impact of Nanoscale - Patterning on Hard Disk Drives", Solid State Technology, 2006, S7 Suppl. S.

[52] C. Ross, "Patterned Magnetic Recording Media", Annual Review of Materials Research, 2001, vol 31, pg. 203-235.

[53] Y. Mitsuya, T. Ohkubo and H. Ota, "Averaged Reynolds-Equation Extended to Gas Lubrication Possessing Surface-Roughness in The Slip-Flow Regime - Approximate Method and Confirmation Experiments", Journal of Tribology - Transactions of the ASME, 1989, vol 111(3), pg. 495-503.

[54] Y. Mitsuya and T. Koumura, "Transient-Response Solution Applying ADI Scheme to Boltzmann Flow-Modified Reynolds-Equation Averaged with Respect to Surface-Roughness", Journal of Tribology - Transactions of the ASME, 1995, vol 117(3), pg. 430-436.

[55] M. Jai, "Homogenization and 2-Scale Convergence of the Compressible Reynolds Lubrication Equation Modeling the Flying Characteristics of a Rough Magnetic Head Over a Rough Rigid-Disk Surface", Mathematical Modeling and Numerical Analysis, 1995, vol 29 (2), pg. 199-233.

[56] G.C. Buscaglia and M. Jai, "New Numerical Scheme for Non Uniform Homogenized Problems: Application to the Non Linear Reynolds Compressible Equation", Mathematical Problems in Engineering, 2001, vol 7(4), pg. 355-378.

[57] G. Buscaglia and M. Jai, "Sensitivity Analysis and Taylor Expansions in Numerical Homogenization Problems", Numerische Mathematik, 2000, vol 85(1), pg. 49-75.

[58] M. Duwensee and F.E. Talke, INSIC EHDR Tribology meeting, Colorado State University, Nov 2006.

[59] G.C. Buscaglia and M. Jai, "Homogenization of the Generalized Reynolds Equation for Ultra-Thin Gas Films and its Resolution by FEM", Journal of Tribology - Transactions of the ASME, 2004, vol 126(3), pg. 547-552.

[60] A. Almqvist and J. Dasht, "The Homogenization Process of the Reynolds Equation Describing Compressible Liquid Flow", Tribology International, 2006, vol 39(9), pg. 994-1002.

[61] G. Buscaglia, I. Ciuperca and M. Jai, "Homogenization of the Transient Reynolds Equation", Asymptotic Analysis, 2002, vol 32(2), pg. 131-152.

[62] M. Jai and B. Bou-Said, "A Comparison of Homogenization and Averaging

Techniques for the Treatment of Roughness in Slip-Flow-Modified Reynolds Equation", Journal of Tribology - Transactions of the ASME, 2002, vol 124(2), pg. 327-335.

[63] M. Kane and B. Bou-Said, "Comparison of Homogenization and Direct Techniques for the Treatment of Roughness in Incompressible Lubrication", Journal of Tribology - Transactions of the ASME, 2004, vol 126(4), pg. 733-737.